

การจำลอง และวิเคราะห์ของความดันลวดในระบบตัวกรองเซรามิกแบบแบ่งคู่ที่อุณหภูมิสูง



นาย วิศรุต จินตวร

สถาบันวิทยบริการ

จุฬาลงกรณ์มหาวิทยาลัย

วิทยานิพนธ์นี้เป็นส่วนหนึ่งของการศึกษาตามหลักสูตรปริญญาวิศวกรรมศาสตรมหาบัณฑิต

สาขาวิชาวิศวกรรมเคมี ภาควิชาวิศวกรรมเคมี

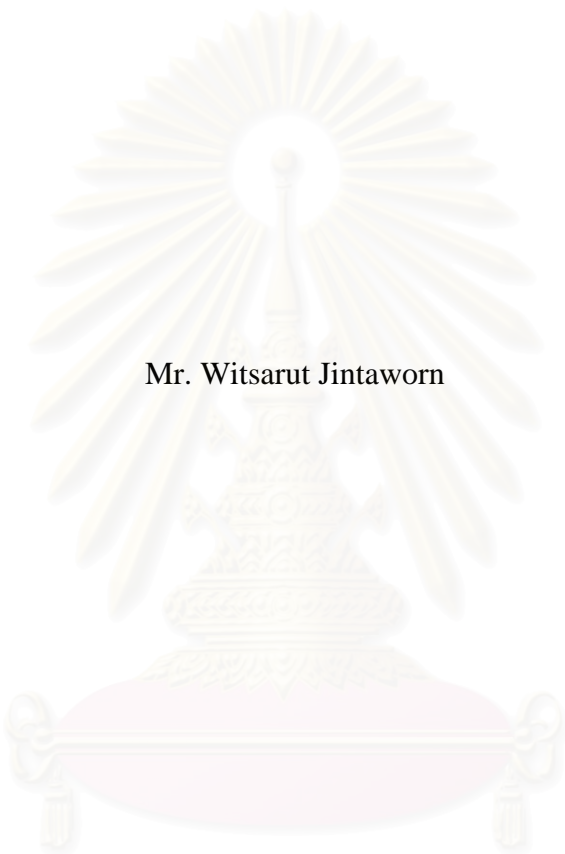
คณะวิศวกรรมศาสตร์ จุฬาลงกรณ์มหาวิทยาลัย

ปีการศึกษา 2548

ISBN 974-53-2829-4

ลิขสิทธิ์ของจุฬาลงกรณ์มหาวิทยาลัย

SIMULATION AND ANALYSIS OF PRESSURE DROP IN HIGH TEMPERATURE
TWIN-CANDLE CERAMIC FILTER SYSTEM



Mr. Witsarut Jintaworn

สถาบันวิทยบริการ
จุฬาลงกรณ์มหาวิทยาลัย

A Thesis Submitted in Partial Fulfillment of the Requirements
for the Degree of Master of Engineering in Chemical Engineering

Department of Chemical Engineering

Faculty of Engineering

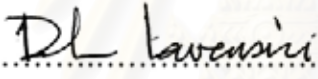
Chulalongkorn University

Academic Year 2005


ISBN 974-53-2829-4


Thesis Title SIMULATION AND ANALYSIS OF PRESSURE DROP IN
 HIGH TEMPERATURE TWIN-CANDLE CERAMIC
 FILTER SYSTEM
By Mr. Witsarut Jintaworn
Field of study Chemical Engineering
Thesis Advisor Associate Professor Tawatchai Charinpanitkul, D.Eng.
Thesis Co-advisor Professor Wiwut Tanthapanichakoon, Ph.D.

Accepted by the Faculty of Engineering, Chulalongkorn University in
Partial Fulfillment of the Requirements for the Master's Degree


.....Dean of the Faculty of Engineering
(Professor Direk Lavansiri, Ph.D.)

THESIS COMMITTEE

.....Chairman
(Associate Professor Suttichai Assabumrungrat, Ph.D.)

.....Thesis Advisor
(Associate Professor Tawatchai Charinpanitkul, D.Eng.)

.....Thesis Co-advisor
(Professor Wiwut Tanthapanichakoon, Ph.D.)

.....Member
(Assistant Professor Mana Amornkitbamrung, D.Eng.)

วิศรุต จินตวร : การจำลอง และวิเคราะห์ของความดันลดในระบบตัวกรองเซรามิกแบบ
 แท่งคู่ที่อุณหภูมิสูง (SIMULATION AND ANALYSIS OF PRESSURE DROP IN HIGH
 TEMPERATURE TWIN-CANDLE CERAMIC FILTER SYSTEM) อ. ที่ปรึกษา : รศ.
 ดร. ธวัชชัย ขรินพานิชกุล, อ. ที่ปรึกษาร่วม : ศ. ดร. วิวัฒน์ ตันตะพานิชกุล 99 หน้า.
 ISBN 974-53-2829-4.

ตัวกรองเซรามิกเป็นทางเลือกที่น่าสนใจในการจับกับอนุภาคแขวนลอยที่มีขนาดเล็กกว่า 2.5 ไมครอน
 (PM2.5) เนื่องจากเป็นวัสดุที่สามารถทนต่ออุณหภูมิสูง, ความดันสูง, สารเคมี และการกัดกร่อนได้ ขณะที่ชั้นเค้ก
 ก่อตัวขึ้นที่บริเวณผิวด้านนอกของตัวกรองเซรามิก ความดันลดซึ่งเป็นหนึ่งในลักษณะสมบัติที่สำคัญของ
 กระบวนการกรองจะเพิ่มขึ้นอย่างรวดเร็ว ในขณะที่เดียวกันประสิทธิภาพในการจับกับอนุภาค และการสิ้นเปลือง
 พลังงานในการดำเนินการจะเพิ่มขึ้นตามกัน ดังนั้นพัลส์เจ็ทจะถูกฉีดเป็นช่วง ๆ เพื่อให้ฝุ่นที่สะสมอยู่หลุดออก
 โดยวิธีนี้จะส่งผลให้ความดันลดในระบบลดลง

เทคนิคหนึ่งที่ถูกนำมาใช้ในการทำนายอัตราการเกิดขึ้นเค้กทางอ้อม คือพลศาสตร์ของของไหลแบบ
 คำนวณทางคณิตศาสตร์ (CFD) เนื่องจากเทคนิคนี้มีข้อดีคือคือค่าใช้จ่าย ปลอดภัย และใช้งานได้สะดวก
 อย่างไรก็ตาม การศึกษาทาง CFD ที่ผ่านมามีแนวโน้มศึกษาตัวกรองแบบแท่งเดี่ยว ในงานวิจัยนี้
 อัตราการเกิดขึ้นเค้กบนตัวกรองเซรามิกแบบแท่งคู่ในระบบต้นแบบจะถูกจำลองขึ้น และยืนยันผลของความดัน
 ลดที่ได้กับผลการทดลองจาก Hosokawa Powder Technology Research Institute (HPTRI) แบบจำลอง
 CFD ที่เหมาะสมซึ่งถูกจัดเตรียมโดยโปรแกรมทางการค้าที่มีชื่อว่า FLUENT ได้ถูกเลือกเพื่อนำมาใช้ในการ
 จำลองการไหลแบบ 3 มิติ ภายในระบบตัวกรองแบบแท่งคู่ การไหลที่ถูกคำนวณออกมาจะถูกใช้ในการประเมิน
 ค่าความเร็วในการไหลผ่านส่วนต่าง ๆ ของแท่งกรอง จากข้อสมมติฐานที่สมเหตุสมผลว่าแท่งกรองมีประสิทธิภาพ
 ในการจับกับอนุภาค 100% และ อนุภาคมีขนาดเล็กกว่าระดับไมโครเมตร อนุภาคจะเคลื่อนที่ไปตามเส้นการ
 ไหลของอากาศโดยมีการกระจายตัวอย่างสม่ำเสมอในอากาศ ดังนั้นเราจึงสามารถทำนายความแตกต่างของ
 อัตราการเกิดขึ้นเค้กที่บริเวณส่วนต่าง ๆ กันของแท่งกรองจากความเร็วที่พื้นผิวของส่วนนั้น ๆ และสามารถ
 คำนวณสมบัติด้านความต้านทานของชั้นเค้กได้ นอกจากนี้เทคนิค CFD ยังถูกใช้ในการศึกษาผลของตัวแปร
 หลัก เช่น ความเร็วในการกรอง, อุณหภูมิ, ความเข้มข้นของฝุ่น และตำแหน่งในการป้อน ซึ่งจะถูกรับเปลี่ยนค่า
 พบว่าความเร็วในการกรองเป็นตัวแปรที่ส่งผลกระทบที่สุดต่อความดันลดของระบบ

ภาควิชา วิศวกรรมเคมี
 สาขาวิชา วิศวกรรมเคมี
 ปีการศึกษา 2548

ลายมือชื่อนิสิตร.....วิศรุต จินตวร.....
 ลายมือชื่ออาจารย์ที่ปรึกษา.....
 ลายมือชื่ออาจารย์ที่ปรึกษาร่วม.....

4670499721 MAJOR ENGINEERING

KEY WORD: CFD / CERAMIC FILTER / TWIN CANDLES / DUST COLLECTION / HIGH TEMPERATURE

WITSARUT JINTAWORN: THESIS TITLE. (SIMULATION AND ANALYSIS OF PRESSURE DROP IN HIGH TEMPERATURE TWIN-CANDLE CERAMIC FILTER SYSTEM) THESIS ADVISOR: ASSOC. PROF. TAWATCHAI CHARINPANITKUL, D.Eng., THESIS CO-ADVISOR: PROF. WIWUT TANTHAPANICHAKOON, Ph.D., 99 pp. ISBN 974-53-2829-4

The ceramic candle filter presents an interesting alternative to collect aerosol particles smaller than $2.5 \mu\text{m}$ (PM_{2.5}) because of its high resistance to high temperature, high pressure, chemicals and corrosion. As cake builds up on the outside surface of the ceramic candle filter, pressure drop, one of the important characteristics of filtration, would be increased rapidly. Meanwhile, the collection efficiency and energy consumption also increased in tandem. So, a pulse jet is injected periodically to shake down the accumulated dust cake, thereby reducing the pressure drop in the system.

One technique frequently used to indirectly predict cake formation rate applies computational fluid dynamics (CFD) since it offers low cost, low risk and ease of use. However, nearly all previous CFD investigations focused on single filters. In this research, the cake formation rate on twin ceramic candle filters in a prototype system was modeled and its pressure drops validated with experimental data obtained by Hosokawa Powder Technology Research Institute (HPTRI). A suitable CFD model provided by commercial software code FLUENT was selected and employed to simulate the 3D fluid flow inside the twin-candle unit. The calculated flow field was used to estimate the local flow velocities. Due to the reasonable assumption of 100% collection efficiency and submicrometer aerosol size, the particles would move along the gas streamline with uniform distribution. Thus we could predict the differences in cake formation rate on each part or element of the candle filter from the local face velocity and calculate the cake resistance properties. In addition, the CFD technique was used to investigate the effects of such major parameters as filtration velocity, temperature, dust concentration and inlet feed location, to be varied. It was found that the filtration velocity was the most important parameter affecting the pressure drop of the system.

Department Chemical Engineering

Field of study Chemical Engineering

Academic year 2005

Student's signature... W. Jintaworn

Advisor's signature... T. Charinpanitkul

Co-advisor's signature... W. Tanthapanichakoon

ACKNOWLEDGMENTS

The author sincerely wishes to thank Prof. Wiwut Tanthapanichakoon and Assoc. Prof. Tawatchai Charinpanitkul, thesis advisors, for their invaluable advice, and constant encouragement throughout this project.

The author would like to thank New Energy Development Organization (NEDO) for their financial supporting to this research.

The author would like to express a special thank to Assoc. Prof. Suttichai Assabumrungrat and Asst. Prof. Mana Amornkitbamrung for their useful comments and participation as the thesis committee.

Furthermore, the author is also grateful to the Prof. Takehisa Fukui and Mr. Masahiro Yoshikawa, Hosokawa Powder Technology Research Institute, Osaka, Japan, for their kindness and valuable data. The author is indeed grateful to Prof. Makio Naito, Joining and Welding Research Institute, Osaka University, Osaka, Japan.

Moreover, the author would like to thank Ms. Jerapan Laksameearunotai, Mr. Dumrongsak Leochaiporn, Mr. Kompanart Kaewplang, Mr. Sira Srinives and the entire member of Particle technology and Material Processing Laboratory.

In addition, the author would like to acknowledge the Assoc. Prof. Anchaleeporn Waritswat Lothongkum, Dr. Surat Areerat and Mr. Pisan Polpoh, Department of Chemical Engineering, King Mongkut's Institute of Technology Ladkrabang (KMITL) for their kindly collaboration.

Eventually, the author would like to express deep thank to his parents for their love, support and encouragement throughout the course of his life.

จุฬาลงกรณ์มหาวิทยาลัย

CONTENTS

	Page
ABSTRACT IN THAI	iv
ABSTRACT IN ENGLISH	v
ACKNOWLEDGEMENTS	vi
CONTENTS	vii
LIST OF TABLES	xi
LIST OF FIGURES	xii
NOMENCLATURE	xvi
CHAPTER	
I INTRODUCTION	
1.1 Introduction	1
1.2 Objectives	2
1.3 Scopes of research	3
1.4 Procedure of research	3
II LITERATURE REVIEW	
2.1 Experiment	4
2.2 Simulation	6
III THEORY	
3.1 Pressure drop of ceramic filter	10
3.2 Efficiency of dust collection to pressure drop	11
3.3 Computational Fluid Dynamics (CFD)	11
3.4 Commercial software used for CFD	
3.4.1 Pre-processing program	12
3.4.2 Processing program	13
3.4.3 Post-processing program	15
3.5 Modeling turbulence	
3.5.1 RNG k- ϵ model	16
3.5.2 Governing equations	17

CHAPTER	Page
3.5.2.1 Continuity Equation	18
3.5.2.2 Momentum Equation	19
3.5.2.3 Energy Equation	20
3.5.2.4 Equation for turbulent kinetic energy (k)	20
3.5.2.5 Equation for dissipation rate of turbulent kinetic energy (ϵ)	20
3.5.3 Porous media model for ceramic candle filter	20
3.5.3.1 Continuity equation for flow through the porous medium	21
3.5.3.2 Momentum equation for flow through the porous medium ...	21
3.5.3.3 Energy equation for flow through the porous medium	21
3.6 Discretization method	22
3.7 Under-relaxation factor	23
IV MODELING AND SIMULATION	
4.1 Description of experimental set-up	
4.1.1 Filtration rig	26
4.1.2 Measurement of average pressure difference	29
4.2 Meshing	
4.2.1 The need for mesh	32
4.2.2 Building meshes	34
4.2.3 Modifying meshes for better solution	37
4.3 Defining model parameters	
4.3.1 Fluid properties	38
4.3.2 Ceramic candle filter properties	39
4.3.3 Boundary conditions	40
4.4 Model assumptions	
4.4.1 Assumptions for ceramic candle filter	41
4.4.2 Assumptions for fluid flow behavior	41

CHAPTER	Page
4.5 Procedure of simulation	
4.5.1 Virgin filter with clean air	43
4.5.2 Loaded filter (cyclic operation)	43
V RESULTS AND DISCUSSION	
5.1 Validation of virgin filter with clean air	
5.1.1 Viscous resistance of candle filter	49
5.1.1.1 Effect of influent gas flow rate	49
5.1.1.2 Effect of elevated gas temperature	50
5.1.2 Spatial distribution of local face velocity	51
5.2 Validation of model for cyclic operation (dust-laden air, pulsed cleaning)	
5.2.1 Viscous resistance and cake thickness formed	
uniformly on the surface of each candle filter	54
5.2.1.1 Face velocity distribution	56
5.2.1.2 Relative change in cake thickness	56
5.2.2 Non-uniform cake formation on each candle filter	
5.2.2.1 Face velocity distribution	60
5.2.2.2 Specific cake resistance	67
5.2.2.3 Relative change in cake thickness	68
5.3 Effect of elevated gas temperature	71
5.4 Effect of influent gas flow rate at high temperature	72
5.5 Effect of dust concentration at high temperature	73
5.6 Effect of gas inlet location at high temperature	74
VI CONCLUSIONS AND RECOMMENDATIONS	
6.1 Conclusions	
6.1.1 Virgin filter with clean air	76
6.1.2 Cyclic operation (dust-laden air, pulsed cleaning)	76
6.2 Recommendation for future work	77

CHAPTER	Page
REFERENCES	78
APPENDICES	
APPENDIX A Dimensions of the dust removal system	82
APPENDIX B Velocity vector profile	86
APPENDIX C Pressure drop from simulation	93
APPENDIX D Calculation example	96
VITA	99



สถาบันวิทยบริการ
จุฬาลงกรณ์มหาวิทยาลัย

LIST OF TABLES

	Page
Table 4.1	Specifications of the ceramic candle filter.....27
Table 4.2	Surface area of each element45
Table 5.1	Zones of normal face velocity distribution along z-position of the candle..... 53



สถาบันวิทยบริการ
จุฬาลงกรณ์มหาวิทยาลัย

LIST OF FIGURES

	Page
Figure 3.1	Trend of the pressure drop in the single-candle system..... 11
Figure 3.2	Basic Program Structure of FLUENT..... 14
Figure 3.3	The mass flux in and out of the fixed volume element through which a fluid is flowing ($u=v_x$, $v=v_y$, $w=v_z$) 18
Figure 3.4	The momentum flux in and out of the fixed volume element through which a fluid is flowing 19
Figure 3.5	Control Volume Used to Illustrate Discretization of a Scalar transport Equation 23
Figure 3.6	Overview of the segregated solution method..... 24
Figure 4.1	Schematic diagram of the experimental setup by HPTRI..... 27
Figure 4.2	Photo of ceramic candle filter using in experimental set-up..... 27
Figure 4.3	SEM image of testing dust (Fly ash JIS10) 28
Figure 4.4	SEM image of testing dust (Carbon black JIS12)..... 29
Figure 4.5	Example of experimental ΔP across filter candle A (Fly ash JIS No.10, average air temperature 543 K, air flow volume $0.38 \text{ m}^3/\text{min}$, feed dust concentration $5 \text{ kg}/\text{m}^3$, pulse interval 120 seconds)..... 30
Figure 4.6	Measured values of ΔP_A , estimated values of ΔP_B and overall ΔP_{av} ... 30
Figure 4.7	Cross section of filtration unit and positions of pressure drop measurements..... 31
Figure 4.8	Effect of mesh density 33
Figure 4.9	The tetrahedron shape of mesh structure 34
Figure 4.10	Illustration of the employed computational grid in the twin-candle system feeding from the bottom position..... 35
Figure 4.11	Illustration of the employed computational grid in the twin-candle system feeding from the top position..... 36
Figure 4.12	Illustration of the employed computational grid in the twin-candle system feeding from the tangential position 36

	Page
Figure 4.13	Illustration of the employed computational grid in the single-candle system feeding from the bottom position37
Figure 4.14	Modifying mesh using for calculation38
Figure 4.15	The parameters required for fluid specification.....38
Figure 4.16	The properties of ceramic candle filter39
Figure 4.17	The characteristic of ceramic candle filter.....40
Figure 4.18	The velocity inlet boundary condition41
Figure 4.19	The procedure of calculation of the flow resistance of the virgin ceramic candle filter.....43
Figure 4.20	The filter sub-divided into 4 quadrants for each of the 8 layers44
Figure 4.21	The 8 layers of the candle filter used in calculation45
Figure 4.22	The shape of each element used for the calculation46
Figure 4.23a	Estimate property (flow resistance) of candle wall of virgin filter....47
Figure 4.23b	Estimate property (flow resistance) of candle wall of used filter under cyclic operation, including permanent flow resistance due to embedded particles.....47
Figure 4.23c	Estimate changes in flow resistance, gas through-flow, cake thickness, etc. of each candle wall element during cyclic operation ..48
Figure 5.1	The effect of the flow rate on the relation between the viscous resistance of the candle wall and the pressure drop.....50
Figure 5.2	The effect of the temperature on the relation between the viscous resistance of the candle wall and the pressure drop.....51
Figure 5.3	Calculated deviations of local normal face velocity at each height and each quadrant of the twin virgin candles.....52
Figure 5.4	Calculated deviations of local normal face velocity at each height and each quadrant of the single and twin virgin candles54
Figure 5.5	Comparison of the calculated and experimental pressure drops.....55
Figure 5.6	The estimated viscous resistances of individual candle filters and the combined total at each cyclic time step.....55
Figure 5.7	The calculated normal face velocity at each cyclic time56
Figure 5.8	Relative change in cake thickness occurring at each cyclic time57

	Page
Figure 5.9	The calculated pressure drop compared with the experimental value at each cyclic time58
Figure 5.10	The local viscous resistance of the candle filter A at each height as a function of cyclic time59
Figure 5.11	The local viscous resistance of the candle filter B at each height as a function of cyclic time59
Figure 5.12	The experimental pressure drop compared with the simulation results60
Figure 5.13	Distribution of local fluid velocity normal to the candle's surface at the top end position as a function of cyclic time61
Figure 5.14	Distribution of local fluid velocity normal to the candle's surface at $z=-930\text{mm}$ as a function of cyclic time.....62
Figure 5.15	Distribution of local fluid velocity normal to the candle's surface at $z = -950\text{mm}$ as a function of cyclic time.....62
Figure 5.16	Distribution of local fluid velocity normal to the candle's surface at $z=-970\text{ mm}$ as a function of cyclic time.....63
Figure 5.17	Local fluid velocity through the first quadrant of the left candle at various heights (z) as a function of cyclic time64
Figure 5.18	Local fluid velocity through the first quadrant of the right candle at various heights (z) as a function of cyclic time64
Figure 5.19	Schematic of the local face velocity distribution along z -position at time = 065
Figure 5.20	Relative change in the velocity of the right candle before and after the right candle filter is pulsed as a function of height.....66
Figure 5.21	Relative change in the velocity of the left candle before and after the right candle filter is pulsed as a function of height67
Figure 5.22	The specific resistance of the left candle as the function of time68
Figure 5.23	The specific resistance of the right candle as the function of time68
Figure 5.24	Relative change in accumulated cake thickness on quadrant 2 of the left candle.....69

	Page
Figure 5.25	Relative change in accumulated cake thickness on quadrant 1 of the right candle.....70
Figure 5.26	Relative change in accumulated cake thickness at the top end of the candle filter.....71
Figure 5.27	The effect of temperature on pressure drop as a function of time72
Figure 5.28	The effect of flow rate on pressure drop at high temperature condition73
Figure 5.29	The effect of dust concentration on pressure drop at high temperature condition.....74
Figure 5.30	The effect of gas inlet location on pressure drop as a function of time75
Figure 5.31	Profile of velocity vector at inlet port as a function of x and y for case of the tangential feed port of the twin candle system.....75

NOMENCLATURES

A	Surface area [m^2]
\vec{A}_f	Area of face f [-]
C_{in}	Inlet gas concentration [mg/l]
C_{out}	Outlet gas concentration [mg/l]
d_p	Mean diameter of particles [m]
E_f	Total fluid energy [J]
E_s	Total solid phase energy [J]
k_{eff}	Effective thermal conductivity in the porous medium [W/m]
k_f	Fluid phase thermal conductivity [W/m]
k_s	Solid phase thermal conductivity [W/m]
L	Thickness of the medium [m]
L_1	The first quadrant of the left candle [-]
L_2	The second quadrant of the left candle [-]
L_3	The third quadrant of the left candle [-]
L_4	The fourth quadrant of the left candle [-]
R_1	The first quadrant of the right candle [-]
R_2	The second quadrant of the right candle [-]
R_3	The third quadrant of the right candle [-]
R_4	The fourth quadrant of the right candle [-]
m	Dust load per area [kg/m^2]
N_{faces}	Number of faces enclosing cell [-]
Q	Gas flow rate [m^3/s]
S_f^h	Fluid enthalpy source term [J]
S_i	Source term in the part of porous media [J]
S_ϕ	Source of ϕ per unit volume [J/m^3]
v	Gas velocity [m/s]
\vec{v}	Physical velocity through porous medium [m/s]
V_f	The velocity of the fluid [m/s]

η	Efficiency of particle collection [-]
π	Penetration [-]
γ	The porosity of the ceramic candle filter [-]
ε	Porosity of the medium [-]
ψ	The inertial resistance factor [-]
μ	Viscosity of air [Pa.s]
ρ	Density of gas [kg/m ³]
ξ	Specific resistance of ceramic candle filter [m ⁻¹]
α	Specific resistance of dust cake [m ⁻¹]
ΔP_{total}	Pressure drop of the filtration system [Pa]
ΔP_{filter}	Pressure drop due to ceramic candle filter [Pa]
$\Delta P_{\text{dust cake}}$	Pressure drop due to dust cake layer [Pa]



สถาบันวิทยบริการ
จุฬาลงกรณ์มหาวิทยาลัย

CHAPTER I

INTRODUCTION

1.1 Introduction

Recently air pollution has become a serious public health issue in Thailand. Particulate matter (PM) not only constitutes one of the primary air pollutants but also often contains toxic components hazardous to human health. PM is produced from various industrial processes such as thermal power plants, including those which use diesel oil as main fuel of diesel generators. Therefore it is imperative to remove the particulate matter before it is emitted to the atmosphere and threatens the health of power plant employees and residents in the surrounding communities. Fine particles with diameters smaller than 2.5 micrometers (PM_{2.5}) are known to have the highest impact on human health because they can penetrate deeply into the human respiratory system. Therefore it is indispensable to develop a high-temperature particulate matter (soot) collecting system with high collection efficiency.

Several high-temperature dust collection technologies have been proposed and investigated around the world. One of the most promising practical methods is the employment of ceramic candle filters. The inevitable changes in pressure loss and face velocity during cyclic operation of filtration and dedusting may significantly influence filter durability. The pulse-cleaning jet and its pressure in the filter cavity might not be distributed uniformly along the filter length. Both experimental results and numerical calculations were employed to investigate some characteristics of the pulse jet cleaning [1]. Computer simulation was used to investigate the influence of the filtration velocity and the maximum pressure drop. It was found that the residual pressure drop of the filter depended on the compressibility of the dust cake building up on the surface the filter medium with every new filtration cycle. The compressibility of the dust cake was defined by a relation between the cake compression pressure and tolerable stress [2]. Occasionally the ceramic filter tended to show patchy cleaning when the filter regeneration was incomplete. Achim Dittler et al. compared the regeneration behavior between modeling and experimental results

during the following filtration cycle. The observed fair agreement indicated that the model has good predictive capability for operational filter cleaning. Both filter conditioning and dust cake compression significantly influenced the operational performance of partially regenerated filter media [3]. The filtration and the reversed flow process at ambient conditions were investigated by T.G. Chuaha et al. using a cylindrical filter and tapered filter. They modeled the gas flow along the ceramic candle filter by assuming one-dimensional steady state flow. For the tapered filter, the model's prediction was shown to have good agreement with their experimental data [4]. Unless correctly designed, manufactured and operated, the high-temperature ceramic filtration process could become unstable. As one of the necessary conditions for stable operation, they identified the time-dependent relation between the pressure drop across the filter candles and the deposited dust load during each filtration cycle. In other words, determination of the process parameters involved in the prediction of the pressure drop as a function of the deposited soot mass is a necessary condition for successful long-term cyclic operation of filter loading (filtration) and regeneration (decaking). During the build-up of the dust cake, the pressure drop of the filtration system increased monotonically and the system was periodically regenerated by the application of air-pulse cleaning or some other effective decaking method.

A typical ceramic filtration unit consists of a multitude of filter candles. However, nearly all previous CFD investigations have focused on single filters. For the sake of simplicity, only a twin-candle filtration unit will be validated with experimental data obtained by Hosokawa Powder Technology Research Institute (HPTRI). We employ a CFD model provided by commercial software (FLUENT) to simulate the 3D fluid flow inside the ceramic twin-candle filter unit. The calculated flow field is used to estimate the local flow velocities. In addition, the CFD technique allows the major parameters to be varied and investigated efficiently.

1.2 Objectives

The objective of this research is to simulate and analyze the pressure drop across the twin-candle ceramic candle filter system by including the effect of filtration velocity, dust concentration, gas temperature and gas inlet location.

1.3 Scope of research work

The scope of this research is as follows:

1. Simulate the pressure drop of the virgin twin-candle ceramic filter system.
2. Investigate the effects of key parameters, such as filtration velocity, dust concentration, gas temperature and gas inlet location, on the pressure drop across the filter and then verify the simulation results by using experimental results.
3. Inlet gas temperature range: 15 - 600 °C.
4. Filtration velocity range: 1 – 5 cm/s.
5. Inlet dust concentration range: 5 - 50 g/m³.
6. Gas inlet location: three positions.

1.4 Procedure of the research

1. Review the related literature.
2. Consider suitable mathematical models which could represent the system.
3. Run simulation and validate the simulation results by comparison with experimental results as reported data.
4. Analyze and discuss effects of concerning variables on pressure drop.
5. Write the thesis.

CHAPTER II

LITERATURE REVIEW

This chapter will review representative reports on the removal of the particulate matter emitted using the ceramic candle filter. Both of the experiment and the simulation are observed. They are summarized as follows.

2.1 Experiment

A. Larbot et. al employed ceramic air filters (CAF) with different characteristics to investigate the influence of face velocity and CAF characteristics (porous volume, average pore diameter and thickness) on the values of aerosol penetration and pressure drop. The investigations were carried out by varying all the parameters influencing the filter performance. It was found that face velocity and CAF thickness had a strong influence on the collection efficiency. As expected, if the velocity increased or the thickness decreased, the filter efficiency decreased [1].

E. Schmidt investigated the compression of dust cakes deposited on filter media by considering the various factors such as particle size distribution, particle charge, adhesive and cohesive properties, and pressure drop across filter element. The filter flow resistance and pressure drop nonlinearly increased with filtration time. There were jumps in pressure drop at a higher cleaning frequency, which is disadvantageous for filtration performance. They predicted the deviation in the time-dependent pressure loss functions from the linear trend. Compression results of different filter cakes were verified by local cake structure analyses, thereby indicating inadequate cake stability [2].

C.R.N. Silva et. al studied the behavior of the filter during filtration at several superficial velocities with respect to the formation and removal of the deposited layer. The cake porosity decreased and the cake specific resistance increased with increase in the face velocity due to particle settling before reaching the filter. They suggested that the effect of porosity is greater than that of the average diameter of the particles. The estimated cake/fabric adhesion force was estimated as well as the effective

distance between the particle surfaces [3].

K. Smolders and J. Baeyens determined the baseline pressure drop and the effect of the cleaning cycles from the experimental results for various face velocities. The baseline pressure drop increased dramatically and the removal of dust cake was vital for a return to the virgin state. The jet-cleaning velocity was important. Too low velocities were insufficient to adequately clean the filter. In practice, the total pressure consists of the baseline pressure drop and the pressure drop of the dust layer which is directly affected by the dust load. The equation through porous media can be used to calculate the proportionality factor for predicting the time between two cleaning cycles [4].

C. Kanaoka and M. Amornkitbamrung captured dust by a ceramic filter using five elements made of different materials and structures. Injecting a high-pressure pulse clean air, the behavior of dust detachment was monitored by high speed video images. At the beginning, the pressure drop across the filter surface increased immediately because of the formation of a dense dust layer on the ceramic filter surface and was followed by a slowdown in the increase in rate due to the formation of a coarse layer. In the cleaning process, the pressure traces had different behaviors after the injection of cleaning air, depending on the filter permeability and the filter material [5].

D. Thomas et. al studied the increase of pressure drop and filter efficiency (characterized by HEPA filters) during the filter clogging that was linked to both penetration profile inside the filter bed and the deposited structure. Within the range of their study, no influence of either the face filtration velocity or the aerosol concentration on deposit structure was detected. They found that larger particles induced a smaller pressure drop, which is linked to the specific surface area. They carried out not only experimental but also modeling study. Their model described the transition zone between depth filtration and cake filtration, and also penetration profile [6].

J.C. Ruiz et. al studied the potentiality of symmetric ceramic filters for efficient air filtration, and pointed out the parameters to take into account for defining their properties. The evolution of particle penetration and pressure drop was investigated as a function of pore size, membrane thickness and air flow velocity. The

test was carried out with three types of ceramic compositions to capture sodium chloride particles in the range of 0.01-0.7 micron in diameter. Besides, a linear variation of the pressure drop versus the face velocity and a logarithmic variation as a function of CAF thickness were observed, along with the influence of pore diameter on the penetration and pressure drop. Interesting result is a specific correlation between the characteristics of the filter media and the filtration velocity with an acceptable pressure drop [7].

2.2 Simulation

J.H Choi et. al carried out experimental work in a hot bench unit as well as simulation of the corresponding fluid flow around the pulse nozzle at steady state. Operated at 400 to 600 °C, the bench scale unit employed oil combustion gas and fly ash. The simulation study was carried out using the FLUENT code and the k- ϵ turbulent flow model of Re-normalization Group (RNG). In order to simulate the flow dynamics of the air pulse cleaning, the axial symmetric equation of Navier - Stokes at steady state was solved numerically. The pressure drop through the filter element was calculated using Darcy's law [8].

C. Stocklmayer and W. Hoflinger applied mathematical modeling and computer simulation to the investigation of the influence of two key parameters - the filtration velocity and the maximum pressure drop. It was found that the residual pressure drop of the filter mainly depends on the compressibility of the dust cake, which successively builds-up on the surface the filter medium with every new filtration cycle. Here the compressibility of the dust cake is defined as the relation between the cake compression pressure and withstandable stress. The effect of the two operational parameters (the filtration velocity and maximum pressure drop) on these two variables (residual pressure drop and dust-cake compressibility) were investigated [9].

A. Aroussi et. al examined, through experimental and computational modeling, the deposition process and the factors that affect the build-up of the filter cake of a single filter element in cross-flow and parallel flow. For both flow regimes the validation of the computational study was adequate and a method was developed for predicting the filter cake growth using CFD data. An experimental and

computational investigation was also conducted into the particle trajectories in the vicinity of a single filter element in cross-flow and parallel flow. The filter cake formed on a filter element operating predominantly in cross-flow has the same particle size distribution as that in the approaching gas stream. Deposition is essentially uniform. Whether the flow is predominantly parallel to the filter element, the filter cake will be size-differentiated according to vertical and circumferential positions on the filter face. It is likely that the cleaning process will significantly influence the cake composition [10].

A. Karadimos and R. Ocone presented a simple model for the loading process of aerosol particles on fibrous filters with the aim to show the influence that the flow recalculation around a single fibre has on the complete loading process, up to the final clogging of the filter. At each loading stage, the change of shape of the fibre is presented, and information on the flow field around the fibre and the resulting filter efficiency were obtained. The effect of the flow recalculation on the filter efficiency showed that the single fibre efficiency would be overestimated when the effect of further deposition was neglected. To perform the study, they developed a CFD code and combined it with particle trajectory simulations. The effect of the fluid flow recalculation on particle deposition in a fibrous filter has been investigated by solving both the flow of the carrier gas and the motion of the particles past the fibre. The results were combined to show the effect of the dendrites on the flow and to consider the influence this has on the efficiency of the filter. The experimentally observed increase of efficiency, as loading increases, was predicted. A slower increase of particle capture and single fibre efficiency was observed with time; this can be attributed to the interactions between deposited particles and gas flow around them [11].

A. Dittler et. al reported that rigid ceramic filter media widely used for the removal of particles from gas streams at elevated temperature tend to show patchy cleaning when the filter regeneration is incomplete. They also obtained reasonable comparison of the regeneration behavior between modeling and experimental results during the next filtration cycle. The fair agreement of modeling with experiment indicates that the model has real predictive capability for operational filter cleaning.

Both filter conditioning and dust cake compression significantly influence the operational performance of partially regenerated filter media [12].

T.G. Chuah, C.J. Withers and J.P.K. Seville used a cylindrical filter and tapered filter to investigate both the filtration and the reverse flow process at normal conditions. The positions which were used to measure the pressure difference across the filter at various points along the filter were the tapping tubes and micromanometer. For the numerical integration, a computer code is employed using FORTRAN 90. Their work predicted the gas flow along the ceramic candle filter by assuming one-dimensional steady state flow. For the tapered filter, the model's prediction was shown to have good agreement with their experimental data. Moreover, the friction factor term which affects the momentum term in the model had a strong influence on the reverse flow case [13].

Y. Awni and A. Ootom predicted the deposited cake thickness on a ceramic candle filter by considering the number of dust particles deposited and their size distribution which were analyzed statistically. Using a random size distribution of the particles, the model predicted the manners in which the collection efficiency, the porosity, and the pressure drop across the filter change with the filtration time in several filter types. The model was shown to be capable of predicting the cake thickness and pressure drop which agreed with the experimental data [14].

Z. Ji, M. Shi and F. Ding investigated a pulse-jet generating system. To calculate the mass consumption of compressed gas per pulse, the gas flow from the reservoir was treated as an adiabatic process. Based on the theory of flow transients and thermodynamic relations, a dynamic model was presented for the pulse-generating system consisting of the pulse gas reservoir, nozzle, solenoid valve and connecting pipelines. The model is said to constitute a requisite tool for optimizing the pulse cleaning operation and predicting the performance of the pulse cleaning system [15].

Three filter media with very different physical properties are used in the work by S. Calle et. al during clogging and cleaning cycles was developed. The model determined the cleaned fraction at each cycle with the assumption of patchy cleaning. In this study, they determined the pattern of a parameter representative of cleaning, namely the cleaned fraction, from experimental values of the residual pressure drop of

a filter medium. However, it had limitation in case of certain treatment undergone by the medium to increase its regeneration capabilities. Moreover, it was based on the assumption of ideal patchy cleaning presenting either totally cleaned or non-cleaned areas, which is far from reality [16].

C.B. Neiva et. al carried out experiments under coal gasification conditions assuming that the gas velocity was constant and that the layers were formed in equal time interval. They used Darcy's law, the Happel cell model and the Carman-Kozeny equation in calculating the pressure drop during the build-up of dust filter cakes. The adjustment of the cake properties took into account through a constitutive equation the compressive stress which arose from the cumulative drag forces due to gas flow acting on the cake particles. The introduction of an empirical setting factor in the method brought the results closer to the experimental values in all three cases [17].



CHAPTER III

THEORY

3.1 Pressure drop of ceramic filter

The total pressure drop of the system can be considered as the summation of the pressure drops across the clean ceramic candle filter and across the dust cake layer as shown in Equation (3.1).

$$\Delta P_{total} = \Delta P_{filter} + \Delta P_{dust\ cake} = (\xi + m\alpha)\mu v \quad (3.1)$$

Then

$$\Delta P_{total} = \frac{(\xi + m\alpha)\mu Q}{A} = (R_{filter} + R_{cake})Q \quad (3.2)$$

From equation (3.2) we can derive the relationship between the filter resistance (R_{filter}) and the specific resistance of filter (ξ) as shown in equation (3.3). Similarly, the relationship between the cake resistance (R_{cake}) and the specific resistance of dust cake (α) is shown in equation (3.4).

$$R_{filter} = \frac{\mu\xi_{filter}}{A} \quad (3.3)$$

$$R_{cake} = \frac{\mu m\alpha}{A} \quad (3.4)$$

The porosity of the filtration cake is a very important structural parameter, as the pressure drop in the filter and the necessary forces for the removal of the deposited powder layer depend on it. The average porosity of a cake obtained from these equations could be used for estimating the medium porosity with reasonable accuracy. Of the equations investigated, the well known Ergun correlation is the one which presented the best results and would be used here for estimating cake porosity. For a particle layer of thickness L , composed of particles with mean diameter d_p , the Ergun correlation for the pressure drop can be written as equation (3.5)

$$\frac{\Delta P}{L} = \frac{150(1-\varepsilon^2)}{\varepsilon^3} \frac{\mu V_f}{d_p^2} + \frac{1.75(1-\varepsilon)}{\varepsilon^3} \frac{\rho V_f^2}{d_p} \quad (3.5)$$

where ε is the mean porosity of the layer. μ is the gas viscosity and ρ is the density of gas. The assumptions of these equations are as follows:

1. The collection efficiency is essentially 100 percent.
2. Dust cake is incompressible.

The pressure drop will be dependent on the operating time and cleaning (pulse-jet) duration time as shown in Figure 3.1 .Also, the pressure drop will depend on the frequency of cleaning and the number of filter candles.

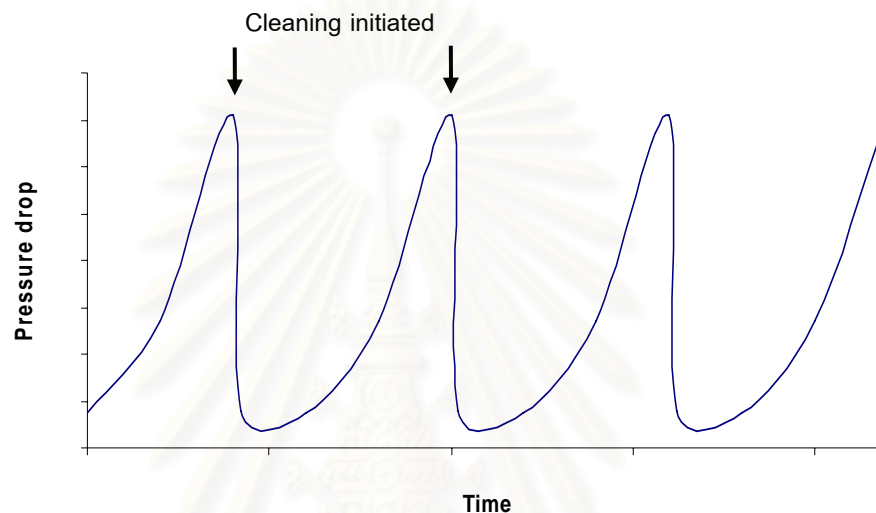


Figure 3.1 Trend of the pressure drop in a single-candle system

3.2 Efficiency of particle collection

In a dust collection system, particles will be separated from the gas stream by settling or impact and get trapped at the medium. The particle collection efficiency of dust collection system can be considered in the form of dust separated and collected by that instrument. On the other hand, we can consider the form of dust escaping from the system which is called penetration. The definitions of particle collection efficiency and penetration are illustrated in Equations (3.6) and (3.7).

$$\text{Efficiency of particle collection} \quad \eta = 1 - \frac{C_{out}}{C_{in}} \quad (3.6)$$

$$\text{Penetration} \quad \pi = 1 - \eta \quad (3.7)$$

3.3 Computational Fluid Dynamics (CFD)

Computational Fluid Dynamics or CFD is the analysis of systems involving fluid flow, heat transfer and associated phenomena such as chemical reactions by

means of computer-based simulation. This technique is very powerful and spans a wide range of industrial and non-industrial application areas. The ultimate aim of developments in CFD field is to provide a capability comparable to other computer-aided engineering tools. The variable cost of an experiment is proportional to the number of data points and the number of configurations tested. In contrast CFD codes can produce extremely large volumes of results at virtually no added expense and it is very cheap to perform parametric studies, for instance optimize equipment performance.

3.4 Commercial software used for CFD

Each software package aimed at the CFD market has to assist the user in carrying out the tasks that form the analysis process. This is done by providing, typically, three main pieces of software together with a variety of utility programs as follows.

- Pre-processing program
- Processing program
- Post-processing program

The use of all these programs will be explained below.

3.4.1 Pre-processing program

All the tasks that take place before the starting of the numerical solution process are called “pre-processing”. This includes the first three phases of the analysis process that consisted of thinking, mesh generation and defines the numerical control parameters. While the first phase needs considerable thought, and considerable engineering judgement, if the physical flow problem is to be translated into a problem that is solvable by the CFD software it does not involve any computing. It is only when this first phase has been completed that the computing starts.

To assist in the computational part of the pre-processing phase, most software packages have a pre-processing program that can be used to carry out the following operations:

- Define a grid of points and perhaps volumes or elements.
- Define the boundaries of the geometry.

- Apply the boundary conditions.
- Specify the initial conditions.
- Set the fluid properties. .
- Set the numerical control parameters.

In carrying out these tasks the user has to interact with the computer in some way. Since the pre-processing program usually has a graphical interface, so that parameters can be set and the resulting changes seen quickly. This is particularly important when the mesh is being built.

The most difficult task in the pre-processing phase is the generation of the grid of points or mesh. It is often that this task can be simplified by using software which has been especially designed to carry out mesh generation. One example of this is the use of programs written to produce meshes suitable for the finite element analysis of structural problems. Some software, such as GAMBIT, is commonly available and can interface with computer-aided design systems. This allows the analyst to access computer models of objects, the surface data of which can form the basis for the geometry around which the mesh for a CFD simulation can be built.

3.4.2 Processing program

Each package has a program that solves the numerical equations for the problem under consideration. This program must be given all the relevant data that has been defined by the pre-processing program. To transfer the data between the programs, the pre-processing program writes out data files that the processing program can read. These files can also be moved, if necessary, between computers. This is extremely useful as it means that the processing program can run on a machine specifically designed for high speed numerical work while the interactive tasks are carried out on a smaller machine. This splitting of the tasks between machines enables the hardware to be used in the most efficient manner. Once the data files are in place, the processing program is activated and the required solution process carried out. At the end of this phase, further data files will be available, which may have to be transferred back to the machine where the pre- and post-processing programs are run.

FLUENT is one of the most favorite processing programs using for modeling fluid flow and heat transfer in complex geometry. FLUENT also allows refining or coarsening the finite-difference grid based on the flow solution. This solution-adaptive grid capability is particularly useful for accurately predicting flow fields in regions with large gradients. Solution-adaptive refinement makes it easier to perform grid refinement studies and reduces the computational effort required to achieve a desired level of accuracy.

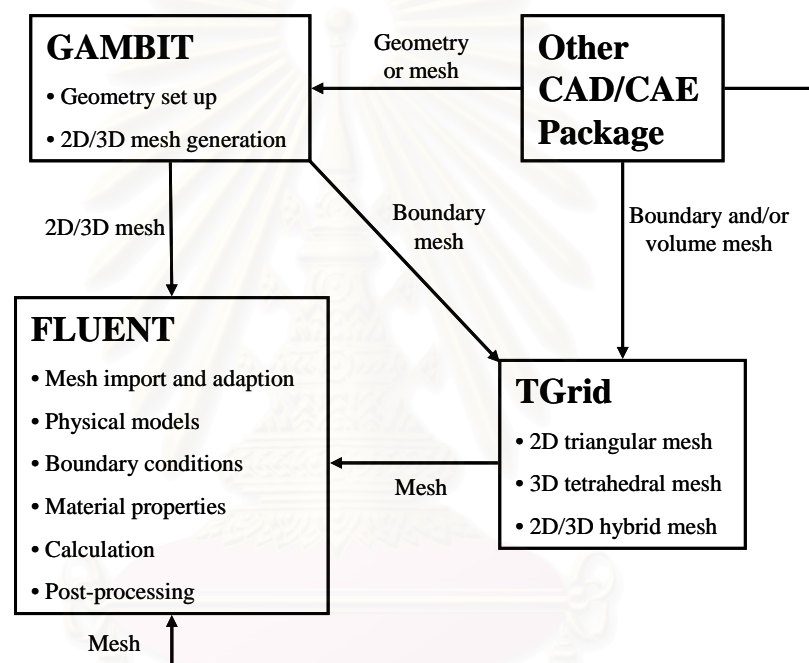


Fig 3.2 Basic Program Structure of FLUENT

FLUENT employs unstructured meshes in order to reduce the amount of time spent on generating meshes, simplify the geometry modeling and mesh generation process, and model more complex geometries than we can handle with conventional, multi-block structured meshes. It also let us adapt the mesh to resolve the flow-field features. FLUENT is capable of handling triangular and quadrilateral elements (or a combination of the two) in 2D, and tetrahedral, hexahedral, pyramid and wedge elements (or a combination of these) in 3D. This flexibility allows picking mesh topologies that are best suited for the particular application. We can adopt all types of meshes in FLUENT in order to resolve large gradients in the flow field, but we must

always generate the initial mesh (whatever the element types used) outside of the solver, using pre-processing program for which mesh import filters exist.

The solving steps of FLUENT is as follows

- 1 Create the model geometry and grid.
- 2 Start the appropriate solver for 2D or 3D modeling.
- 3 Import the grid.
- 4 Check the grid.
- 5 Select the solver formulation.
- 6 Choose the basic equations to be solved:
 - Laminar or turbulent, chemical species or reaction, heat transfer models, etc.
 - Identify additional models needed: fans, heat exchangers, porous media, etc.
- 7 Specify material properties.
- 8 Specify the boundary conditions.
- 9 Adjust the solution control parameters.
- 10 Initialize the flow field.
- 11 Calculate a solution.
- 12 Examine the results.
- 13 Save the results.
- 14 If necessary, refine the grid or consider revisions to the numerical or physical model.

3.4.3 Post-processing program

As large numbers of points have to be created within the flow domain if reasonable simulations are to be obtained, and as several variables are stored at these points, computer graphics is often the only means of assessing the data written by the processing program. The post-processing program is used to display the results, and, as with the pre-processing program, this program is interactive and so is usually run on the same machine as the pre-processing program. Typical pictures obtained with the post-processing program might contain a section of the mesh together with vector plots of the velocity field or contour plots of scalar variables such as pressure. These pictures enable global trends in the data to be seen.

3.5 Modeling Turbulence

Turbulent flows are characterized by fluctuating velocity fields. These fluctuations mix transported quantities such as momentum, energy, and species concentration, and cause the transported quantities to fluctuate as well. Since these fluctuations can be of small scale and high frequency, they are too computationally expensive to simulate directly in practical engineering calculations. Instead, the instantaneous (exact) governing equations can be time-averaged, ensemble-averaged, or otherwise manipulated to remove the small scales, resulting in a modified set of equations that are computationally less expensive to solve. However, the modified equations contain additional unknown variables, and turbulence models are needed to determine these variables in terms of known quantities.

FLUENT provides many choices of turbulence models. It is an unfortunate fact that no single turbulence model is universally accepted as being superior for all classes of problems. The choice of turbulence model will depend on considerations such as the physics encompassed in the flow, the established practice for a specific class of problem, the level of accuracy required, the available computational resources, and the amount of time available for the simulation. In this work, we will use k- ϵ model to make the appropriate model for the system.

3.5.1 RNG k- ϵ model

The simplest “complete models” of turbulence are two-equation models in which the solution of two separate transport equations allows the turbulent velocity and length scales to be independently determined. The standard k- ϵ model in FLUENT falls within this class of turbulence model and has become the workhorse of practical engineering flow calculations. Robustness, economy, and reasonable accuracy for a wide range of turbulent flows explain its popularity in industrial flow and heat transfer simulations. As the strengths and weaknesses of the standard k- ϵ model have become known, improvements have been made to the model to improve its performance. One of these variants available in FLUENT is the RNG k- ϵ model. The RNG k- ϵ model was derived using a rigorous statistical technique (called

renormalization group theory). It is similar in form to the standard k - ε model, but includes the following refinements:

- The RNG model has an additional term in its ε equation that significantly improves the accuracy for rapidly strained flows.
- The effect of swirl on turbulence is included in the RNG model, enhancing accuracy for swirling flows.
- The RNG theory provides an analytical formula for turbulent Prandtl numbers, while the standard k - ε model uses user-specified, constant values.
- While the standard k - ε model is a high-Reynolds-number model, the RNG theory provides an analytically-derived differential formula for effective viscosity that accounts for low-Reynolds-number effects. Effective use of this feature does, however, depend on an appropriate treatment of the near-wall region.

These features make the RNG k - ε model more accurate and reliable for a wider class of flows than the standard k - ε model. The RNG-based turbulence model is derived from the instantaneous Navier-Stokes equations, using a mathematical technique called “renormalization group” (RNG) methods. The analytical derivation results in a model with constants different from those in the standard k - ε model, and additional terms and functions in the transport equations for k and ε .

3.5.2 Governing equations

The mass and momentum equations derived from the conservation principles are given for the unsteady-state flow in the form of time-averaged variables.

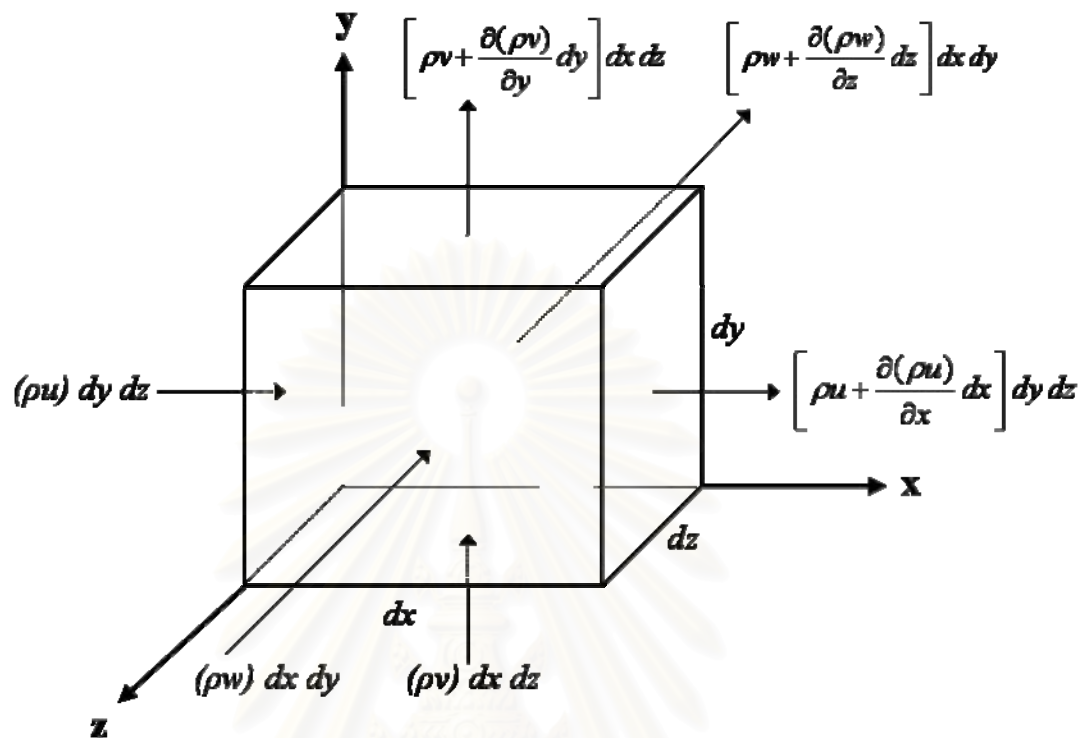


Fig. 3.3 The mass flux in and out of the fixed volume element through which a fluid is flowing ($u=v_x$, $v=v_y$, $w=v_z$)

3.5.2.1 Continuity Equation

$$\frac{\partial \rho}{\partial t} + \frac{\partial}{\partial x}(\rho v_x) + \frac{\partial}{\partial y}(\rho v_y) + \frac{\partial}{\partial z}(\rho v_z) = 0 \quad (3.8)$$

สถาบันวิทยบริการ
จุฬาลงกรณ์มหาวิทยาลัย

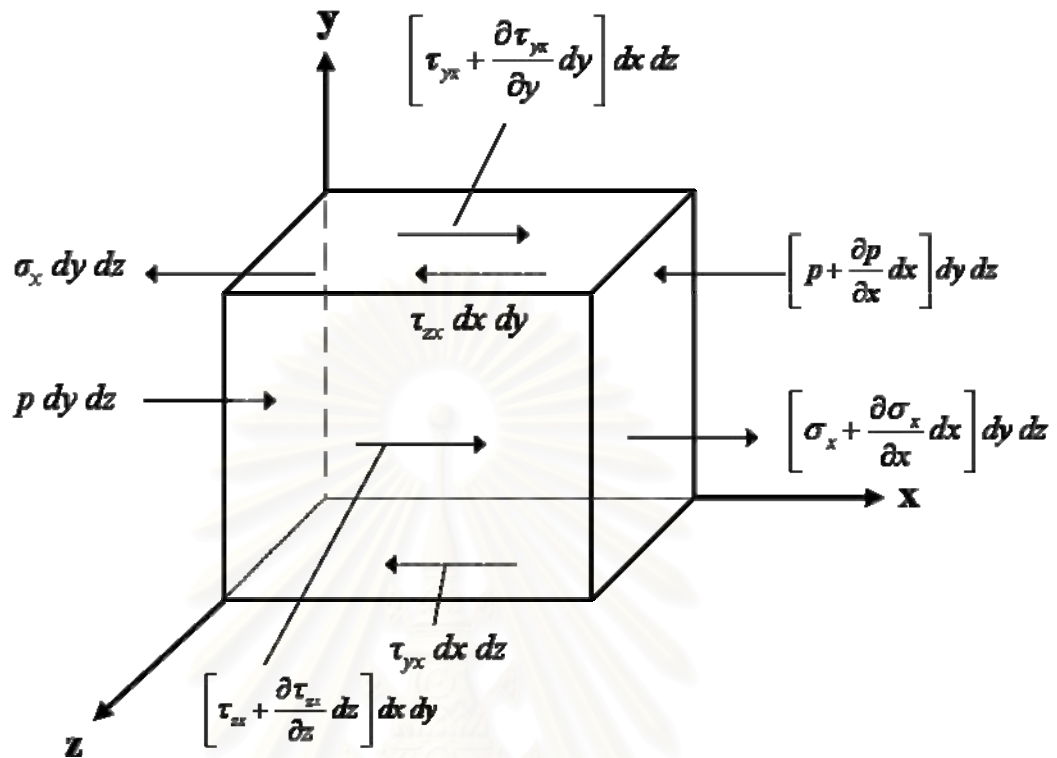


Fig. 3.4 The momentum flux in and out of the fixed volume element through which a fluid is flowing

3.5.2.2 Momentum Equation

X-component:

$$\frac{\partial}{\partial t}(\rho v_x) + \frac{\partial}{\partial x}(\rho v_x v_x) + \frac{\partial}{\partial y}(\rho v_y v_x) + \frac{\partial}{\partial z}(v_z v_x) = -\frac{\partial p}{\partial x} + \mu \left[\frac{\partial^2 v_x}{\partial x^2} + \frac{\partial^2 v_x}{\partial y^2} + \frac{\partial^2 v_x}{\partial z^2} \right] + \rho g_x$$

Y-component:

$$\frac{\partial}{\partial t}(\rho v_y) + \frac{\partial}{\partial x}(\rho v_x v_y) + \frac{\partial}{\partial y}(\rho v_y v_y) + \frac{\partial}{\partial z}(v_z v_y) = -\frac{\partial p}{\partial y} + \mu \left[\frac{\partial^2 v_y}{\partial x^2} + \frac{\partial^2 v_y}{\partial y^2} + \frac{\partial^2 v_y}{\partial z^2} \right] + \rho g_y$$

Z-component:

$$\frac{\partial}{\partial t}(\rho v_z) + \frac{\partial}{\partial x}(\rho v_x v_z) + \frac{\partial}{\partial y}(\rho v_y v_z) + \frac{\partial}{\partial z}(v_z v_z) = -\frac{\partial p}{\partial z} + \mu \left[\frac{\partial^2 v_z}{\partial x^2} + \frac{\partial^2 v_z}{\partial y^2} + \frac{\partial^2 v_z}{\partial z^2} \right] + \rho g_z$$

(3.9)

3.5.2.3 Energy Equation

The total energy of a control volume consists of internal energy, kinetic energy and potential energy.

$$\frac{\partial(\rho E)}{\partial t} + \nabla \cdot (\bar{v}(\rho E + p)) = \nabla \cdot \left(k_{eff} \nabla T - \sum_j h_j \bar{J}_j + (\bar{\tau}_{eff} \cdot \bar{v}) \right) + S_h \quad (3.10)$$

3.5.2.4 Equation for turbulent kinetic energy (k)

The fluid dynamics model used has been described in detail elsewhere. A turbulence model is adopted here because of the high Reynolds number of the influent fluid velocity ($Re \approx 2400-9100$). The k- ϵ turbulence model has two constituent equations. Equations (3.11) and (3.12) for k and ϵ , and the methods of calculating the turbulent viscosity and model constants are as follows. The assumption of isotropic turbulence is considered appropriate. The present turbulence model is the renormalization group (RNG) k- ϵ model, and its formulation is derived from strict mathematical rules covering rotation or swirl in the mean flow. The RNG model in FLUENT provides a tool to account for the effects of swirl or rotation by modifying the turbulent viscosity appropriately.

$$\frac{\partial}{\partial t}(\rho k) + \frac{\partial}{\partial x_i}(\rho k u_i) = \frac{\partial}{\partial x_j} \left(\alpha_k \mu_{eff} \frac{\partial k}{\partial x_j} \right) + G_k + G_b - \rho \epsilon - Y_M + S_k \quad (3.11)$$

3.5.2.5 Equation for dissipation rate of turbulent kinetic energy (ϵ)

$$\frac{\partial}{\partial t}(\rho \epsilon) + \frac{\partial}{\partial x_i}(\rho \epsilon u_i) = \frac{\partial}{\partial x_j} \left(\alpha_\epsilon \mu_{eff} \frac{\partial \epsilon}{\partial x_j} \right) + C_{1\epsilon} \frac{\epsilon}{k} G_k - C_{2\epsilon} \rho \frac{\epsilon^2}{k} - R_\epsilon + S_\epsilon \quad (3.12)$$

3.5.3 Porous media model for ceramic candle filter

The porous media model can be used for a wide variety of problems, including flows through packed beds, filter papers, filter, flow distributors, and tube banks. When this model is used, we have to define a cell zone in which the porous media model is applied and the pressure drop in the flow is determined. The porous media

model incorporates an empirically determined flow resistance in a region of model defined as “porous”. By default FLUENT calculates the superficial velocity based on volumetric flow rate. The superficial velocity in the governing equations can be represented as

$$\vec{v}_{\text{superficial}} = \gamma \vec{v}_{\text{physical}} \quad (3.13)$$

The superficial velocity values within the porous region remain the same as those outside of the porous region. This limits the accuracy of the porous model where there should be an increase in velocity throughout the porous region. For more accurate simulations of porous media flows, it becomes necessary to solve for the true, or physical velocity throughout the flow field, rather than the superficial velocity.

FLUENT calculates the flow through a porous medium with the input of permeability and porosity of the porous medium and the thermal properties of the solid and fluid. The porosity, fluid density, thermal conductivity and specific heat were assumed to be constant throughout a simulation.

3.5.3.1 Continuity equation for flow through the porous medium

$$\frac{\partial(\varepsilon_p \rho)}{\partial t} + \frac{\partial(\varepsilon_p \rho v_x)}{\partial x} + \frac{\partial(\varepsilon_p \rho v_y)}{\partial y} + \frac{\partial(\varepsilon_p \rho v_z)}{\partial z} = 0 \quad (3.14)$$

3.5.3.2 Momentum equation for flow through the porous medium

$$\frac{\partial(\varepsilon_p \rho \vec{v})}{\partial t} + \nabla \cdot (\varepsilon_p \rho \vec{v} \vec{v}) = -\varepsilon_p \nabla p + \nabla \cdot (\varepsilon_p \vec{\tau}) + \varepsilon_p \vec{B}_f - \left(\frac{\mu}{\alpha} + \frac{C_2 \rho}{2} |\vec{v}| \right) \vec{v} \quad (3.15)$$

3.5.3.3 Energy equation for flow through the porous medium

$$\frac{\partial}{\partial t} (\varepsilon_p \rho_f E_f + (1 - \varepsilon_p) \rho_s E_s) + \nabla \cdot (\vec{v} (\rho_f E_f + p)) = \nabla \cdot \left(k_{\text{eff}} \nabla T - \sum_i h_i \vec{J}_i + (\vec{\tau} \cdot \vec{v}) \right) + S_f^h \quad (3.16)$$

The effective thermal conductivity is computed as the volume average of the fluid conductivity and the solid conductivity as follows.

$$k_{eff} = \varepsilon_p k_f + (1 - \varepsilon_p) k_s \quad (3.17)$$

The pressure drop across the porous medium is modeled by the addition of a momentum source term to the standard fluid flow equations, equation (3.9). The source term is composed of two parts:

1. A viscous loss term (Darcy, the first term on the right-hand side of Equation (3.18))
2. An inertial loss term (the second term on the right-hand side of Equation (3.18))

$$S_i = - \left(\frac{\mu}{\alpha} v_i + \psi \frac{1}{2} \rho |v| v_i \right) \quad (3.18)$$

S_i incorporates the additional pressure gradient in the porous medium. In laminar flow through the porous medium, the pressure drop is typically proportional to the velocity and the constant ψ in equation (3.18) can be considered to be zero. Ignoring convective acceleration and diffusion, the porous media model then reduces to Darcy's Law:

$$\nabla p = - \frac{\mu}{\alpha} \vec{v} \quad (3.19)$$

3.6 Discretization

FLUENT uses a control-volume-based technique to convert the governing equations to algebraic equations that can be solved numerically. This control volume technique consists of integrating the governing equations about each control volume, yielding discrete equations that conserve each quantity on a control-volume basis. Triangular cell shown in Figure 3.5 is an example of such a control volume.

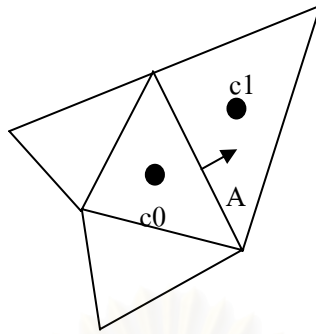


Figure 3.5 Control Volume Used to Illustrate Discretization of a Scalar Transport Equation

Discretization of the governing equations can be illustrated most easily by considering the steady-state conservation equation for transport of a scalar quantity ϕ . This is demonstrated by the following equation written in integral form for an arbitrary control volume V as follows:

$$\sum_f^{N_{\text{faces}}} \rho_f \vec{v}_f \phi_f \cdot \vec{A} = \sum_f^{N_{\text{faces}}} \Gamma_\phi (\nabla \phi)_n \cdot \vec{A}_f + S_\phi V \quad (3.20)$$

By default, FLUENT stores discrete values of the scalar ϕ at the cell centers (c_0 and c_1 in Figure 3.5). However, face values ϕ_f is required for the convection terms in Equation (3.20) and must be interpolated from the cell center values. This is accomplished using an upwind scheme. “Upwind” means that the face value ϕ_f is derived from quantities in the cell upstream, or upwind relative to the direction of the normal velocity v_n in Equation (3.20). In FLUENT, several upwind schemes can be chosen: first-order upwind, second-order upwind, power law, and QUICK.

3.7 Under-relaxation factor

During the iterative solution of an algebraic equation or in the overall iterative scheme employed for handling nonlinearity, it is often desirable to speed up or to slow down the estimated changes, from iteration to iteration, in the values of the dependent variables. This process is called under-relaxation. Under-relaxation is a very useful device for nonlinear problems. It is often employed to avoid divergence in the iterative solution of strongly nonlinear equations. There are numerous ways of

introducing under-relaxation. Because of the nonlinearity of the equation set being solved by FLUENT, it is necessary to control the change of a dependent variable ϕ . This is typically achieved by under-relaxation, which reduces the change of ϕ produced during each iteration. In a simple form, the new value of the variable ϕ within a cell depends upon the old value, ϕ_{old} , the computed change in ϕ , $\Delta\phi$, and the under-relaxation factor (α) as follows

$$\phi = \phi_{old} + \alpha\Delta\phi \quad (3.21)$$

Here, $0 < \alpha < 1$

Several iterations of the solution loop shown in Fig.10 must be performed before a converged solution is obtained. The iteration is continued until the convergence criteria are satisfied.

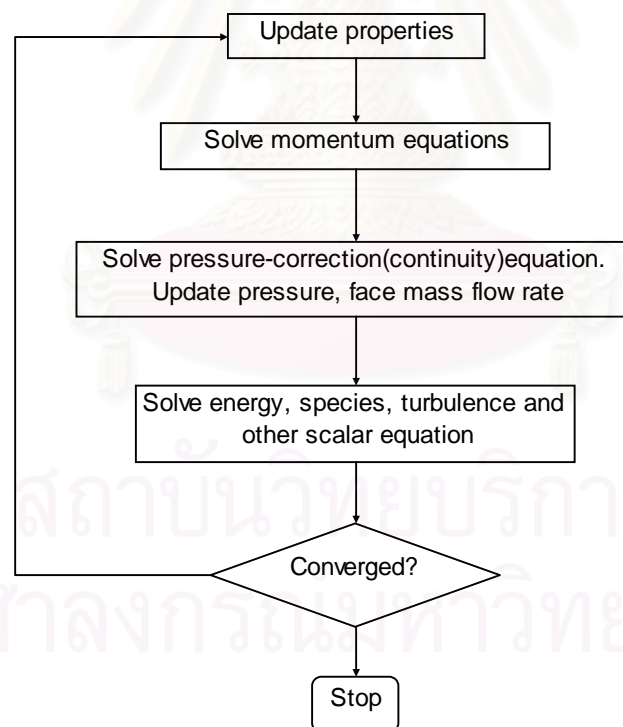


Fig. 3.6 Overview of the segregated solution method

Occasionally, you may want to make changes in the under-relaxation factors and resume your calculation, only to find that the residuals begin to increase. This often results from increasing the under-relaxation factors too much. A cautious

approach is to save a data file before making any changes to the under-relaxation factors, and to give the solution algorithm a few iterations to adjust to the new parameters. Typically, an increase in the under-relaxation factors brings about a slight increase in the residuals, but these increases usually disappear as the solution progresses. If the residuals jump by a few orders of magnitude, you should consider halting the calculation and returning to the last good data file saved.



สถาบันวิทยบริการ
จุฬาลงกรณ์มหาวิทยาลัย

CHAPTER IV

MODELING AND SIMULATION

Ideally the developed model of a high-temperature ceramic filter should be able to predict microscopically the dust cake formation, which directly determines the aerosol collection process and the corresponding pressure drop characteristics. However, the stochastic particle-by-particle cake formation process is infeasible to simulate when the actual aerosol is not only non-spherical but also irregular in shape and polydisperse in size. Moreover, the cohesive and adhesive properties of the aerosol particles at high temperature are still not well understood. Therefore the present work will rely on the air flow field to estimate the corresponding thickness of dust cake on the surface of the candle filter, and their effects on the pressure drop.

Once the specification of the flow problem is known, we can turn our attention to build a computer model. Thus, we will build a mesh of points throughout the flow domain and perhaps produce the necessary volumes or elements. Often it is this phase of the analysis process that determines the total time required to obtain results from a simulation, as all the other phases, including the actual computation of the results, can be carried out quite quickly.

4.1 Description of experimental set-up

4.1.1 Filtration rig

Fig. 4.1 illustrates a twin candle filtration unit used for the high temperature gas cleaning by HPTRI, the data of which are used to validate the simulation results given by FLUENT software. The filtration unit consists of two identical porous ceramic candle filter which can withstand up to 400°C in the vessel shown in Fig. 4.2, dust feeder which has the twin screw for preventing the agglomeration of testing dust, pulse jet system and high temperature gas supply unit.

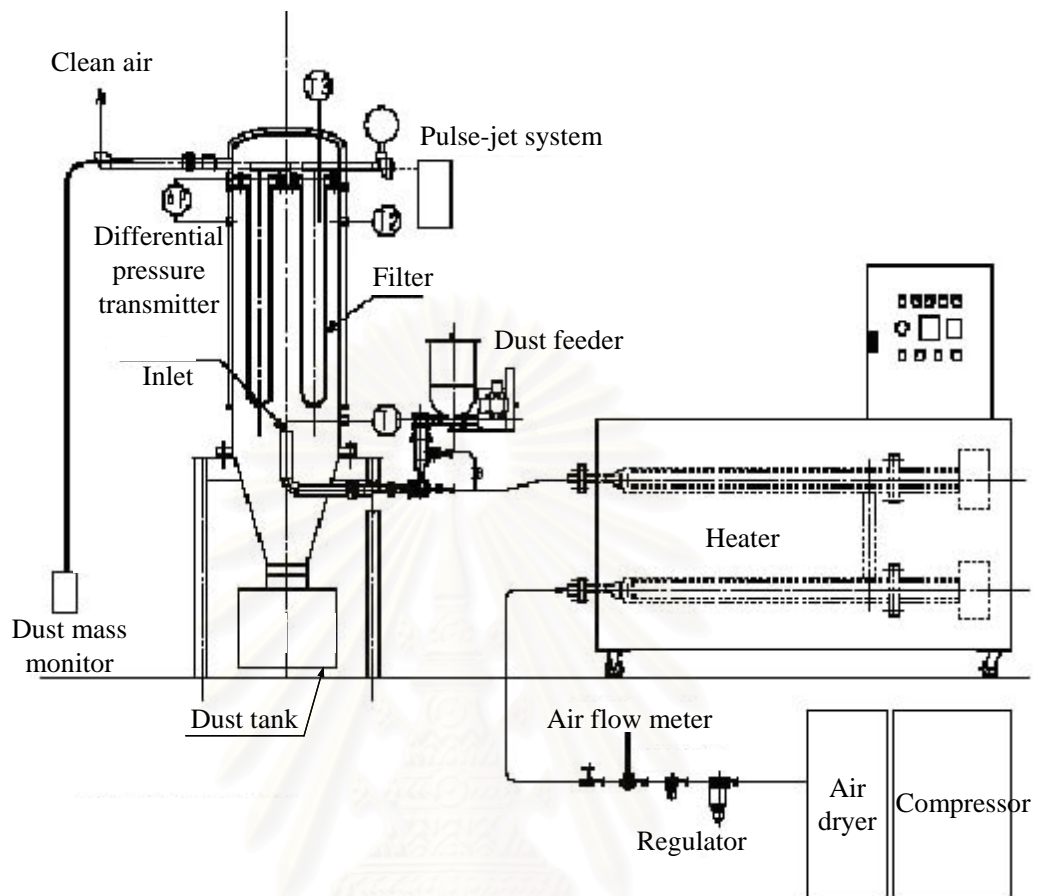


Fig. 4.1 Schematic diagram of the experimental setup by HPTRI.



Fig. 4.2 Photo of ceramic candle filter using in experimental set-up

The specifications of the ceramic candle filter made of ceramic fibers and SiO_2 matrix is illustrated in Table 4.1.

Table 4.1 Specifications of the ceramic candle filter

Outside diameter (mm)	120
Inside diameter (mm)	90
Length of cylindrical portion (mm)	930
Total length (mm)	1000
Filtration area (m ²)	0.38
Wall thickness (mm)	15
Porosity	0.85
Density (kg/m ³)	250

The dust material used were fly ash (JIS No. 10) which had a spherical shape as shown in Fig. 4.3 and carbon black which seem to be agglomerate with others was shown in Fig. 4.4.

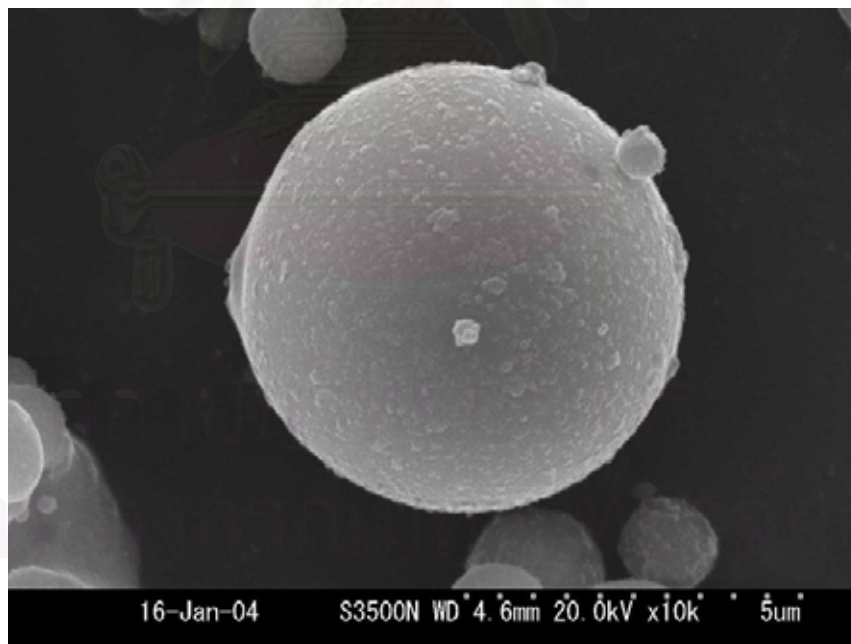


Fig. 4.3 SEM image of testing dust (Fly ash JIS10)

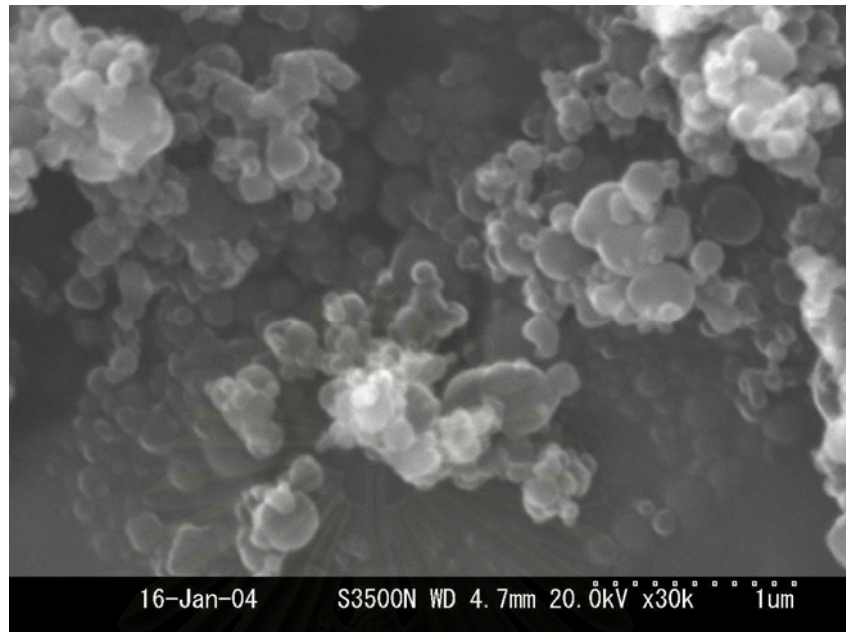


Fig. 4.4 SEM image of testing dust (Carbon black JIS12)

4.1.2 Measurement of average pressure difference

The simulation results in this work are based upon the pressure drop measurements across a candle filter obtained by HPTRI on a data logger at the fixed interval of 20 seconds. In all experimental runs, the total influent flow rate was kept constant while the pressure drop was allowed to vary. Since the experimental data on ΔP consist of a huge quantity of cyclical data as shown in **Fig. 4.5**, we decided to use the average cyclical values to represent the typical data for one cycle as shown in ΔP_A of **Fig. 4.6**.

สถาบันวิทยบริการ
จุฬาลงกรณ์มหาวิทยาลัย

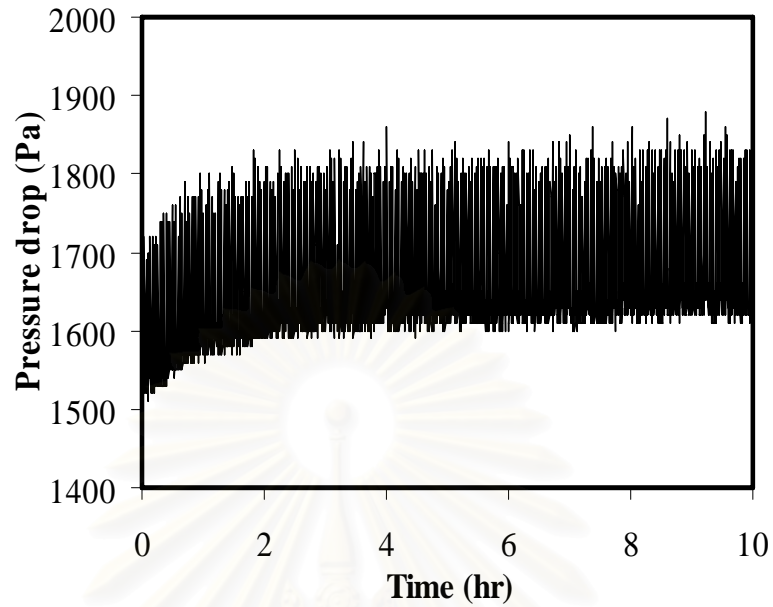


Fig. 4.5 Example of experimental ΔP across filter candle A (Fly ash JIS No.10, average air temperature 543 K, air flow volume 0.38 m³/min, feed dust concentration 5 kg/m³, pulse interval 120 seconds)

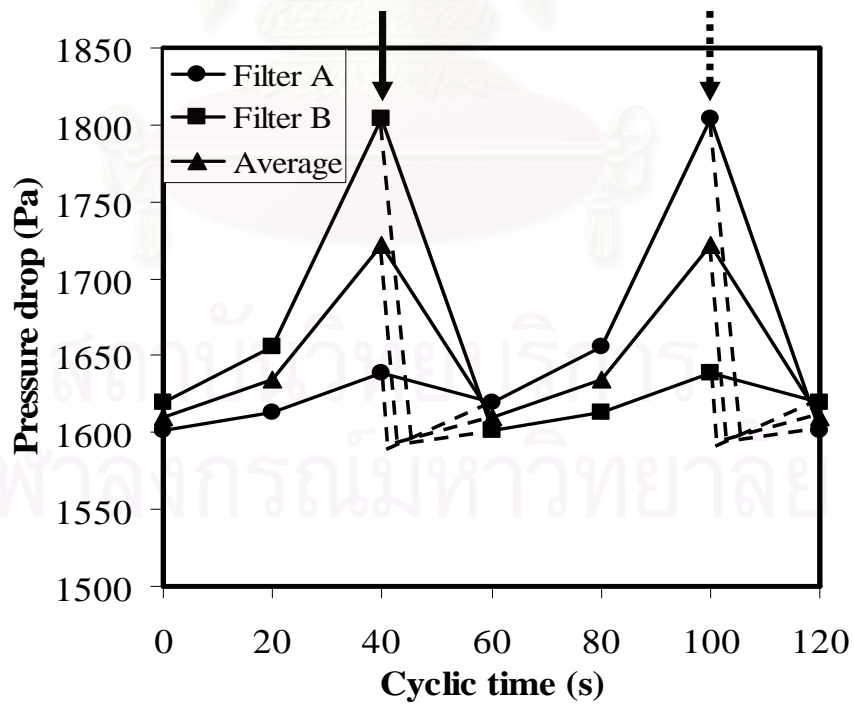


Fig. 4.6 Measured values of ΔP_A , estimated values of ΔP_B and overall ΔP_{av}

To prevent excessive buildup of ΔP_A , compressed air was reversely injected into candle filter A at every 120-second interval to remove the cake layer on its outer surface. The same pulsing frequency was carried out on filter B. The solid and dashed arrows indicate the timings when candle filters A and B, respectively, were pulse-cleaned cyclically. The dash lines indicate the expected changes in the pressure drops upon pulse cleanings if the pressure recordings could be made continuously. Though ΔP_B was not measured, it is reasonable to assume that, because of the system's symmetrical configuration, ΔP_B should have the same time pattern as ΔP_A except for a time shift of 60 seconds. In general, the whole pressure drop and the pressure drops of all candle filters should be the same if the pressure drops in the manifold and those caused by changes in the flow direction etc. are neglected. During pulse cleaning only the candle filter being cleaned should show a different pressure drop unless some interactive effect exists.

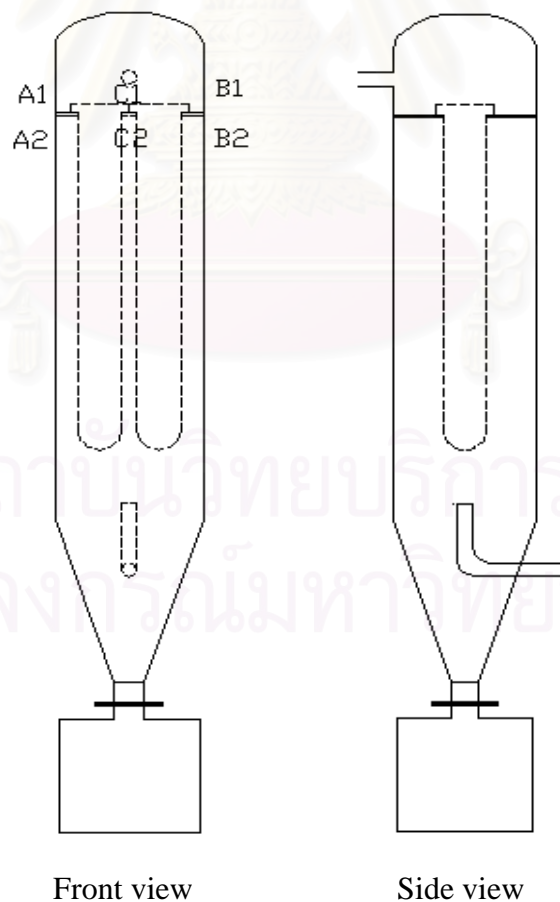


Fig. 4.7 Cross section of filtration unit and positions of pressure drop measurements

According to **Fig. 4.6**, the downstream space of filter A was common to filter B but the relative locations of the two upstream pressure tap ports of both filters were either intercepted by or hidden behind the twin candles. Not only ports A2 and B2 were located too high but our detailed simulation results also do reveal that the local normal face velocities are not uniformly distributed over the entire candle length even when the candle wall resistances are taken to be uniform. These are the reasons why the measured time patterns of ΔP_A and ΔP_B in **Fig. 4.6** did not neatly coincide. As a practical compromise to reduce the observed discrepancy, the correct pressure drops for either candle filter as well as the whole unit were taken to be the average of ΔP_A and ΔP_B in **Fig. 4.6**. As a result, ΔP_{av} in **Fig. 4.6** represents the cyclic pattern of the whole pressure drop over a period of 60 s. Next we consider the instantaneous effect of pulse cleaning of candle filter B, during which ΔP_{av} should drop precipitously at 40 s cyclic time. Since there were not enough data points to indicate how quick or deep the instantaneous drops should be, it was decided to make use of simple linear interpolation between the available data points in **Fig. 4.6**.

4.2 Meshing

In this section, we will discuss the reasons for building a mesh, the requirements that a mesh must satisfy if it is to give satisfactory solutions and the types of mesh that can be built. Then we will discuss how a mesh can be built by using a software tools. Finally, we will look at ways in which a mesh can be modified in the light of the results of a flow simulation such that better results are achieved. The simulation results will be validated using the experimental data obtained by HPTRI (Hosokawa Powder Technology Research Institute). The description of the experimental set-up is explained in the following section.

4.2.1 The need for mesh

There are various ways of discretization the governing partial differential equations of fluid flow so that numerical equations were produced. The mesh of points has to be produced within the volume of the fluid. This can be considered as the discretization of the space in which the flow takes place. The points are arranged

so that they can be grouped into a set of volumes and the partial differential equations can be solved by equating various flux terms through the faces of the volumes. Every flow problem will contain a wide variety of flow features in the domain. That is, things such as boundary layers, regions of rapid fluid velocity and pressure change, and all of these need to be modeled by the CFD simulation. If we have a mesh that is capable of modeling these features, where the gradients in space of the flow variables are high, then we must be aware of where these features might occur. This shows the importance of the mesh that we developed for the specification of the system.

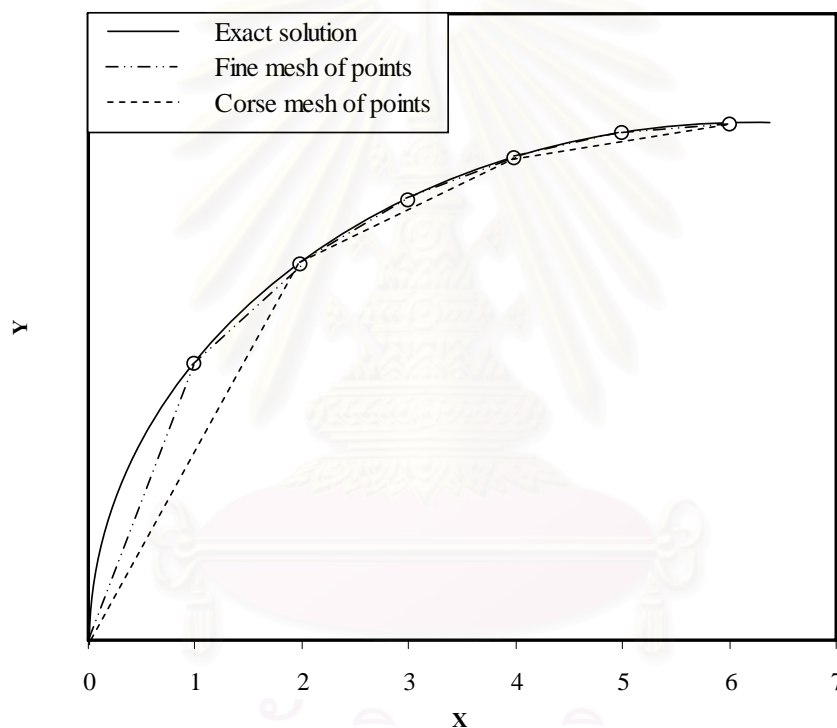


Fig. 4.8 Effect of mesh density

In the critical regions we need to have a large number of points within the mesh. We saw that all the numerical methods assume that the flow variables vary in some simple way between the points or within an element or volume. Consequently, if the flow varies rapidly in space that are the critical regions of the flow, a fine grid will be needed to describe the variation accurately. We can see this clearly in **Fig. 4.8** where a one-dimensional variation in a variable Y is assumed to occur in the X -direction. Assume that some numerical method has given us a set of values for Y which is exact at a number of points in the x -direction. This will never happen in

practice but it is the best that a numerical method can do. If we take the numerical prediction of Y to be the straight lines between these points, then several sources of error in the variation can be seen. First, if the values are obtained at only a few points, which we will call a coarse mesh, then the solution is not an accurate representation of the variation. If we know the values of Y at more points, that is on a finer mesh, then we can see that numerical description of the variation is much more accurate. This is extremely important as we must have accurate values of the variables and their derivatives if we are to simulate the governing equations accurately.

As the conclusion from the previous section, the mesh must be very fine in the critical regions. Along the surface of ceramic candle filter there will be a boundary layer and so there must be several points close to the filter surface in a direction normal to the surface. This allows the numerical solution to model the rapid variation in velocity through the boundary layer.

4.2.2 Building mesh

A mesh must be suitable for the discretization technique and also for the flow in the system. The following are the basic parts from which meshes are built:

1. Points, sometimes called nodes
2. Volumes, also known as cells in some documentation
3. Elements

Various mesh structures which are made up of these parts can be built and have a difference in distinctiveness. Due to the complicated structure of our system, the suitable mesh structure is tetrahedron as shown in **Fig. 4.9**.

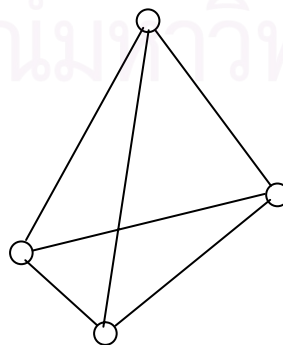


Fig. 4.9 The tetrahedron shape of mesh structure

A CFD package called FLUENT in combination with GAMBIT is used to model and simulate the flow field inside the filtration unit as well as the local gas flow through the wall of each ceramic candle filter. Based on the experimental pressure drop data, the viscous resistance of flow through the filter medium is estimated as a function of cyclic time. The employed 3-dimensional (3D) computational grids for gas flow in the twin-candle filtration unit are shown in **Fig. 4.10, 4.11 and 4.12**. The total number of cells for the calculation is 413,490. In addition, a single-candle model is also employed for comparison and its 3D computational grid is shown in **Fig. 4.13**.

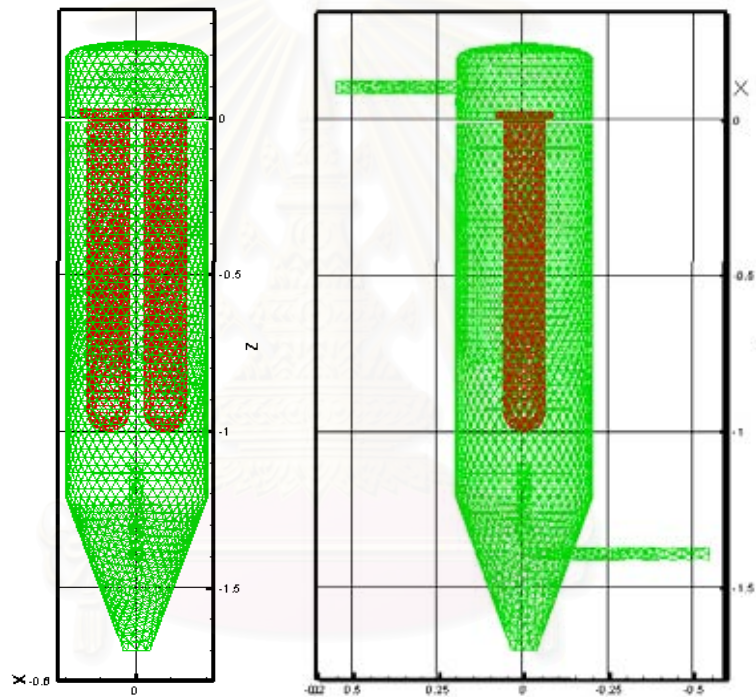


Fig. 4.10 Illustration of the employed computational grid in the twin-candle system feeding from the bottom position

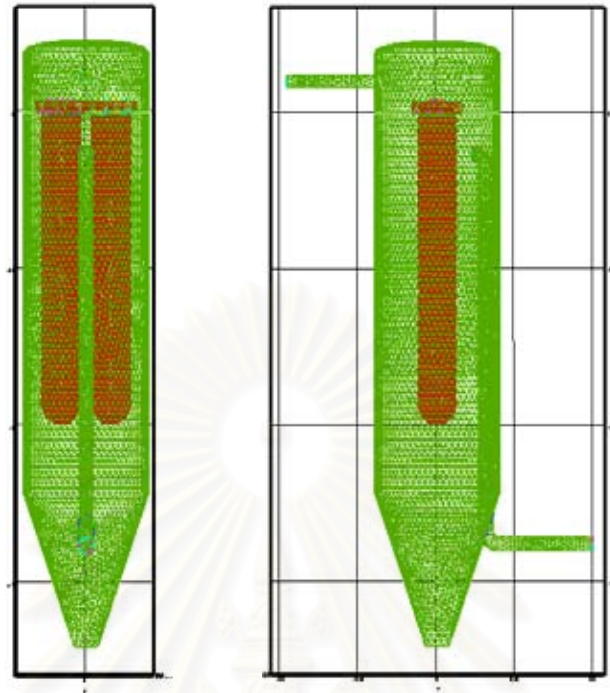


Fig. 4.11 Illustration of the employed computational grid in the twin-candle system feeding from the top position

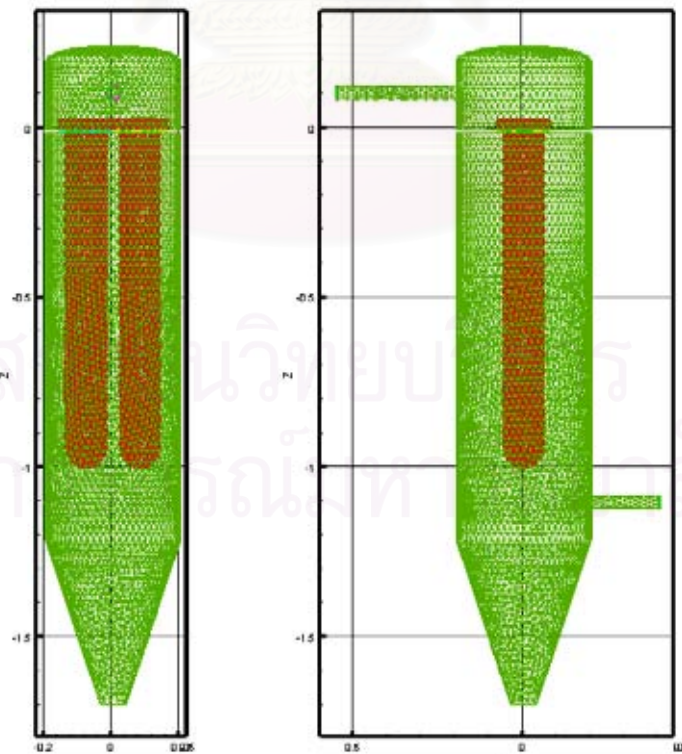


Fig. 4.12 Illustration of the employed computational grid in the twin-candle system feeding from the tangential position

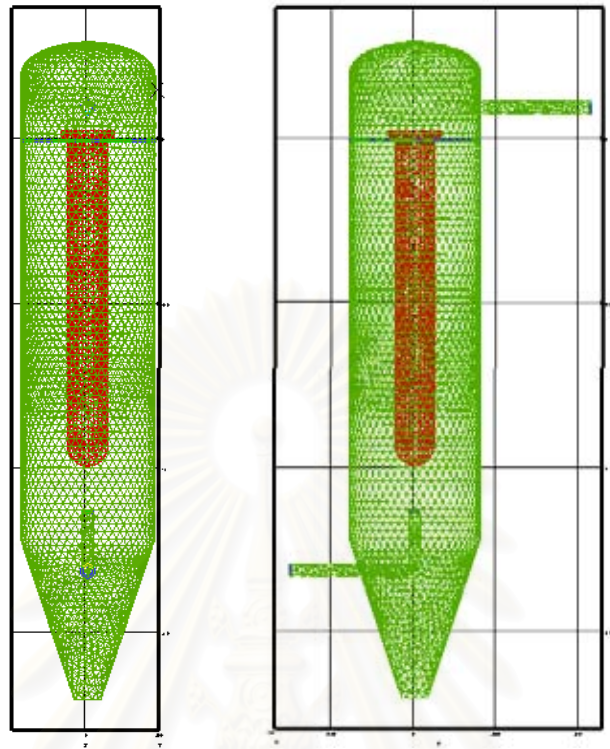


Fig. 4.13 Illustration of the employed computational grid in the single-candle system feeding from the bottom position

4.2.3 Modifying mesh for better solution

Once a mesh has been built, it is possible to modify it to make the better CFD solution on the modified mesh. This modification will take place before a solution of the flow problem is solved. Some CFD preprocessing program, such as GAMBIT, can employ this task. This can reduce the computing effort required to produce a solution and increase the accuracy of the solution. The topology of the mesh stays the same but the mesh points are moved so that the density of points increases where required as shown in **Fig. 4.14**. By using this technique the accuracy of the solution can be increased, but there is a penalty in that extra computational effort is required.

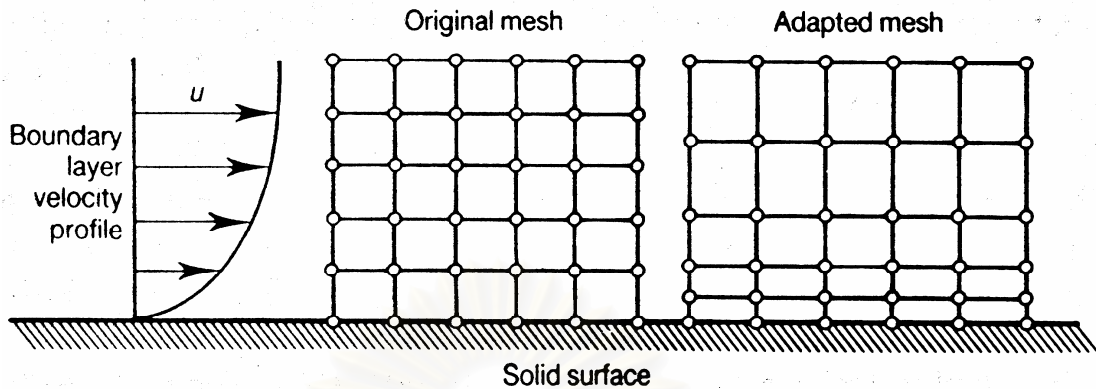


Fig. 4.14 Modifying mesh using for calculation

4.3 Defining model parameters

4.3.1 Fluid properties

The parameters required for inputting in the part of fluid are density, viscosity, specific heat capacity and thermal conductivity as shown in **Fig. 4.15**.

The screenshot shows the 'Materials' dialog box with the following settings:

Name	Material Type	Order Materials By
air	fluid	<input checked="" type="radio"/> Name <input type="radio"/> Chemical Formula
Chemical Formula	Fluid Materials	Database...
	air	
	Mixture	
	none	

Properties	
Density (kg/m ³)	constant Edit... 0.6455
Cp (J/kg-K)	constant Edit... 1039.2
Thermal Conductivity (W/m-K)	constant Edit... 0.0431
Viscosity (kg/m-s)	constant Edit... 2.858e-05

Buttons at the bottom: Change/Create, Delete, Close, Help

Fig. 4.15 The parameters required for fluid specification

4.3.2 Ceramic candle filter properties

The parameters required for inputting in the part of ceramic candle filter are density, specific heat capacity, thermal conductivity, porosity and viscous resistance as shown in **Fig. 4.16** and **4.17**.

The screenshot shows a 'Materials' dialog box with the following fields and values:

Field	Value
Name	filters
Material Type	solid
Order Materials By	<input checked="" type="radio"/> Name <input type="radio"/> Chemical Formula
Chemical Formula	filt
Solid Materials	filters (filt)
Mixture	none
Database...	[Button]
Density (kg/m ³)	constant 250
Cp (j/kg-k)	constant 1050
Thermal Conductivity (w/m-k)	constant 0.075

Buttons at the bottom: Change/Create, Delete, Close, Help

Fig. 4.16 The properties of ceramic candle filter

สถาบันทฤษฎีบริการ
จุฬาลงกรณ์มหาวิทยาลัย

Fluid

Zone Name
1_1_0

Material Name air Edit...

Source Terms
 Fixed Values
 Local Coordinate System For Fixed Velocities
 Laminar Zone
 Porous Zone
 Conical

Viscous Resistance

Direction-1 (1/m2)	3.614549e+11	constant
Direction-2 (1/m2)	3.614549e+11	constant
Direction-3 (1/m2)	3.614549e+11	constant

Fluid Porosity

Porosity 0.85 constant

Solid Material Name filters Edit...

Rotation-Axis Origin

X (mm)	0
Y (mm)	0
Z (mm)	0

Rotation-Axis Direction

X	0
Y	0
Z	1

Motion Type Stationary

OK Cancel Help

Fig. 4.17 The characteristic of ceramic candle filter

4.3.3 Boundary condition

The parameters required for inputting in the boundary condition are velocity specification method, reference frame, velocity magnitude, temperature, turbulence specification method, turbulence kinetic energy (k) and turbulence dissipation rate (ϵ) as shown in **Fig. 4.18**.

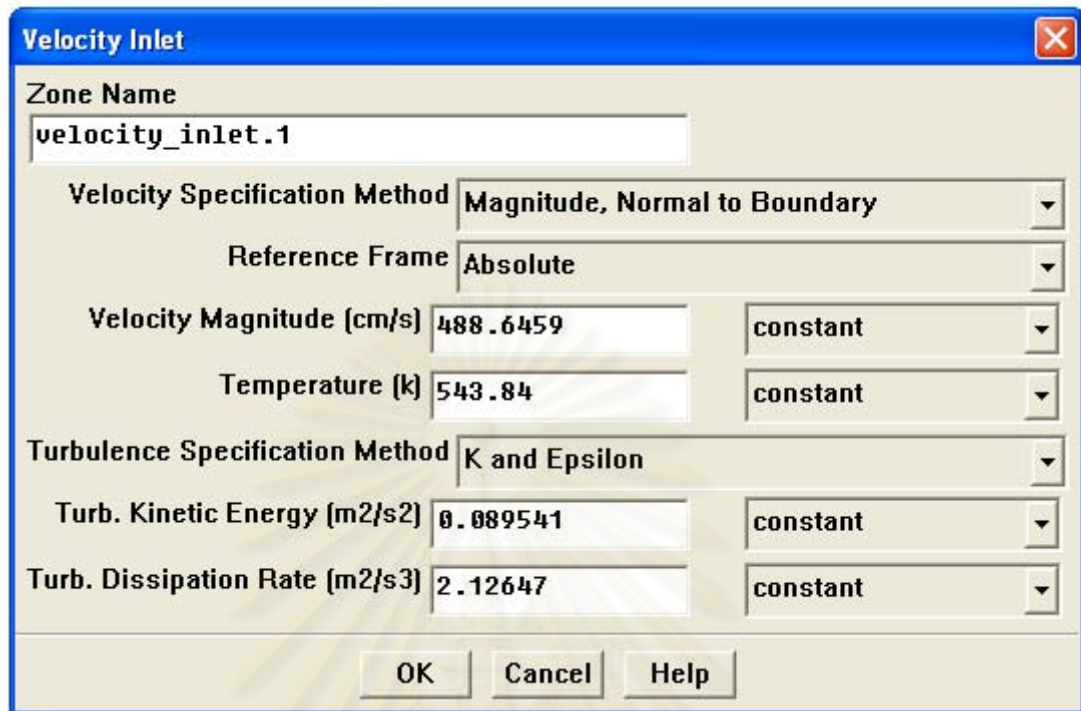


Fig. 4.18 The velocity inlet boundary condition

4.4 Model assumptions

4.4.1 Assumptions for ceramic candle filter

- 1 Both ceramic filter candles have uniform porosity with the same average pore diameter
2. All dust particles have spherical shapes and are monodisperse in size.
3. The spatial distribution of the captured particles is completely random on the candle surface.
4. The porous properties of the candle wall are isotropic.
5. The thermophysical properties of the fluid and the porous medium itself remain constant during filtration.

4.4.2 Assumptions for fluid flow behavior

1. Though the experimental filtration unit was operated by HPTRI in a constant flow mode, the local filtration face velocity was affected by the corresponding local cake thickness (the local total flow resistance).
2. No-slip wall condition is applicable.

3. The gas is incompressible.
4. The filtration face velocity is dependent on the thickness of the deposited dust cake and the total flow resistance.

4.5 Procedure of simulation

A 3-dimensional (3D) computational grid is used to calculate the gas flow in the twin-candle filtration unit. The geometry of the computational grid including the twin-candle and single-candle system with various inlet positions as shown in **Fig. 4.10, 4.11, 4.12 and 4.13**. An inlet gas velocity of interest is selected, and the RNG based $k-\varepsilon$ turbulence model of FLUENT is used in the computation. The turbulence model is derived from the instantaneous Navier-Stokes equation, using a mathematical technique called the “renormalization group” (RNG) method. Problem solving steps of GAMBIT and FLUENT softwares are as following.\

1. Create the 3D model geometry and computational grid with the aid of GAMBIT.
2. Initiate the appropriate FLUENT solver for 3D modeling.
3. Import the grid obtained in Step 1 into FLUENT.
4. Check the grid conditions.
5. Select the solver formulation.
6. Choose the suitable basic equations to be solved:
 - Laminar or turbulent, chemical species and accompanying reaction, heat transfer model, etc.
 - Select the additional model needed: in this case candle’s wall is porous media.
8. Specify the boundary conditions of the candle.
9. Adjust the FLUENT solution control parameters.
10. Initialize the flow field.
11. Numerically integrate the model equations to obtain a solution.
12. Examine the results.
13. Save the results.
14. If necessary, refine the computational grid or consider a change of the numerical or physical model.

4.5.1 Virgin filters with clean air

For virgin candle filters, it is assumed that the whole candle wall has uniform viscous resistance. Then, we find the correct viscous resistance of the virgin ceramic candles (wall) using the experimental pressure drop data (twin candle filters) obtained by HPTRI. We also construct a correlation between the viscous resistance and pressure drop with the flow rate being fixed. By the way, the flow resistance is defined here as the product between the viscous resistance and the thickness of the ceramic candle. The procedure of calculation of the resistance of the virgin filter is shown in **Fig. 4.19**.

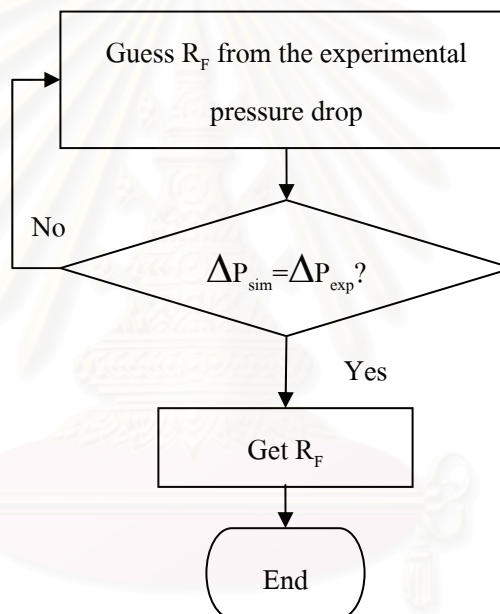


Fig. 4.19 The procedure of calculation of the flow resistance of the virgin ceramic candle filter

Based on the experimental pressure drop for the system, we carry out iterations to estimate the viscous resistance of the filter. After we get the correct viscous resistance (from FLUENT code), we use it to calculate the flow resistance of the filter.

4.5.2 Loaded filter (cyclic operation)

In our preliminary study, we assume uniform local cake deposition on the entire surface of each individual filter but allow for difference in cake deposition

between the two candle filters in order to find out how the flow field changes over time. This approach implies uniform changes in flow resistance during pulsed cleaning and cake deposition. Using the experimental pressure drop measured at 20-second intervals, we proceed to estimate the average rate of cake formation or average change in the flow resistance of each candle filter during each time interval. One interesting phenomenon not seen in the single candle filter systems is the unforeseen cleaning effect on an adjacent filter due to the pulsed cleaning of the other filter.

The purpose of the present study is to predict the cake formation behavior on the surface of each candle filter. For the filter system of interest, we separate the 2 candles to calculate the spatial distribution of dust loading. First, each ceramic candle was divided into 8 layers, which were further subdivided to 4 equal elements per layer as shown in **Figs. 4.20 and 4.21**. In order to investigate the non-uniformity of dust deposition on the surface of each candle due to the difference in the volumetric flow rate of air passing through each element of candle filter, this approach allows us to predict the dust cake formation by using the experimental ΔP obtained by HPTRI. For the case of non-uniform cake deposition, some of the simulation results will be presented as the distribution of velocity through each element.

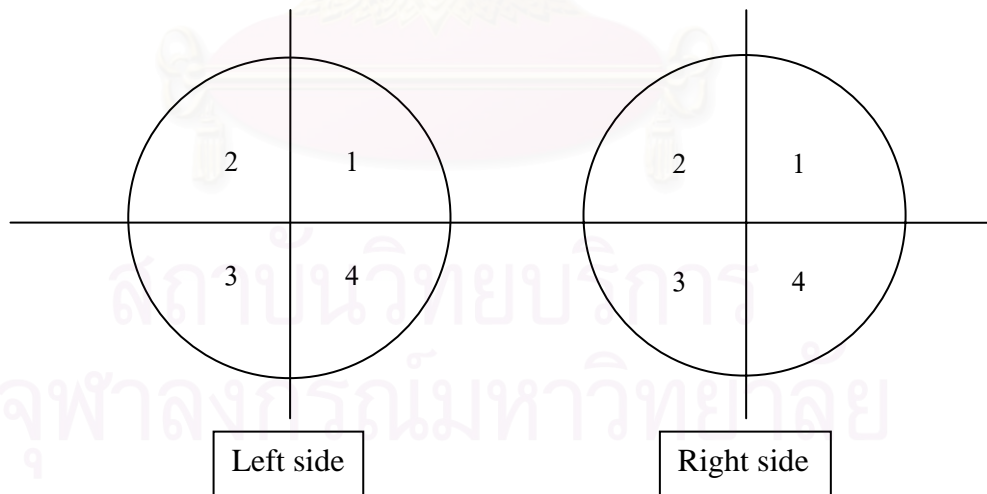


Fig. 4.20 The filter sub-divided into 4 quadrants for each of the 8 layers

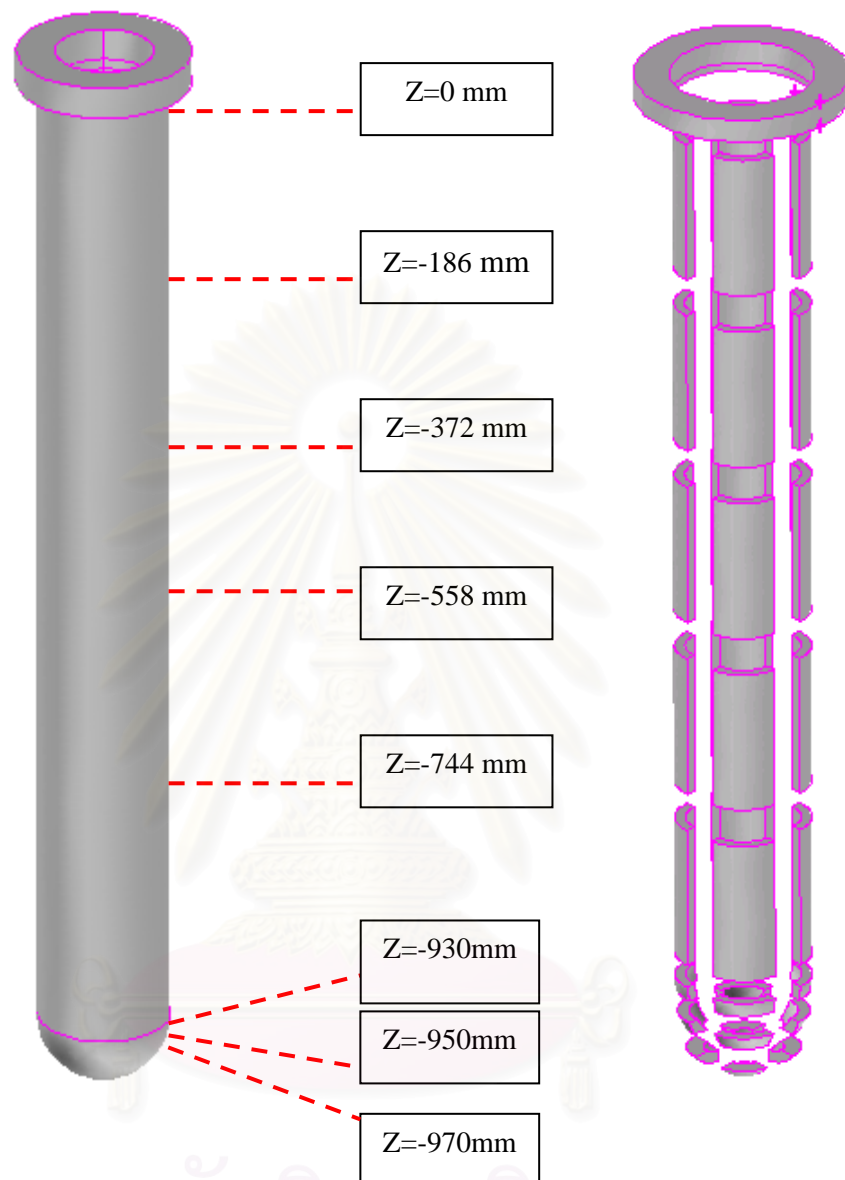


Fig. 4.21 The 8 layers of the candle filter used in calculation

The elements in each layer may assume different shapes as shown in **Fig. 4.22**. The surface area of each element is listed in **Table 4.2**.

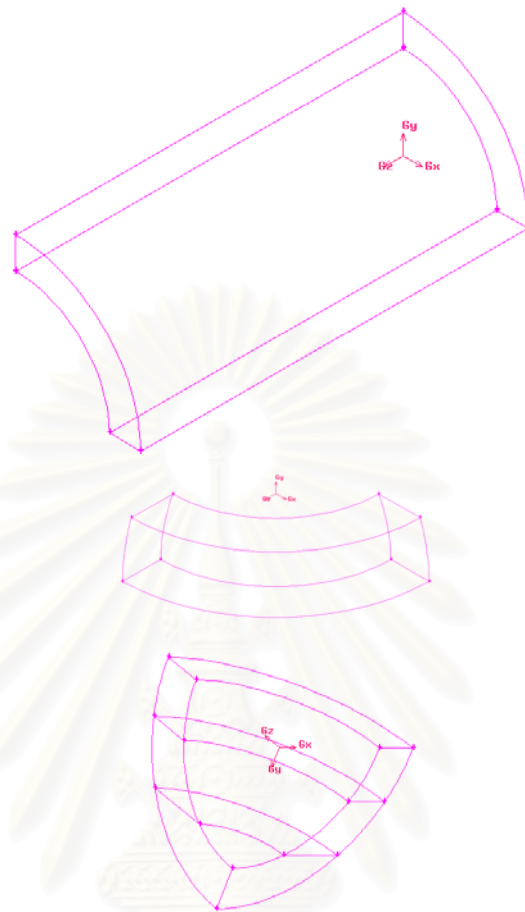
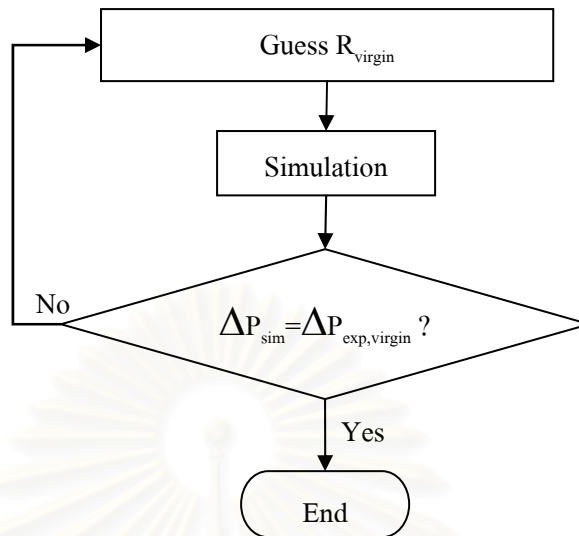


Fig. 4.22 The shape of each element used for the calculation

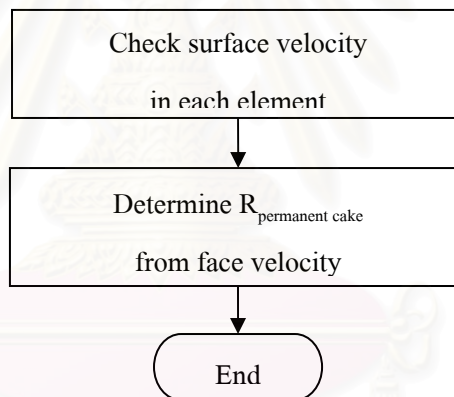
Table. 4.2 Surface area of each element

Z position (mm)	Average simulation area (cm ²)
0-930	175.15
930-950	18.77
950-970	18.8
970-990	18.67

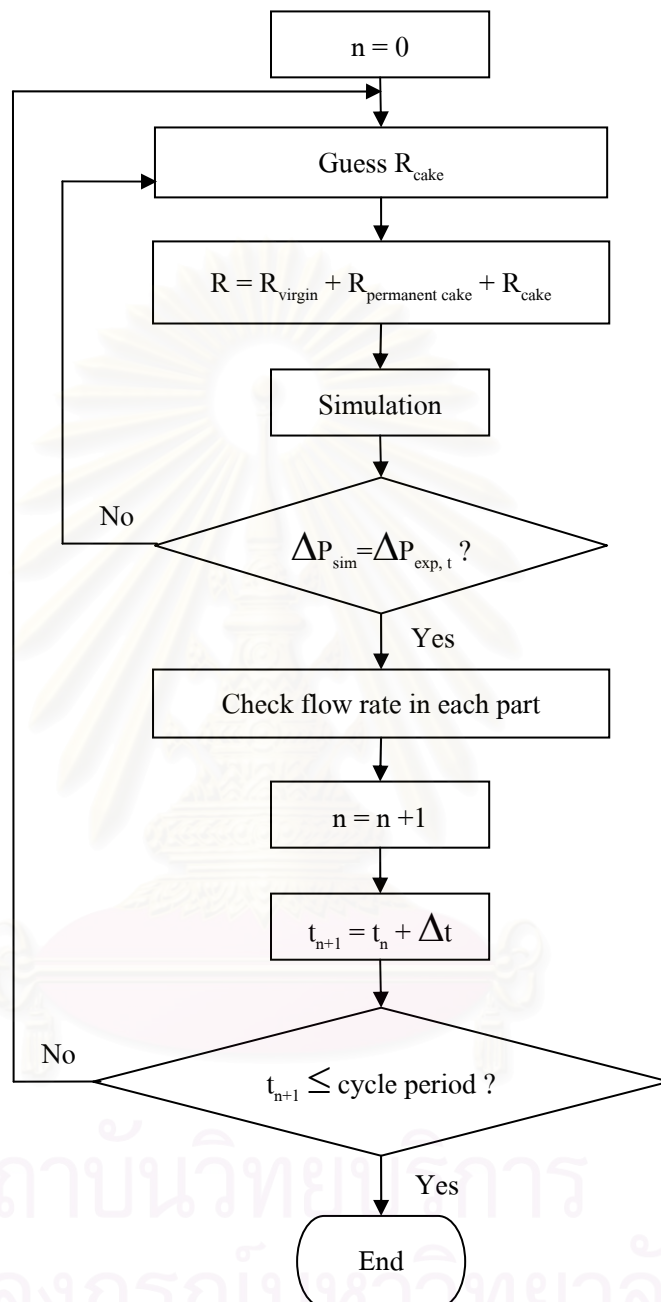
When we adopt the algorithm shown in **Fig. 4.23a, 4.23b and 4.23c**, we will get the estimate of the flow resistance of each filter element at each cyclic time.



(a) Estimate property (flow resistance) of candle wall of virgin filter



(b) Estimate property (flow resistance) of candle wall of used filter under cyclic operation, including permanent flow resistance due to embedded particles.



(c) Estimate changes in flow resistance, gas through-flow, cake thickness, etc. of each candle wall element during cyclic operation.

Fig. 4.23 The algorithm used for the calculation of the flow resistance of the filtration cake at each time interval

CHAPTER V

RESULTS AND DISCUSSION

It should be noted that, in all of the present experiments and corresponding simulations, the flow rate of the influent gas stream was always kept constant by automatically adjusting the inlet pressure (or the total pressure drop of the unit). In this research, we first used the experimental pressure drop data at room temperature condition ($0.38 \text{ m}^3/\text{min}$, 287 K , Fly ash JIS10 $5 \text{ g}/\text{m}^3$) to create the CFD model since it was simple and practical for doing the experiment. Next, the CFD model was used for predicting the pressure drop behavior of the filtration system at high temperature condition ($0.57 \text{ m}^3/\text{min}$, 574 K , $5 \text{ g}/\text{m}^3$ of Fly ash JIS10). The simulation results are classified into two main groups as follows: virgin candle filters with clean air, and cyclic operation with dust-laden air.

5.1 Validation of virgin filter with clean air

Since the filters were brand-new and only clean air was used, it was reasonable to assume that the gas flow rate through the candle filter on the left was always equal to that on the right in the case of the twin ceramic candles.

5.1.1 Viscous resistance of candle filter

First we characterized the porous wall property of the virgin filter candles by estimating the value of their viscous or flow resistance that would yield the same pressure drop as the experimental value in the case of clean air flow through the filter. For simplicity we assumed that the twin-filter candles had identical characteristics. It was subsequently found that the tested viscous resistance of the virgin candle wall should be $6.05 \times 10^{10} \text{ m}^{-2}$ when the total gas flow rate is $0.38 \text{ m}^3/\text{min}$.

5.1.1.1 Effect of influent gas flow rate

To understand the relationship between the viscous resistance of the candle filter and the calculated pressure drop, we next carried out additional simulations for the case of constant gas flow rate (0.38 and $0.57 \text{ m}^3/\text{min}$) at 287 K . Fig. 5.1 illustrates the effect of the influent gas flow rate at 287 K ($14 \text{ }^\circ\text{C}$). Logically the flow rate

significantly affected the pressure drop. The higher the gas flow rate, the higher the predicted pressure drop. For example, when the flow rate was increased by 50 %, the pressure drop was found to also increase by roughly 50 %.

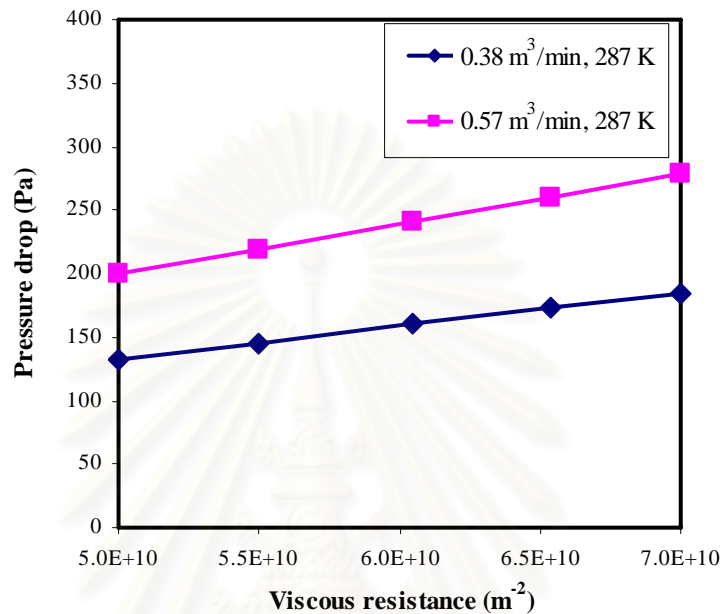


Figure 5.1 The effect of the flow rate on the relation between the viscous resistance of the candle wall and the pressure drop

5.1.1.2 Effect of elevated gas temperature

Similarly, we investigated the effect of elevated gas temperature at 430 K on the relationship between the viscous resistance and the calculated pressure drop. Fig. 5.2 also shows the effect of elevated gas temperature for the same influent flow rate of $0.38 \text{ m}^3/\text{min}$. It is obvious that, as the temperature of the system increased, the pressure drop followed suit because of the higher gas viscosity and face velocity. When the absolute temperature was increased by 50 %, the pressure drop was found to increase by 36 %.

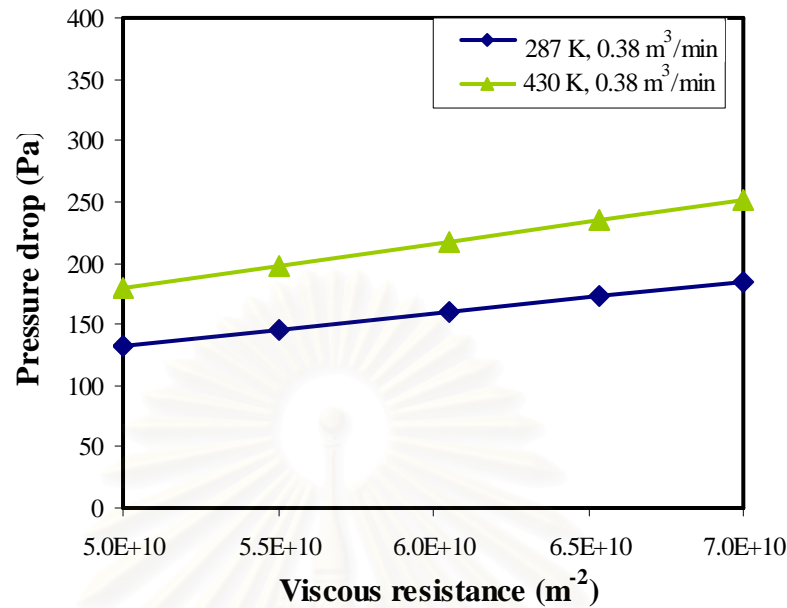


Figure 5.2 The effect of the temperature on the relation between the viscous resistance of the candle wall and the pressure drop

From the above results, it may be concluded that the gas flow rate has a more significant effect than the gas temperature. From the experiment, the pressure drop of clean air through the virgin filter was 160 Pascal at 287 K, $0.38 \text{ m}^3/\text{min}$. Next, the room-temperature CFD model was used to predict the initial pressure drop at high temperature conditions ($0.57 \text{ m}^3/\text{min}$, 574 K, $5 \text{ g}/\text{m}^3$ Fly ash JIS10). It was found that the predicted pressure drop from simulation was over-predicted by about 20 %. The correct viscous resistance of the filter at 574 K must be equal to $5.04 \times 10^{10} \text{ m}^{-2}$, which is less than the room-temperature value by about 17 % to keep the pressure drop equal to the experimental data.

5.1.2 Spatial distribution of local face velocity

Originally it was thought that the local face velocity (normal velocity) of the gas flowing through each part of the candle wall should be essentially identical if the filter candles are identical and clean, and only clean air is used. Our CFD simulation results, however, indicated that significant deviation in the local face velocity could and did happen in the case of our twin candle filter unit.

In order to obtain the spatial distribution of steady gas flow through each small portion of the twin candle filters, and in the case of cyclic operation using dust

laden air, the flow deviation with cycle time between the twin filter candles, we divided the wall of each filter candle into 32 small pieces or elements and obtained the “local” normal flow rate and “local” normal mass or volume flux through each element by CFD simulation.

Subsequently, we interpreted the successive simulation results against cyclic time in different terms such as the local flow resistance, the local velocity distribution, and the corresponding local cake thickness.

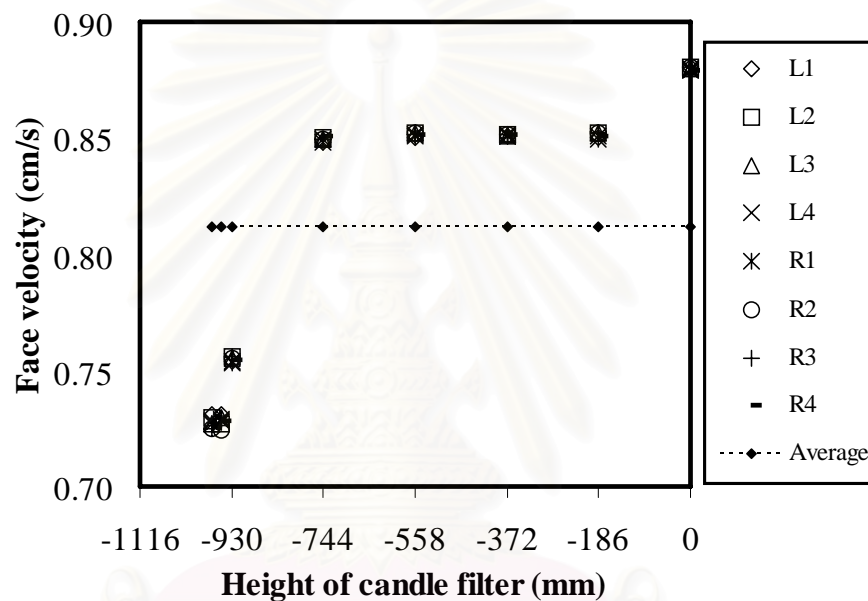


Figure 5.3 Calculated deviations of local normal face velocity at each height and each quadrant of the twin virgin candles

Fig. 5.3 shows the deviations of the calculated face velocity of clean air through the virgin candle filters in the case of clean steady gas flow. It was found that the local face velocity through each quadrant of the virgin filter was essentially the same as long as the quadrants are at the same candle height. At the top section of either candle, the normal face velocity was always highest and it decreased along the lowered height. Since the upward gas velocity outside the twin candles was much lower than its velocity inside the candles, the pressure drop in the former case was lower than the latter when the gas had to travel the same distance on either side. In reality, the pressure drops must be the same, so the local face velocity became significantly different. Unexpectedly, the normal face velocity through the spherical cap ($z=-930$, -950 and -970 mm) decreased remarkably supposedly because of the

enlarged curvaceous surface area. As summarized in Table 5.1, the values of the local normal face velocity may be classified into 4 zones. The maximum velocity was 7.3 % above the average velocity. On the other hand, the minimum velocity was 9.8 % below the average value.

Table 5.1 Zones of normal face velocity distribution along z-position of the candle

Zone	Upper height (mm)	Average velocity (cm/s)	Remark
1	0	0.88	Top end
2	-186, -372, -558, -744	0.85	Cylindrical portion
3	-930	0.76	Base of spherical cap
4	-950, -970	0.74	Curved portion of spherical cap

Fig. 5.4 shows the velocity distributions of the single-candle and twin-candle systems for the cases when the total gas flow was equal. In the figure, the normal face velocity on the filter surface of the single-candle system was double that of the twin-candle system as the influent gas flow was kept constant. The significantly different trends around the caps of the candles may be attributed to the fact that not only the face velocities are different but also the relative location of the inlet pipe with respect to the candles was different. The pipe was pointed at the bottom of the single candle but midway between the twin candles.

สถาบันวิทยบริการ
จุฬาลงกรณ์มหาวิทยาลัย

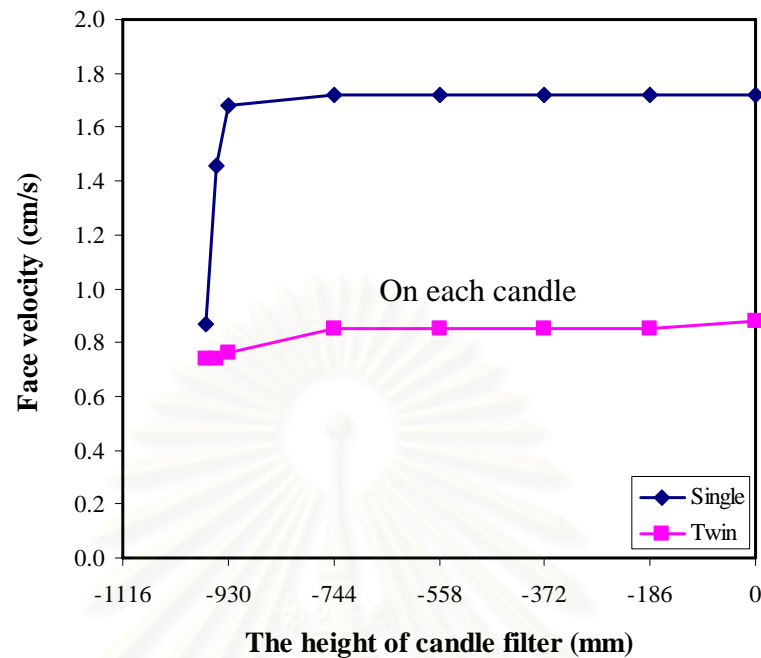


Figure 5.4 Calculated deviations of local normal face velocity at each height and each quadrant of the single and twin virgin candles

5.2 Validation of model for cyclic operation (dust-laden air, pulsed cleaning)

As the system was operated under a cyclic operation, it was suitable to make a preliminary investigation of the flow characteristics by the use of the uniform cake assumptions.

5.2.1 Viscous resistance and cake thickness formed uniformly on the surface of each candle filter

When we compared the pressure drops from the experiment ($0.38 \text{ m}^3/\text{min}$, 287 K , Fly ash $\text{JIS10 } 5 \text{ g/m}^3$) and the simulation, we found the relative error from the simulation was less than 0.1 percent as shown in Fig. 5.5. The solid and dashed arrows indicate the instant at which the right and left candles are pulsed with compressed air, respectively.

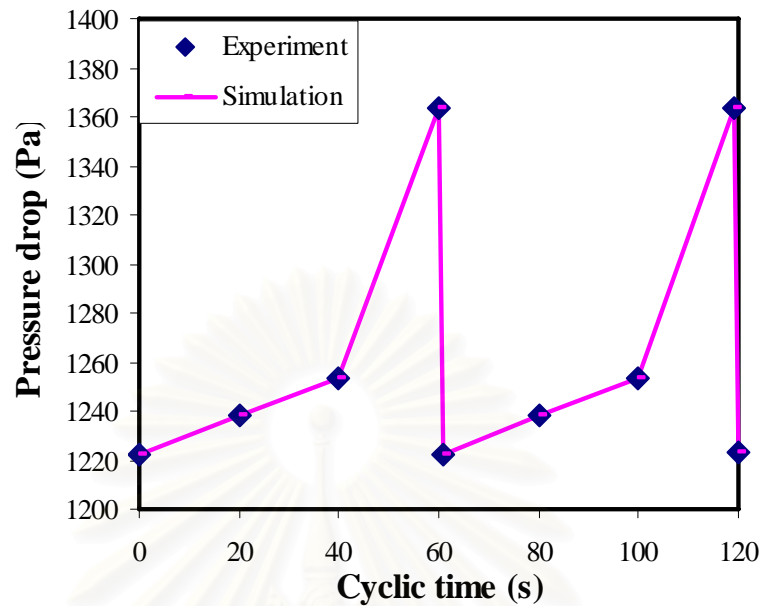


Figure 5.5 Comparison of the calculated and experimental pressure drops

From the pressure drops in Fig. 5.5, the corresponding viscous resistances could be estimated for each filter candle and the combined total as shown in Fig. 5.6. As expected, the trend of the total viscous resistance was similar to the pressure drop.

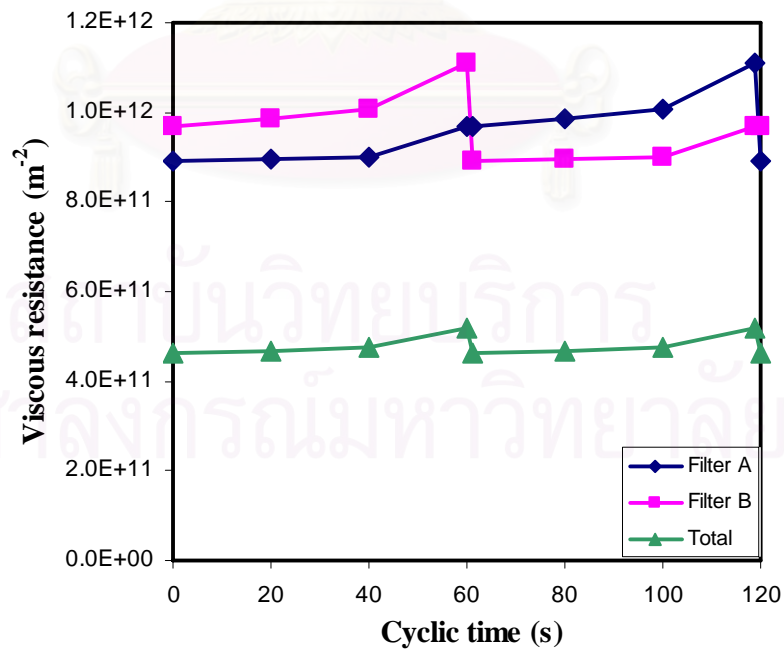


Figure 5.6 The estimated viscous resistances of individual candle filters and the combined total at each cyclic time step

5.2.1.1 Face velocity distribution

The plot of the normal face velocity (averaged over an entire candle) at each time step was shown in Fig. 5.7. The slope of the individual candle curves would be reversed when the pulse-jet system was actuated. Just after filter B was cleaned, the observed big drop in face velocity on filter A may be attributed to the fact that a smaller fraction of the constant influent flow would now go through filter A, once filter B became clean. This phenomenon would not be found if there was no interactive effect between both filters. A similar side-effect phenomenon was observed on filter B just after filter A was pulse-cleaned.

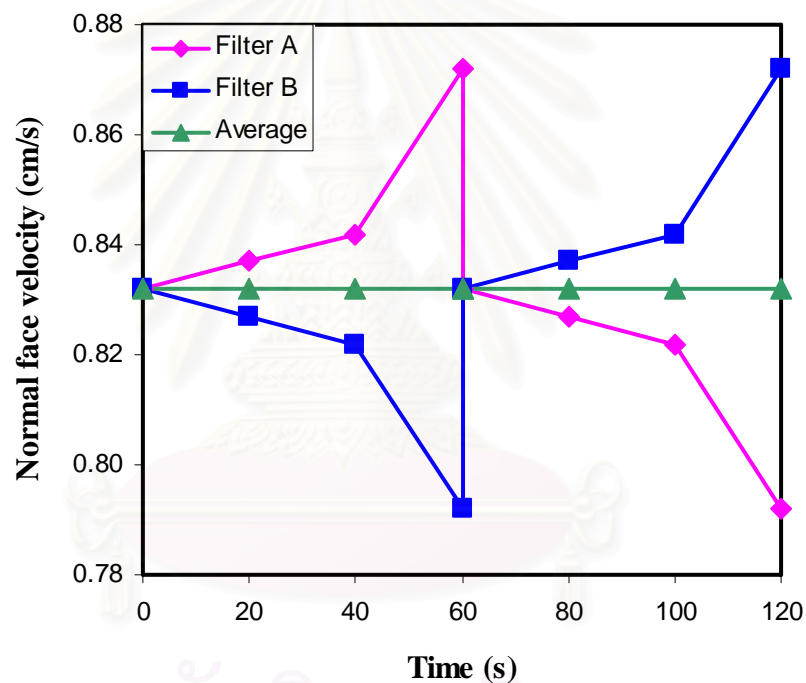


Figure 5.7 The calculated normal face velocity at each cyclic time

From the experimental data, the combined average face velocity for both candles was 0.833 cm/s. Meanwhile the combined average velocity from the simulation was found to be 0.832 cm/s. Therefore, it may be concluded that the present CFD model was suitable for the analysis and prediction of high-temperature gas flow inside a twin-candle filtration unit during cyclic operation.

5.2.1.2 Relative change in cake thickness

As an illustration, we see from the slope of the curve in Fig. 5.8 that the rate of increment of cake thickness on filter A and filter B was essentially equal if we

assumed uniform cake deposition on the whole surface of each candle. Since filter A was relatively cleaner than filter B at the beginning of a cycle, Figs 5.6 and 5.7 indicated that slightly more dirty gas flow should be channeled through filter A than filter B. So it should subsequently cause more rapid formation of dust cake on filter A. As a result, the flow resistance of and cake thickness on filter A should have increased more rapidly than filter B. However, this phenomenon was not observed in Figs. 5.6-5.8. This means that the assumption of uniform cake deposition on the whole surface of each candle was not realistic. In fact it would be shown that the local normal face velocity on each candle was not equal or uniformly distributed.

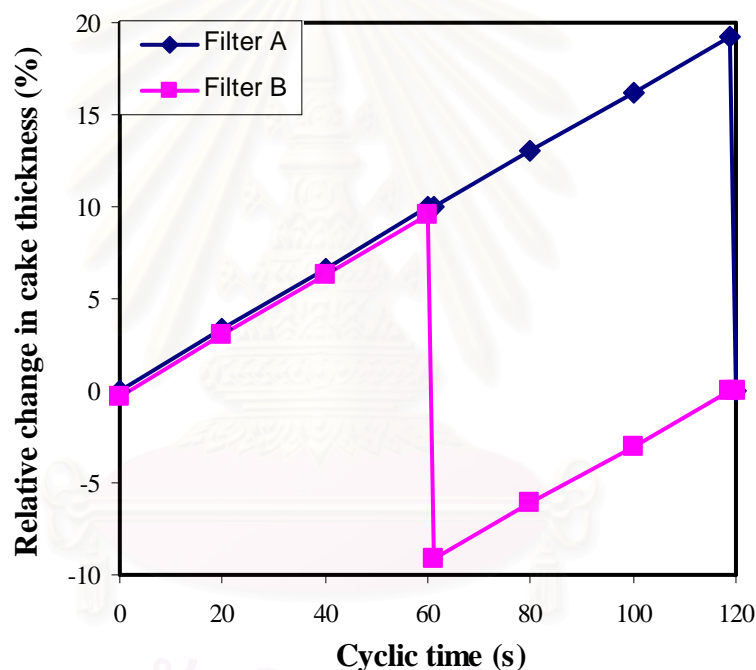


Figure 5.8 Relative change in cake thickness occurring at each cyclic time

5.2.2 Non-uniform cake formation on each candle filter

To prove the effect of non-uniform gas flow through each part of a candle filter, we divided the candle wall into 32 small pieces of elements. Using a short time interval of, say, 5 seconds, we calculated “local” cake build-up and gas flow rate through each wall element. It was assumed that the cake thickness and flow resistance remained essentially constant during this short time interval. The objective was to investigate the local filtration phenomenon as a function of time.

Fig. 5.9 shows the trend of the calculated pressure drops in the system which agreed very well with the experimental data. In fact the resulting pressure drop difference between the experimental and calculated ones was found to be less than 0.1 %.

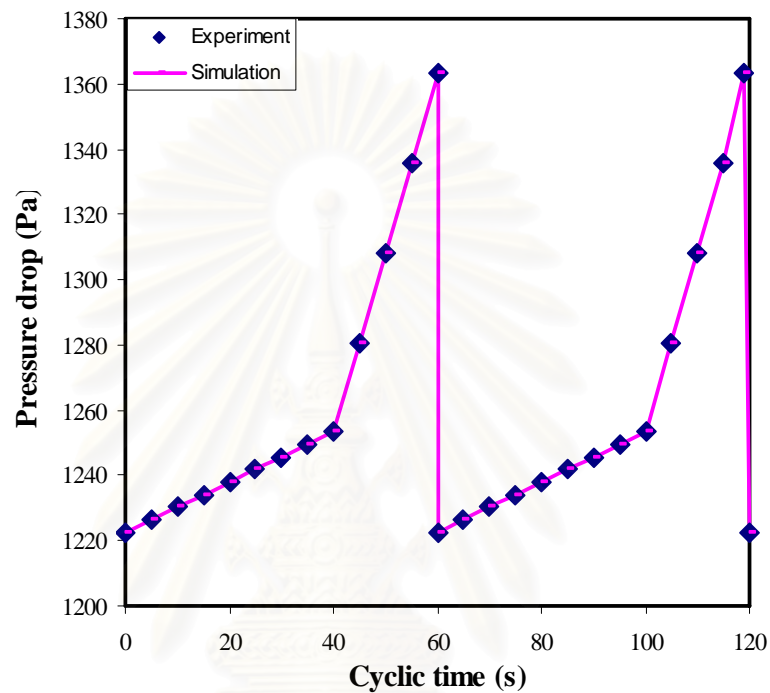


Figure 5.9 The calculated pressure drop compared with the experimental value at each cyclic time

Along with the calculated pressure drop in Fig. 5.9, the corresponding viscous resistance of each element on filter A and filter B was estimated as shown in Fig. 5.10 and Fig. 5.11. The local face velocity distribution on filter A and filter B is shown in Fig. 5.13. The time dependency of the local viscous resistance was the reverse of that of the local face velocity. Since fine dust particles were expected to disperse uniformly in the influent gas stream, a high face velocity through a wall element tended to lead to a proportionally greater amount of local dust deposition and the resulting local viscous resistance would proportionally be higher.

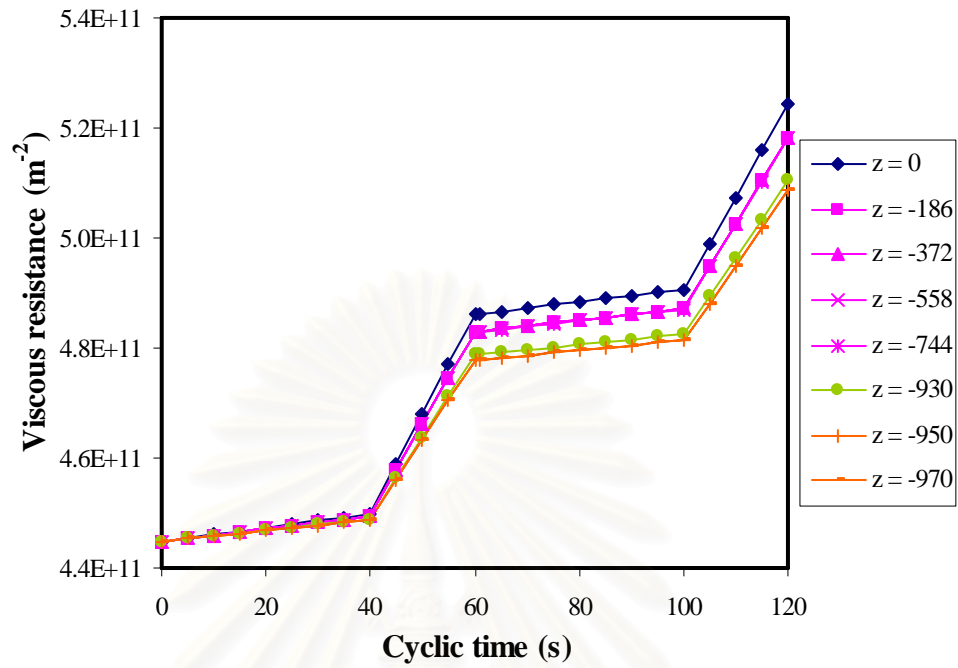


Fig. 5.10 The local viscous resistance of the candle filter A at each height as a function of cyclic time

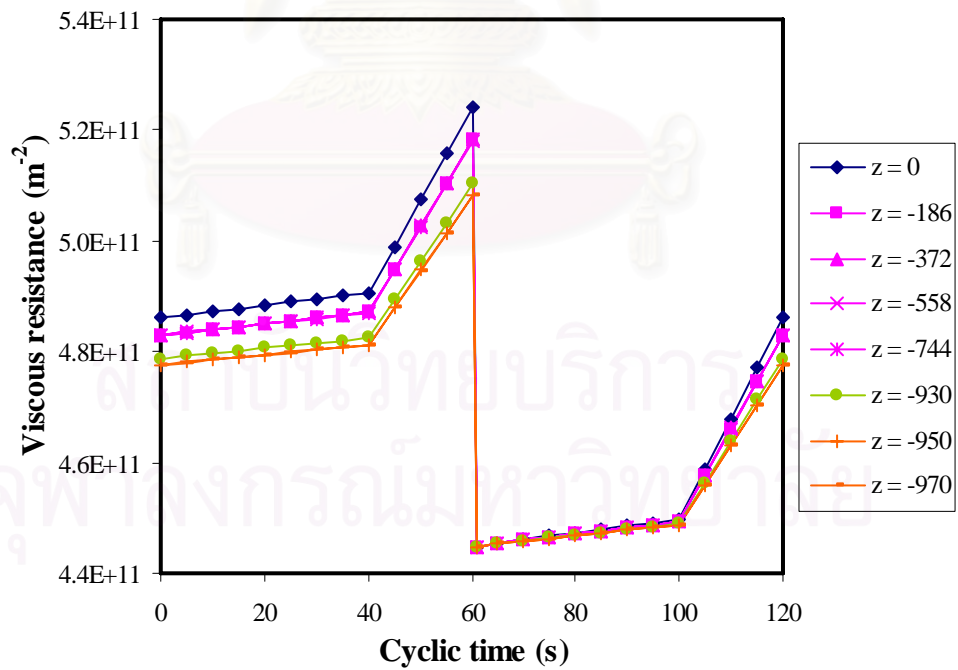


Fig. 5.11 The local viscous resistance of the candle filter B at each height as a function of cyclic time

By the way, we used the room-temperature CFD model to predict the behavior of the system at high temperature conditions ($0.57 \text{ m}^3/\text{min}$, 573 K , $5\text{g}/\text{m}^3$ of Fly ash JIS10) and found that the relative error is over about $+20 \%$ as shown in Fig 5.12. Next, we used another set of experimental data at a different high temperature (270 K) to create a new CFD model and re-estimated. We found that the relative error was decreased to 2% . Thus, we can conclude that a big difference in the temperature did cause a significant error in the CFD predictions.

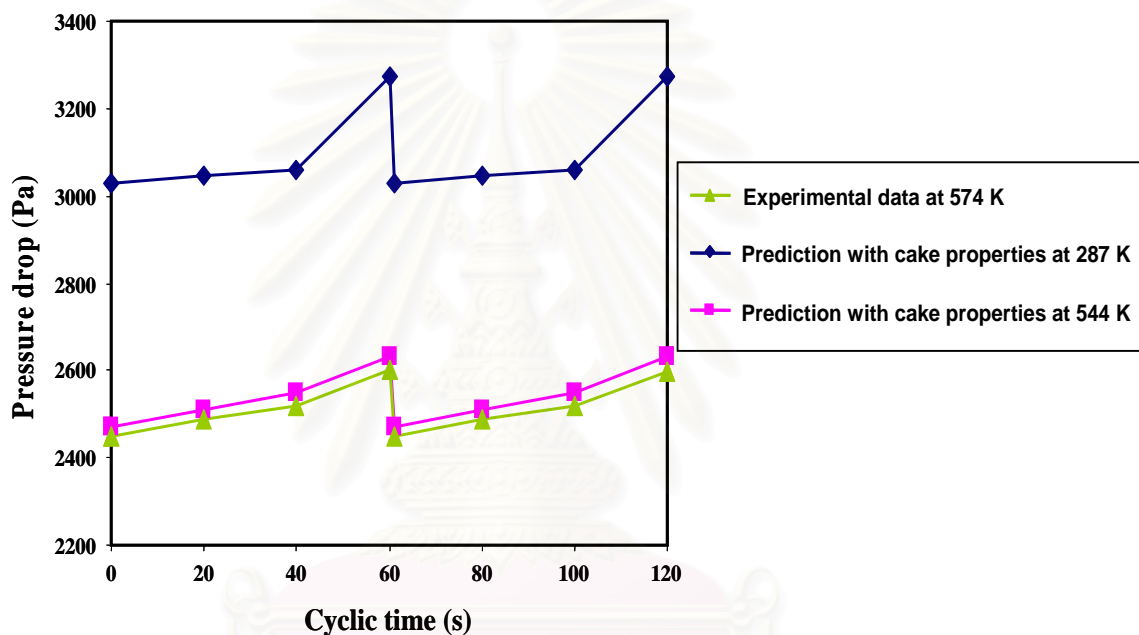


Fig. 5.12 The experimental pressure drop compared with the simulation results

5.2.2.1 Face velocity distribution

Fig. 5.13 shows the local face velocity distribution through each quadrant at the top end of the candle filters as a function of cyclic time.

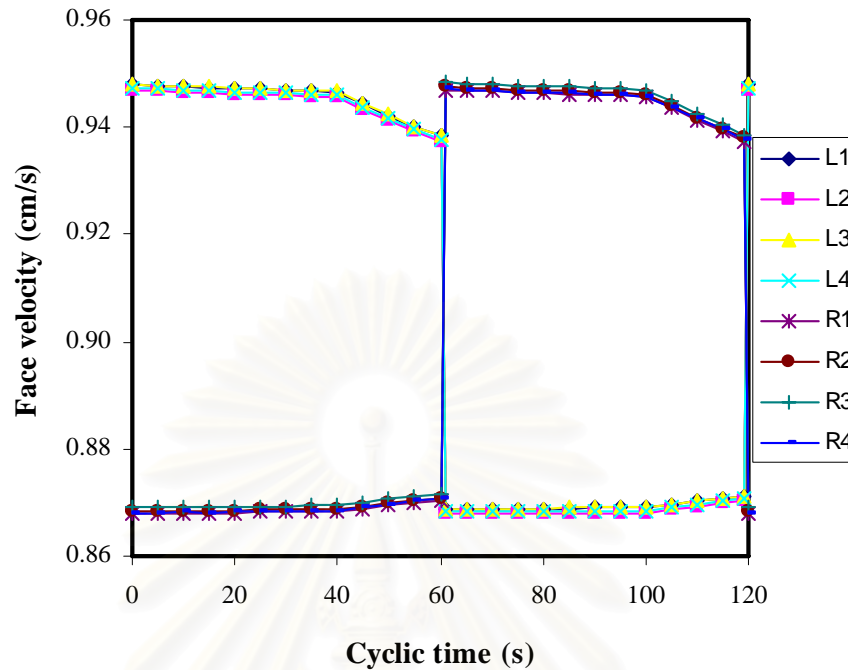


Fig. 5.13 Distribution of local fluid velocity normal to the candle's surface at the top end position as a function of cyclic time

According to figure 5.13, we can conclude that the local face velocity distribution was insignificantly affected by the position of the quadrant of the candle filter. In brief, the trend of the local velocity through the left candle was the reverse of that through the right candle. In other words, when the candle filter on the right was cleaned by compressed air, the local velocity through the left candle would be decreased immediately because the left candle also became comparatively dirtier, thereby causing more gas to flow through the cleaner right candle. After that, the local velocity through the left filter would increase slowly because the rate of cake deposition on the right candle was faster than that on the left. As a result, the local face velocity through the cleaned right candle filter would increase remarkably before it gradually decreased after that.

Obviously, as the resulting face velocity through the left candle increased gradually after it is cleaned, the corresponding local face velocity through the right was decreased by the same amount. This phenomenon occurred to balance the volumetric flow rate between the left and right candles because the unit is operated under constant influent flow rate.

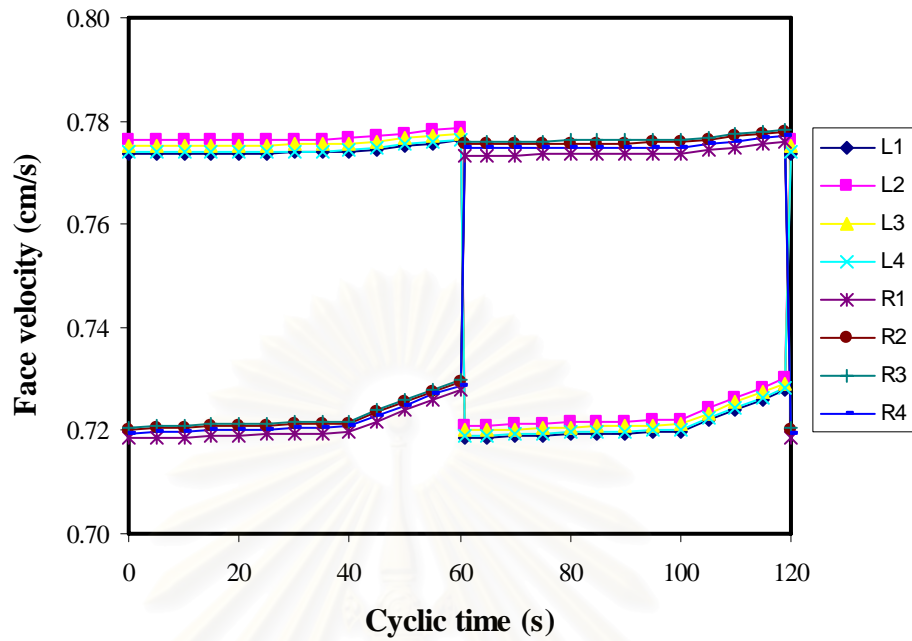


Fig. 5.14 Distribution of local fluid velocity normal to the candle's surface at $z = -930\text{mm}$ as a function of cyclic time

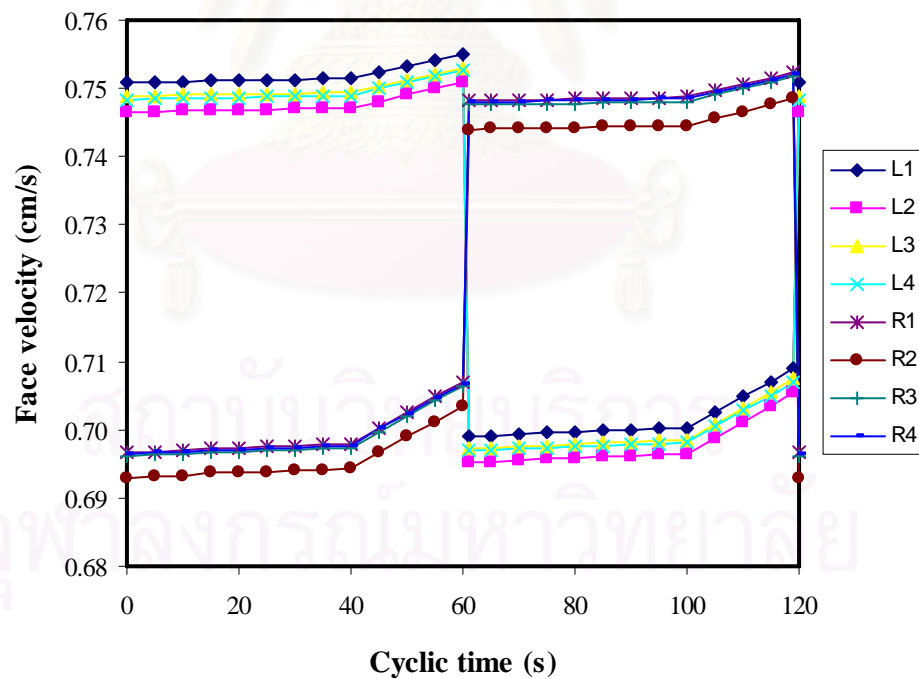


Fig. 5.15 Distribution of local fluid velocity normal to the candle's surface at $z = -950\text{mm}$ as a function of cyclic time

Figs. 5.14 – 5.16 show the trend of the local face velocity as a function of cyclic time. The local face velocity through the right candle increased gradually until

the filter on the left is cleaned; at that instant the face velocity through the right candle decreased abruptly because a higher flow rate tended to go through the cleaner filter.

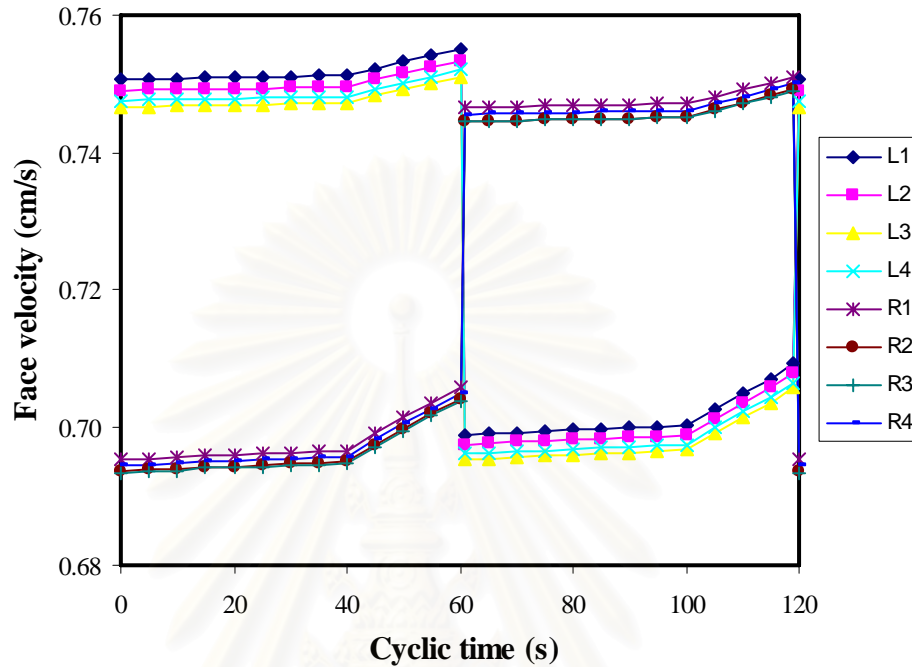


Fig. 5.16 Distribution of local fluid velocity normal to the candle's surface at $z=-970$ mm as a function of cyclic time

Fig. 5.17 and Fig. 5.18 show the average local face velocity at each height as a function of cyclic time on the left and right candles. It can clearly be seen that the local face velocities can be classified into 4 groups or zones along the candle height.

สถาบันวิทยบริการ
จุฬาลงกรณ์มหาวิทยาลัย

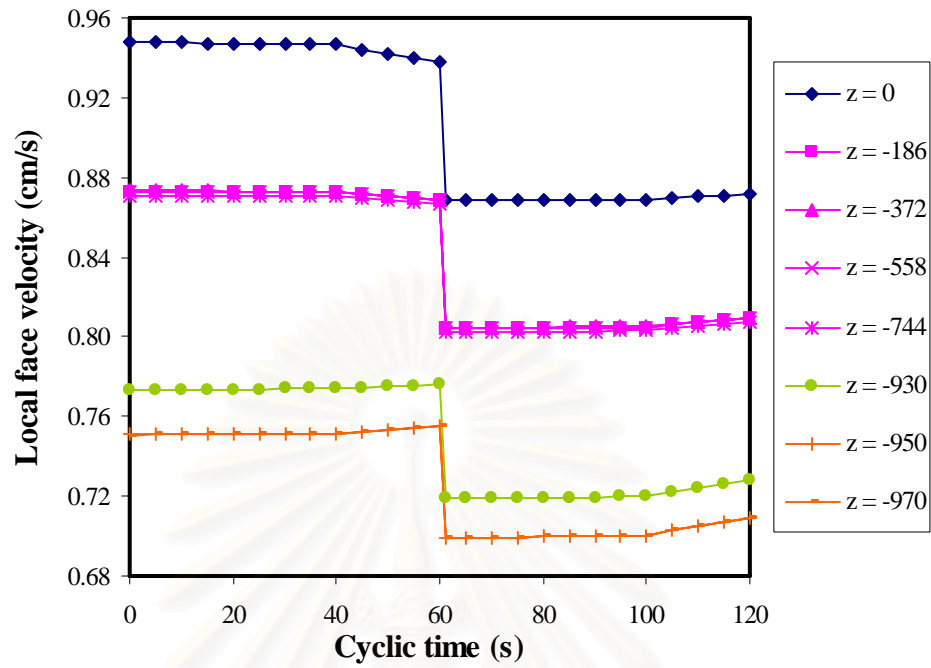


Fig. 5.17 Local fluid velocity through the first quadrant of the left candle at various heights (z) as a function of cyclic time

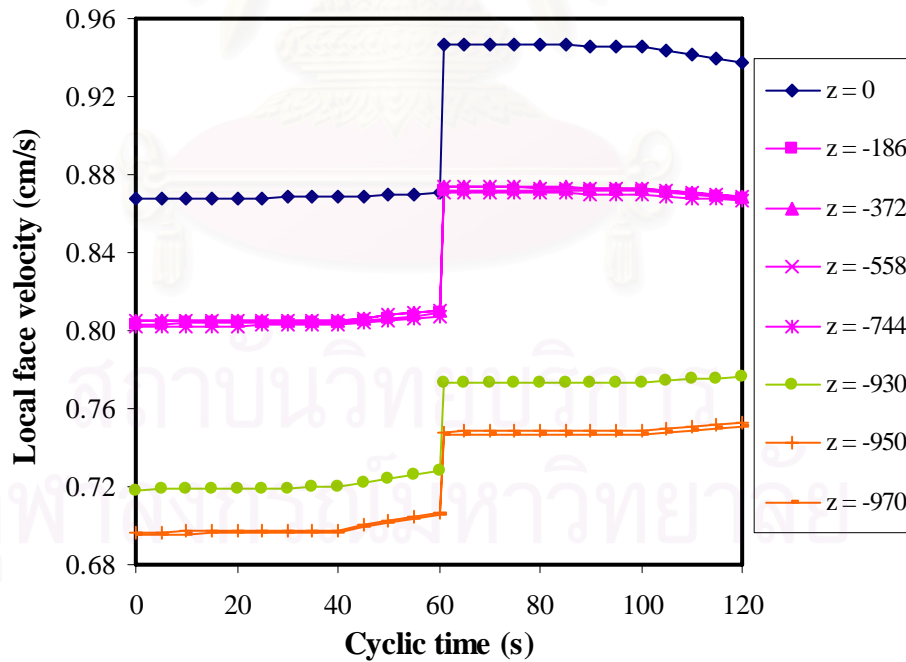


Fig. 5.18 Local fluid velocity through the first quadrant of the right candle at various heights (z) as a function of cyclic time

To aid the understanding, the effect of the candle height on the local face velocity at cyclic time zero is summarized in Fig. 5.19 which shows the average local face velocity distribution as a function of the candle height. In Zone 2, there was not much difference in face velocity among the 4 layers. In Zone 3 and Zone 4, the face velocity obviously dropped further from Zone 2.

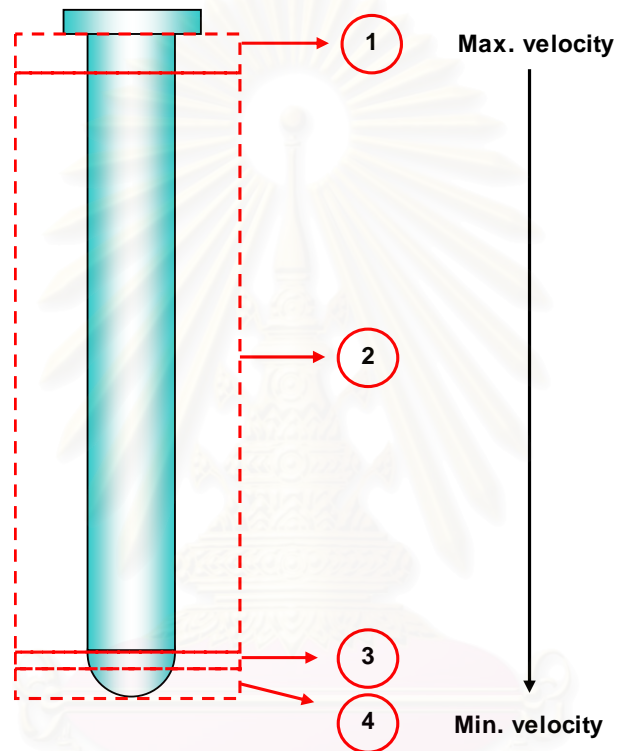


Fig. 5.19 Schematic of the local face velocity distribution along z-position at time = 0

สถาบันวิทยบริการ
จุฬาลงกรณ์มหาวิทยาลัย

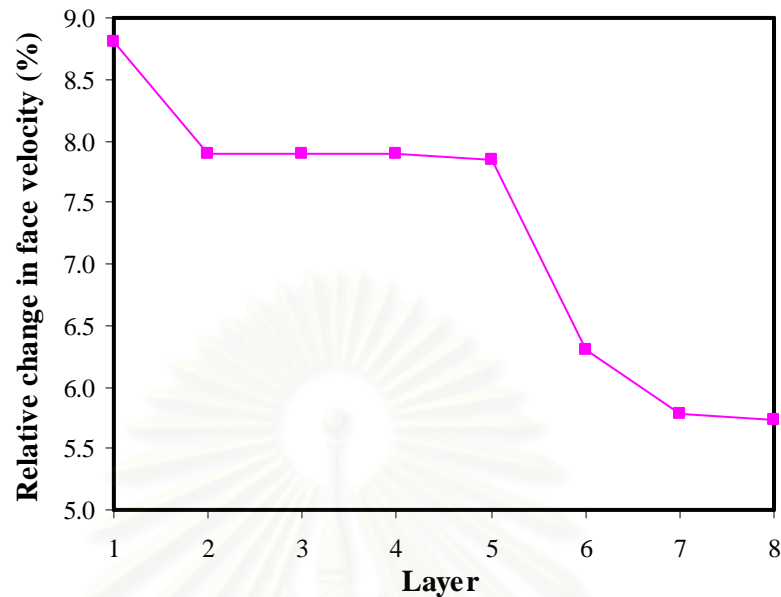


Fig. 5.20 Relative change in the velocity of the right candle before and after the right candle filter is pulsed as a function of height

Fig. 5.20 shows the relative change in the local face velocity along z-direction. In Fig. 5.20, layer no. 6 represents the edge between the lower end of the cylindrical portion of the candle and the hemi-spherical cap. Layers no. 7 and 8 belong to the hemi-spherical cap. Obviously, the pulsed air into the right candle cleaned the cylindrical wall region better than the cap region. In addition, the pulsed air didn't affect the left candle as shown in Fig. 5.21. It should be pointed out that this interesting observation has not been obtained via simulation before.

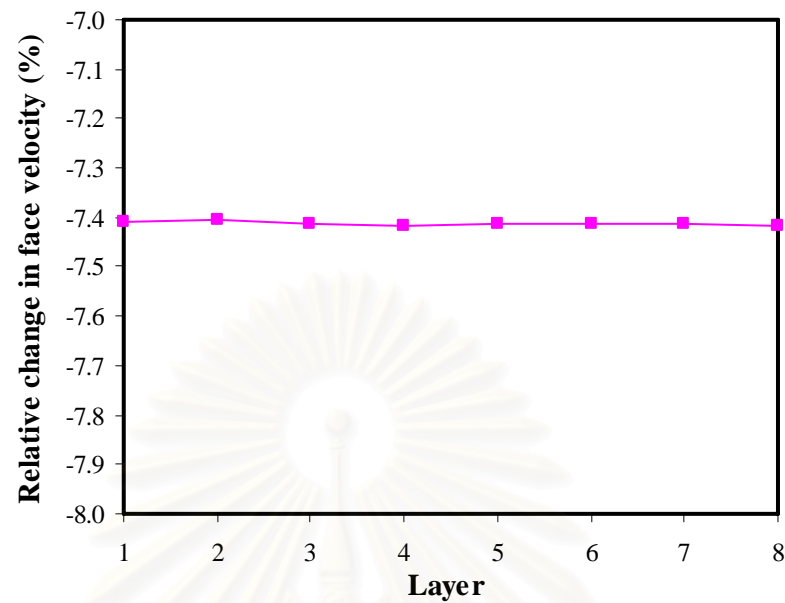


Fig. 5.21 Relative change in the velocity of the left candle before and after the right candle filter is pulsed as a function of height

5.2.2.2 Specific cake resistance

As shown in Fig. 5.22 and Fig. 5.23, we found that at time = 0 (after the left candle was pulsed), the temporary specific cake resistance of the left candle gradually increased while that of the right candle decreased. This phenomenon is caused by the changing fraction of air flow between the two candles after one candle was pulsed, so it caused change in dust cake permeability.

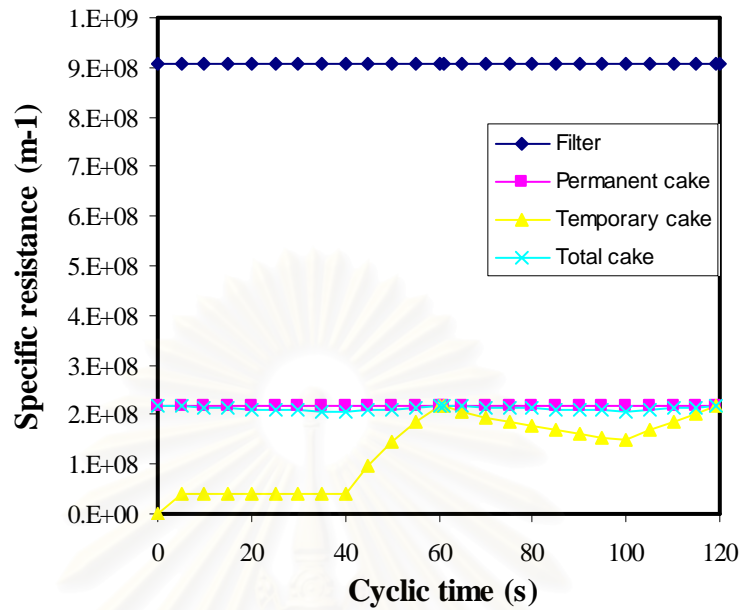


Fig. 5.22 The specific resistance of the left candle as the function of time

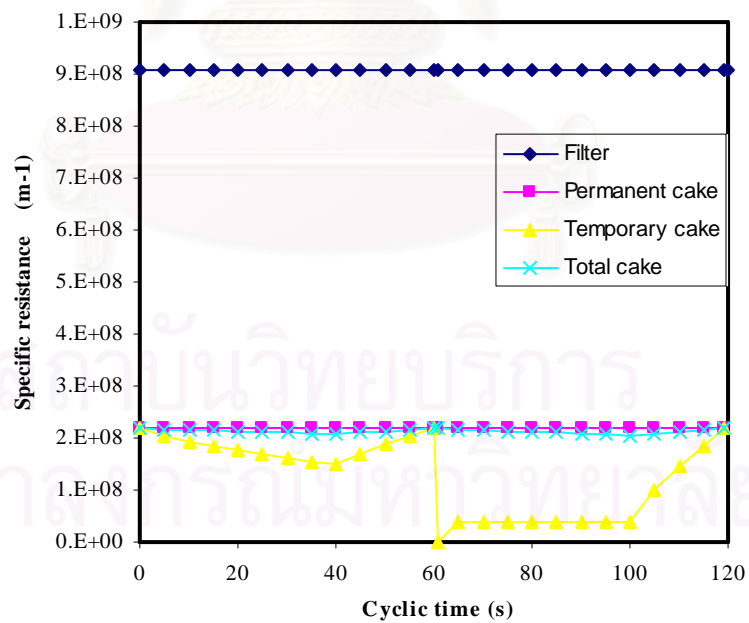


Fig. 5.23 The specific resistance of the right candle as the function of time

5.2.2.3 Relative change in cake thickness

Generally, gas flow through the newly formed cake over the surface of a candle generates an aerodynamic drag force that increases the compression on the thin

layers close to the candle surface, thereby slightly reducing their thickness and permeability. For simplicity, however, we hereby assume that all dust cake layers are incompressible and have uniform cake property. The rise of the pressure drop as a function of the cyclic time was determined, assuming that the local fluid face velocity remains essentially constant during a short time interval. In addition, we assumed that the fine dust particles are uniformly dispersed in the influent gas stream. Furthermore, due to the penetration of the fine dust particles, there are some particles embedded on the filter surface that cannot be removed by the pulse-jet system. We call this layer as “permanent cake”. Particles in the influent gas would be distributed along the local gas flow through the filter surface to form different dust cake thicknesses. So we can directly estimate the local rate of cake formation by considering the local face velocity obtained by simulation. To highlight the small changes in the cake thickness, the time dependency is shown in terms of the relative change in thickness compared to the permanent thickness.

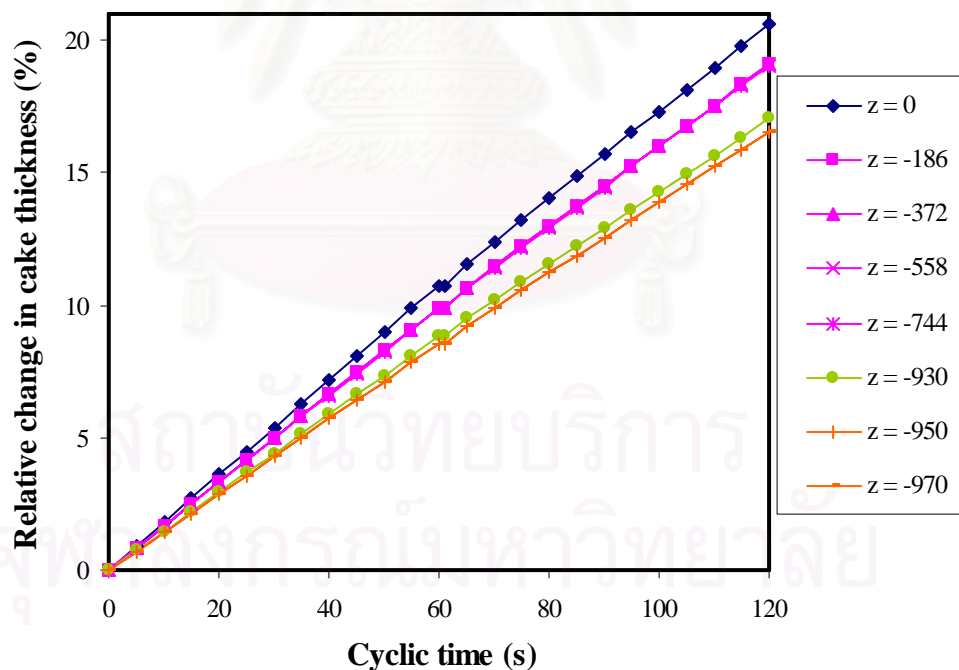


Fig. 5.24 Relative change in accumulated cake thickness on quadrant 2 of the left candle

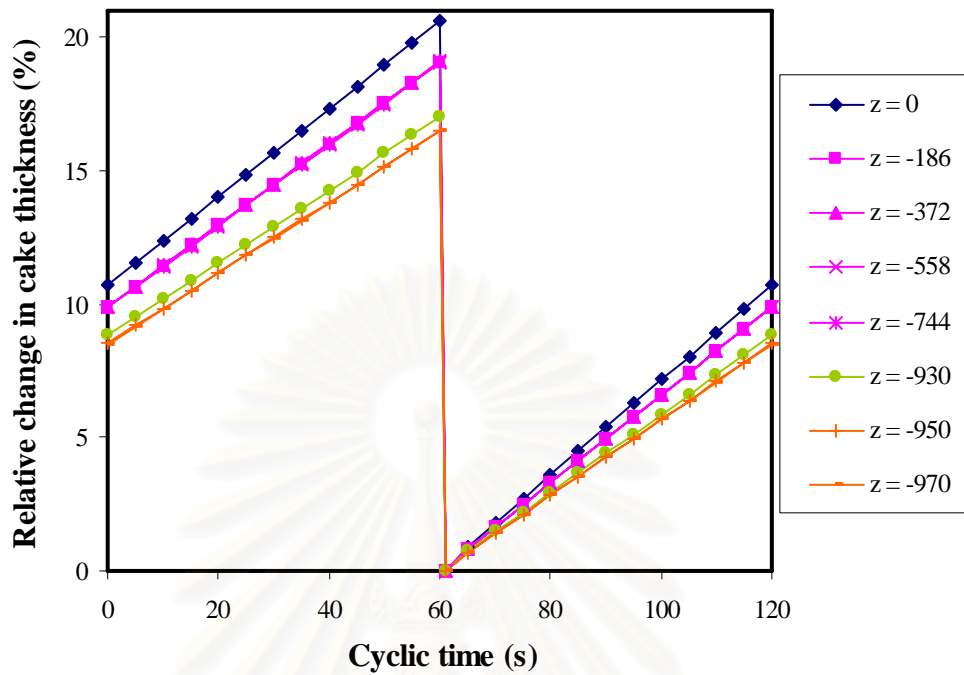


Fig. 5.25 Relative change in accumulated cake thickness on quadrant 1 of the right candle

Dust particles came in with the influent gas stream so the main factor which determined the rate of cake formation was the local face velocity. We can see in Fig. 5.24 and Fig. 5.25 that the relative changes in cake thickness can be divided into 4 zones as in the case of the local face velocity distribution. So the maximum cake thickness was built up at the top end of the candle filter and decreases as a function of the height until it reached a minimum cake thickness at the end of the hemi-spherical cap.

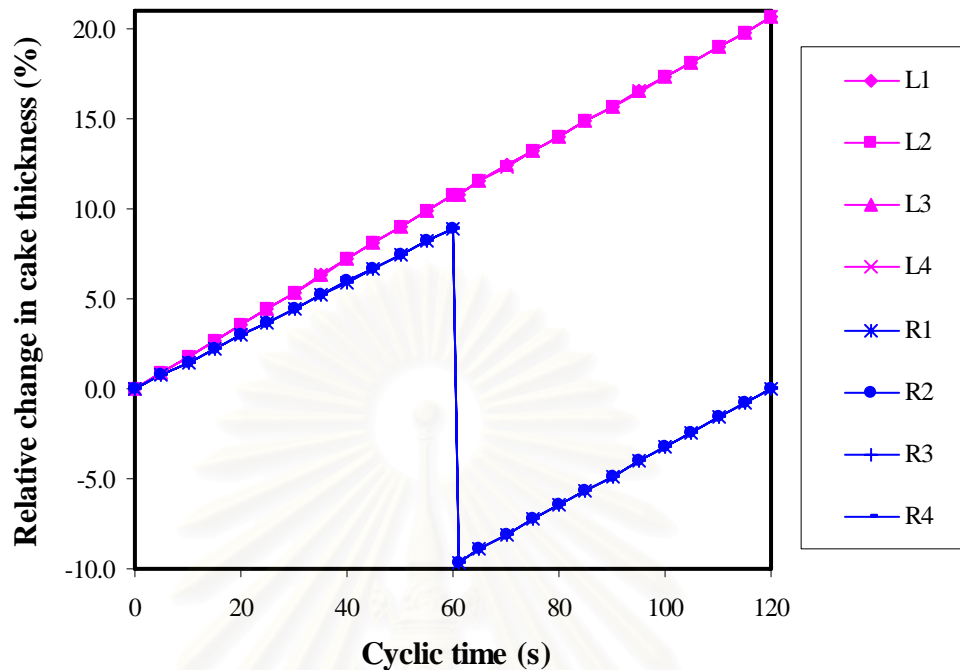


Fig. 5.26 Relative changes in accumulated cake thickness at the top ends of the candle filters

As we can see in Fig. 5.26, the position of each quadrant at the same height of the same candle filter does not significantly affect the cake thickness.

5.3 Effect of elevated gas temperature

In this section, we used the new CFD model created from the experimental data at one high temperature ($0.38 \text{ m}^3/\text{min}$, 544 K , $5 \text{ g}/\text{m}^3$ of Fly ash JIS10) to estimate the behavior of the system at other high temperature conditions. The higher the temperature, the higher the predicted pressure drop became. For example, when the temperature was increased by 50 %, the pressure drop was found to increase by roughly 30 % as shown in Fig. 5.27. The phenomenon was caused by the increased viscosity of air by about 30 % due to the rise of gas temperature. This relationship conformed to equation (3.1) in which pressure drop was directly proportionally to the viscosity of air when the specific resistance of filter and dust cake, filtration velocity and dust concentration were kept to be constant.

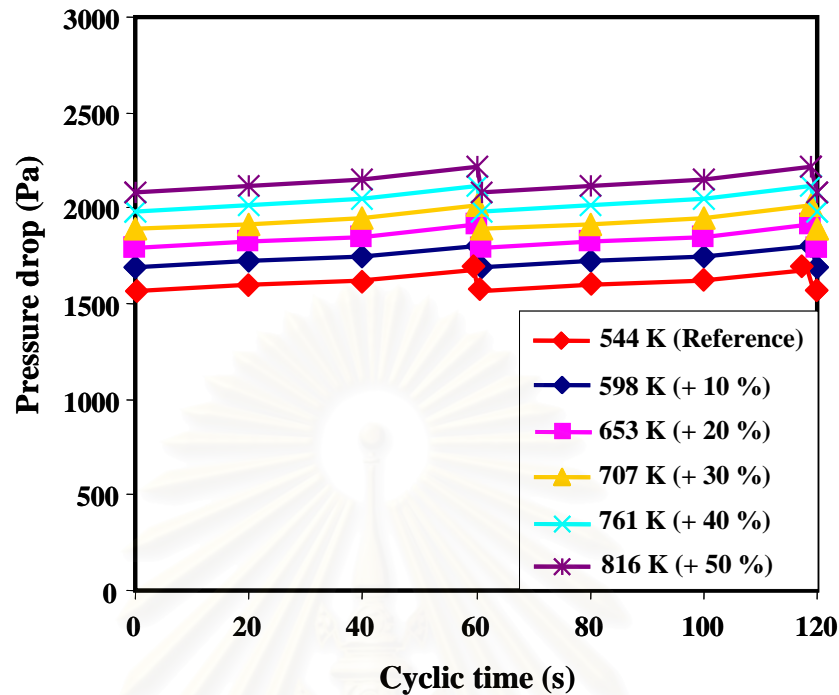


Fig. 5.27 The effect of temperature on pressure drop as a function of time

5.4 Effect of influent gas flow rate at high temperature

As mentioned in the previous section, we will use a new CFD model created from the experimental data at high temperature (0.38 m³/min, 544 K, 5 g/m³ of Fly ash JIS10) to estimate the behavior of the system at other high temperature conditions. The higher the gas flow rate, the higher the predicted pressure drop. For example, when the flow rate was increased by 50 %, the pressure drop was found to increase by roughly 50 % as shown in Fig. 5.28. The phenomenon was caused by the increased gas velocity flowing through the porous medium that increased the flow resistance and the possible compression of dust cake layer. This relationship was consistent with equation (3.2), in which the pressure drop was directly proportional to the volumetric gas flow rate when the specific resistance of filter and dust cake, viscosity of air, dust concentration and filtration area were kept constant.

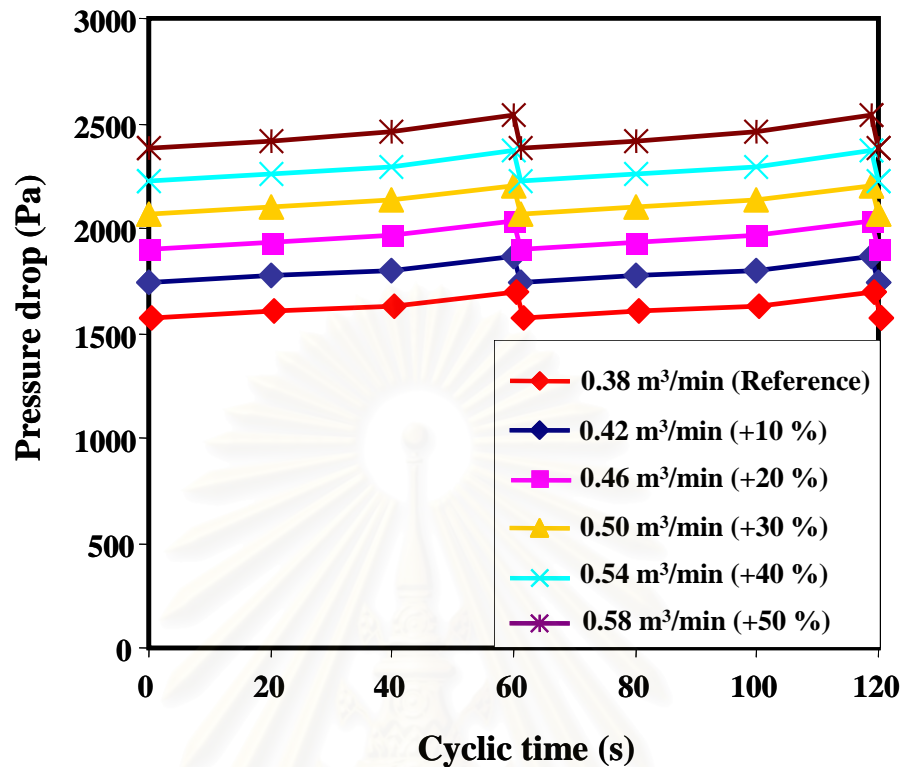


Fig. 5.28 The effect of flow rate on pressure drop at high temperature condition (544 K)

5.5 Effect of dust concentration at high temperature

In this section, we would use the new CFD model created from the experimental data at high temperature (0.38 m³/min, 544 K, 5 g/m³ of Fly ash JIS10) to estimate the behavior of the system at other high temperature conditions. The higher the dust concentration, the higher the predicted pressure drop. For example, when the dust concentration was increased by 50 %, the pressure drop was found to increase by roughly 5 % as shown in Fig. 5.22. As indicated by the results shown in Fig. 5.22, the specific resistance of the clean filter was 350% more than that of the dust cake. Consequently, a small alteration of dust concentration didn't show a significant short-term effect on the pressure drop of the filtration system.

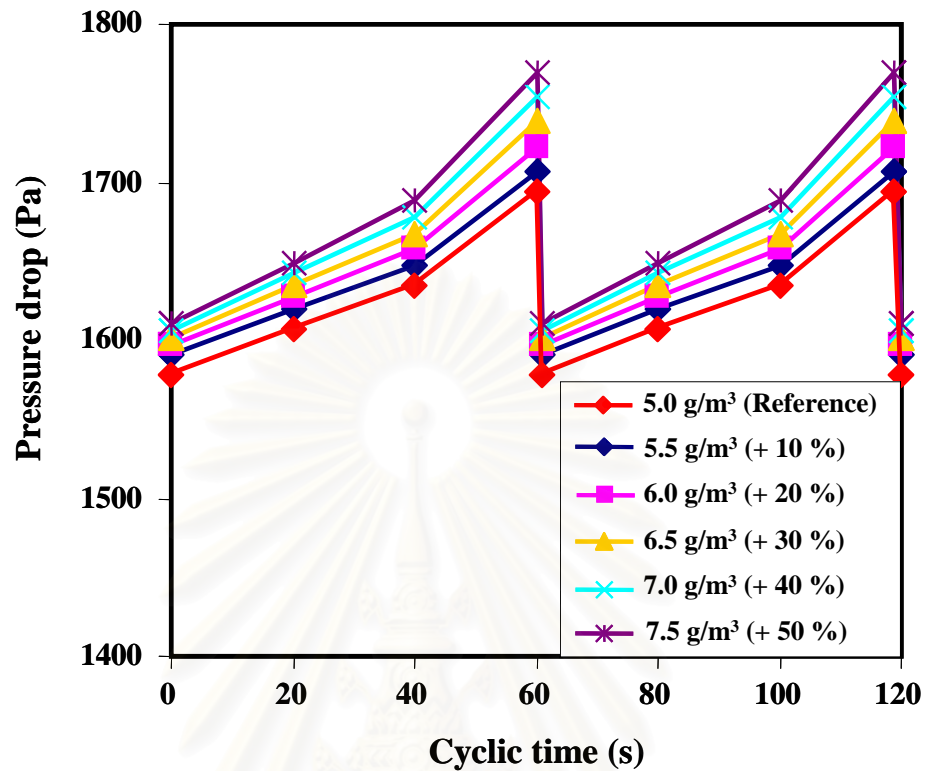


Fig. 5.29 The effect of dust concentration on pressure drop at high temperature condition (544 K)

5.6 Effect of gas inlet location at high temperature

In this section, we also used the new CFD model created from the experimental data at one high temperature (0.38 m³/min, 544 K, 5 g/m³ of Fly ash JIS10) to estimate the behavior of the system at other high temperature conditions. From Fig. 5.30, we found that the inlet gas location was not a significant parameter that affected the pressure drop of the system. The pressure drop in each case is less than 2% in difference. However, the tangential feed location gave the lowest value of pressure drop. As shown in Fig. 5.31, the velocity profile in the tangential feed case expressed the circulatory flow in the system. Therefore, the loss of gas energy due to sudden change in flow velocity and direction made the pressure drop of the system decrease slightly.

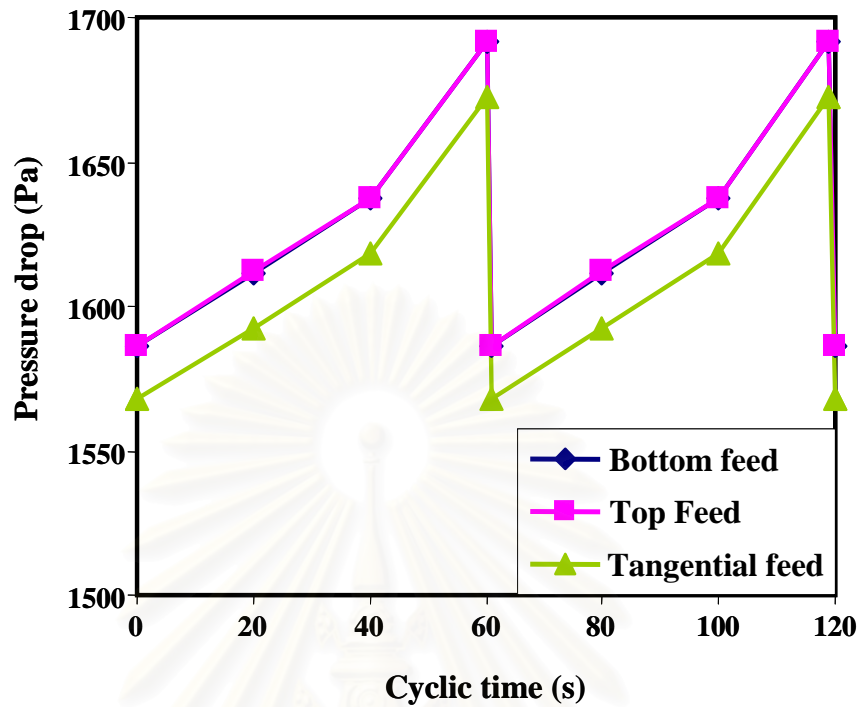


Fig. 5.30 The effect of gas inlet location on the pressure drop as a function of time

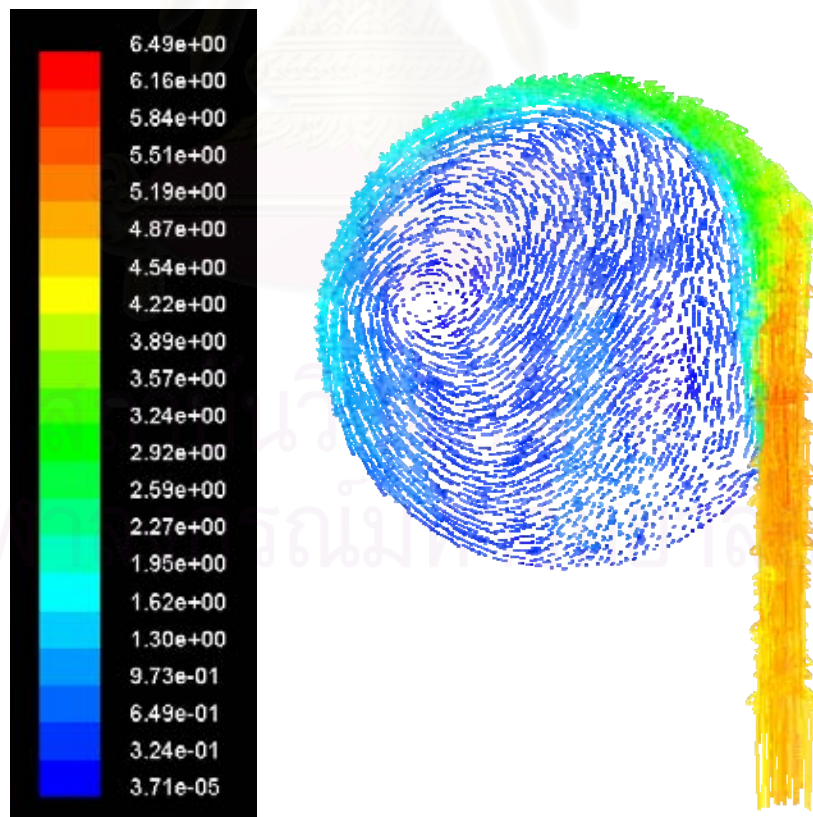


Fig. 5.31 Profile of velocity vector at inlet port as a function of x and y for the tangential feed port of the twin candle system (m/s)

CHAPTER VI

CONCLUSION AND RECOMMENDATION

6.1 Conclusion

The CFD simulation has been divided into 2 parts. First, we considered the clean virgin filter with clean air, and second, cyclic operation of the filter (dust-laden air, pulsed cleaning).

6.1.1 Virgin filter with clean air

The CFD model was validated against the available experimental data on an identical twin-candle system for both clean air using virgin candles and dust-laden air in cyclic operations. Next the effect of the gas flow rate and the gas temperature were investigated in the case of virgin candle filter. As the gas flow rate or the temperature increased, the characteristic pressure drop will increase proportionally in a linear manner. The positive effect of the gas flow rate on the pressure drop was found to be more significant than that of the gas temperature. Though the spatial flow distribution of clean air through the clean twin filters A and B was essentially symmetrical, the height (Z) on the candle significantly affected the local normal face velocity whereas the location of a quadrant at the same height had negligible effect. In fact, the spatial distribution of face velocity of either virgin filter may be classified into 4 zones as listed in **Table 5.1**.

6.1.2 Cyclic operation (dust-laden air, pulsed cleaning)

In the case of cyclic operation (dust-laden air, pulsed cleaning), when the filter was pulse-cleaned, all of the temporary cake was removed but the permanent cake still remained. The candle surface area that attracted the most flow and consequently the highest rate of dust deposit was the top end of the candle filters. The relative change in the temporary cake thickness was calculated in terms of the percentage compared to the permanent cake thickness. It can be considered that the local cake thickness increased as a linear function of the local face velocity. Upon the initiation of pulsed cleaning, the temporary cake on the adjacent candle was estimated

to be removed by approximately 20 % compared with its permanent cake thickness. In reality the unexpected decrease in resistance may not actually be due to any decrease in the temporary cake thickness but should be caused by the sudden decrease in local face velocity on the adjacent candle. It is found that the observed fluctuation in the pressure drop was caused not only by the change in the cake thickness but also by the compressibility of the cake, thereby changing the rate of rise in the pressure drop at each time interval.

When we considered the local flow resistance and corresponding pressure drop at each short time interval, it was found that the local resistance of each element (a total of 32 elements in each candle filter) was caused a corresponding difference in the local face velocity distribution. Similar to the case of the virgin candle filter, the local face velocity can be divided into 4 zones along the height of the candle filters as in the case of the virgin filter; the higher the position of height, the higher the local face velocity. By the way, the face velocity in each quadrant of the same layer did not show any significant difference. This means that the popular simple assumption of uniform cake deposition on the whole surface of each candle is not valid. Obviously, the effect of gas flow rate to the pressure drop of the system was higher than of that of the gas temperature, influent dust concentration and gas inlet location, respectively. In fact, the gas inlet location has nearly insignificant effect on the pressure drop of the filtration system (less than 2 percent).

6.2 Recommendation

- Further investigation should be carried out on the effect of the gas temperature on the properties of the ceramic candle filter and dust cake properties.
- The cohesive and adhesive forces of dust particles may be added to the simulation model by writing some additional code.
- The experimental data on the pressure drop should be collected more frequently than every 20 seconds to ensure higher accuracy of predicting the phenomena.

REFERENCES

- [1] A. Larbot, M. Bertrand, S. Marre, E. Prouzet. Performances of ceramic filters for air purification. Separation and Purification Technology 32 (2003): 81-85.
- [2] E.Schmidt. Experimental investigations into the compression of dust cakes deposited on filter media. Filtration & Separation 32 (1995): 789-793.
- [3] C.R.N. Silva, V.S. Negrini, M.L. Aguiar and J.R. Coury. Influence of gas velocity on cake formation and detachment. Powder Technology 101 (1999): 165-172.
- [4] K. Smolders and J. Baeyens. Cleaning of hot calciner exhaust gas by low-density ceramic filters. Powder Technology 111 (2000): 240-244.
- [5] C. Kanaoka and M. Amornkitbamrung. Effect of filter permeability on the release of captured dust from a rigid ceramic filter surface. Powder Technology 118 (2001): 113-120.
- [6] D. Thomas, P. Penicot, P. Contal, D. Leclerc and J. Vendel. Clogging of fibrous filters by solid aerosol particles Experimental and modeling study. Chemical Engineering Science 56 (2001): 3549-3561.
- [7] J.C. Ruiz, P.H. Blanc, E. Prouzet, P. Coryn, P. Laffont and A. Larbot. Solid aerosol removal using ceramic filters. Separation Purification Technology 19 (2000): 221-227.
- [8] J.H. Choi, S.J. Ha and H.J. Jang. Compression properties of dust cake of fine fly ashes from a fluidized bed coal combustor on a ceramic filter. Powder Technology 140 (2004): 106-115.
- [9] C. Stockmayer and W. Hoflinger. Simulation of the regeneration of dust filters. Mathematics and Computers in Simulation 46 (1998): 601-609.
- [10] A. Aroussi, K. Simmons and S.J. Pickering. Particulate deposition candle filters. Fuel 80 (2001): 335-343.
- [11] A. Karadimos and R. Ocone. The effect of the flow field recalculation on fibrous filter loading: a numerical simulation. Powder Technology 137 (2003): 109-119.

- [12] A. Dittler, M.V. Ferer, P.Mathur, P. Djuranovic, G. Kasper and D.H. Smith. Patchy cleaning of rigid gas filters - transient regeneration phenomena comparison of modelling to experiment. Powder Technology 124 (2002): 55-66.
- [13] T.G. Chuaha, C.J. Withers and J.P.K. Seville. Prediction and measurements of the pressure and velocity distributions in cylindrical and tapered rigid ceramic filters. Separation and Purification Technology 40 (2004): 47–60.
- [14] Y. Awni and A. Otoom. Prediction of the collection efficiency, the porosity, and the pressure drop across filter cakes in particulate air filtration. Atmospheric Environment 39 (2005): 51–57.
- [15] Z. Ji, M. Shi, F. Ding. Transient flow analysis of pulse-jet generating system in ceramic filter. Powder Technology 139 (2004): 200–207.
- [16] S. Calle, P. Contal, D. Thomas, D. Bemer and D.Leclerc. Description of the clogging and cleaning cycles of the filter media. Powder Technology 123 (2002): 40-52.
- [17] C.B. Neiva and L.Goldstein. A procedure for calculating pressure drop during the build-up of dust filter cakes. Chemical Engineering and Processing 42 (2003): 495-501.
- [18] W.C. Hinds. Aerosol Technology. 2nd ed. New York: Wiley-Interscience Publication, 1998.
- [19] H.K. Versteeg and W. Malalasekera. An introduction to computational fluid dynamics. New York: Longman Scientific & Technical, 1995.
- [20] S.V. Patankar. Numerical heat transfer and fluid flow. New York: McGraw-Hill Book, 1980.
- [21] C.T. Shaw. Using computational fluid dynamics. , Hertfordshire: Prentice Hall International, 1992.
- [22] J.H. Ferziger and M. Peric. Computational methods for fluid dynamics. 2nd ed. New York: Springer, 1999.
- [23] ศิริกัลยา สุวจิตตานนท์, วิวัฒน์ ดัฒชะพานิชกุล, ชีลาโอะ คานาโอกะ, จุฑามาศ เกตุทัต. มลภาวะอากาศ. กรุงเทพมหานคร: สำนักพิมพ์มหาวิทยาลัยเกษตรศาสตร์, 2542.

- [24] นภาพร พานิช, แสงสันดี พานิช, วงศ์พันธ์ ลิ้มปเสนีย์, วิจิตรา จงวิศาล และ วราวุธ เสือดี. ตำราระบบบำบัดมลพิษอากาศ. กรุงเทพมหานคร: ศูนย์บริการวิชาการแห่ง จุฬาลงกรณ์มหาวิทยาลัย, 2547.

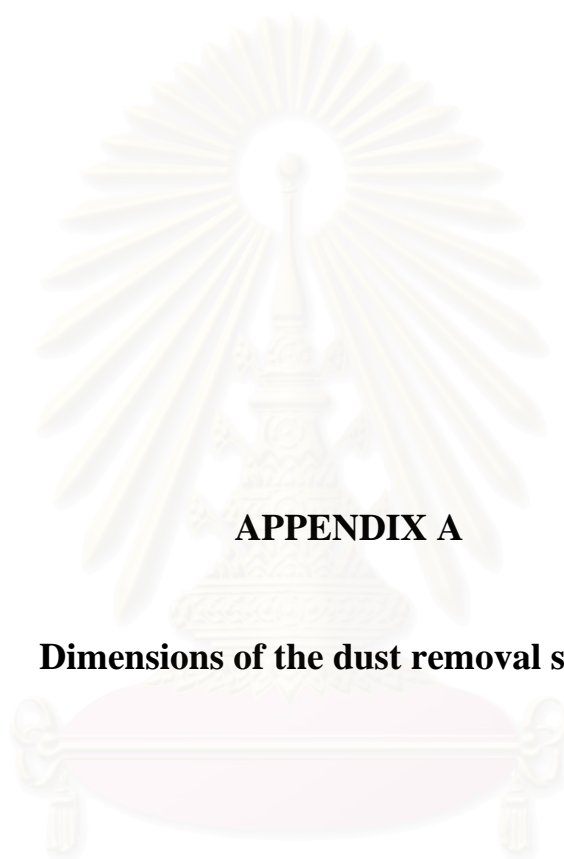


สถาบันวิทยบริการ
จุฬาลงกรณ์มหาวิทยาลัย



APPENDICES

สถาบันวิทยบริการ
จุฬาลงกรณ์มหาวิทยาลัย



APPENDIX A

Dimensions of the dust removal system

สถาบันวิทยบริการ
จุฬาลงกรณ์มหาวิทยาลัย

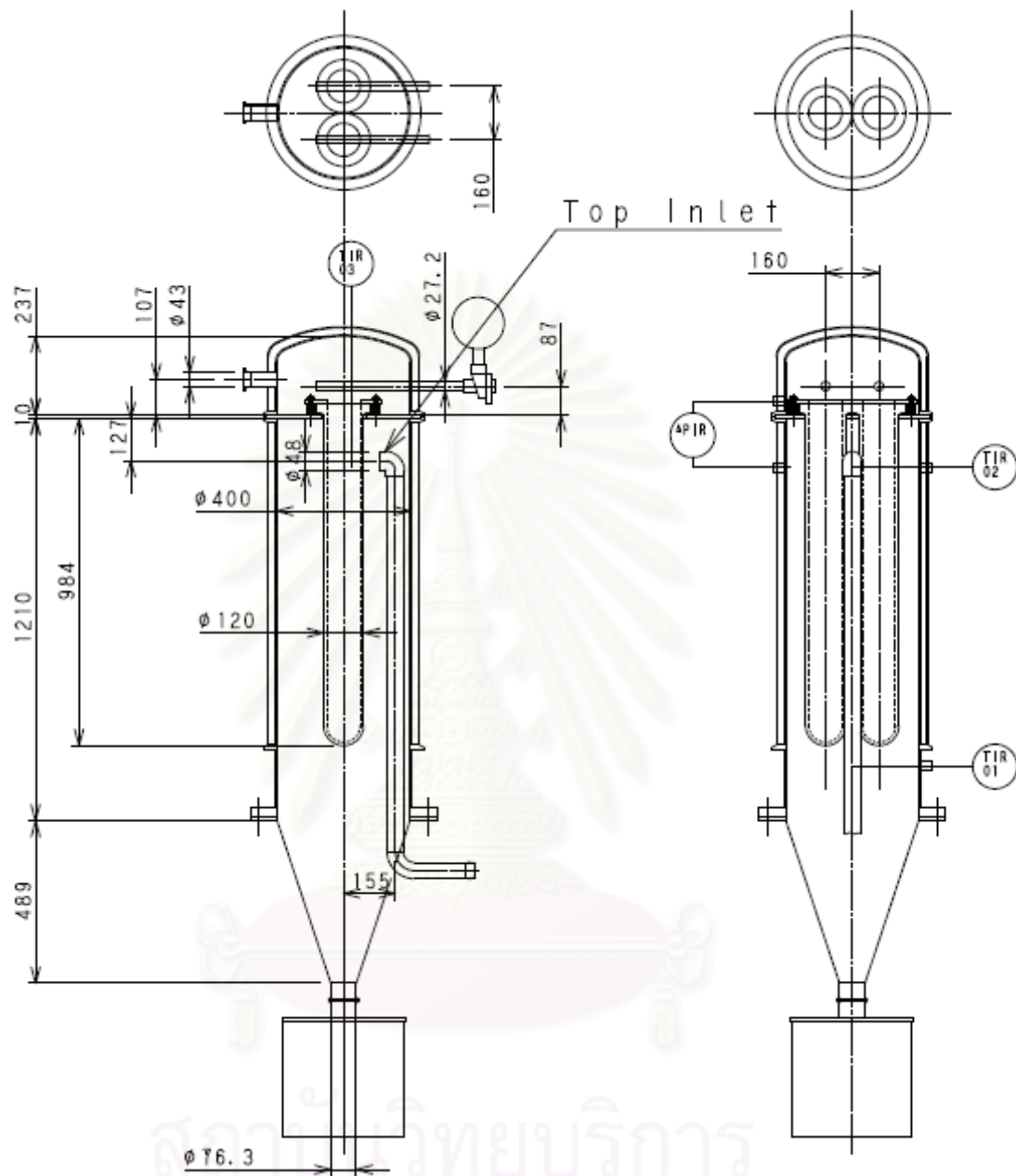


Figure A.1 The dimensions of the dust removal system fed from the bottom position

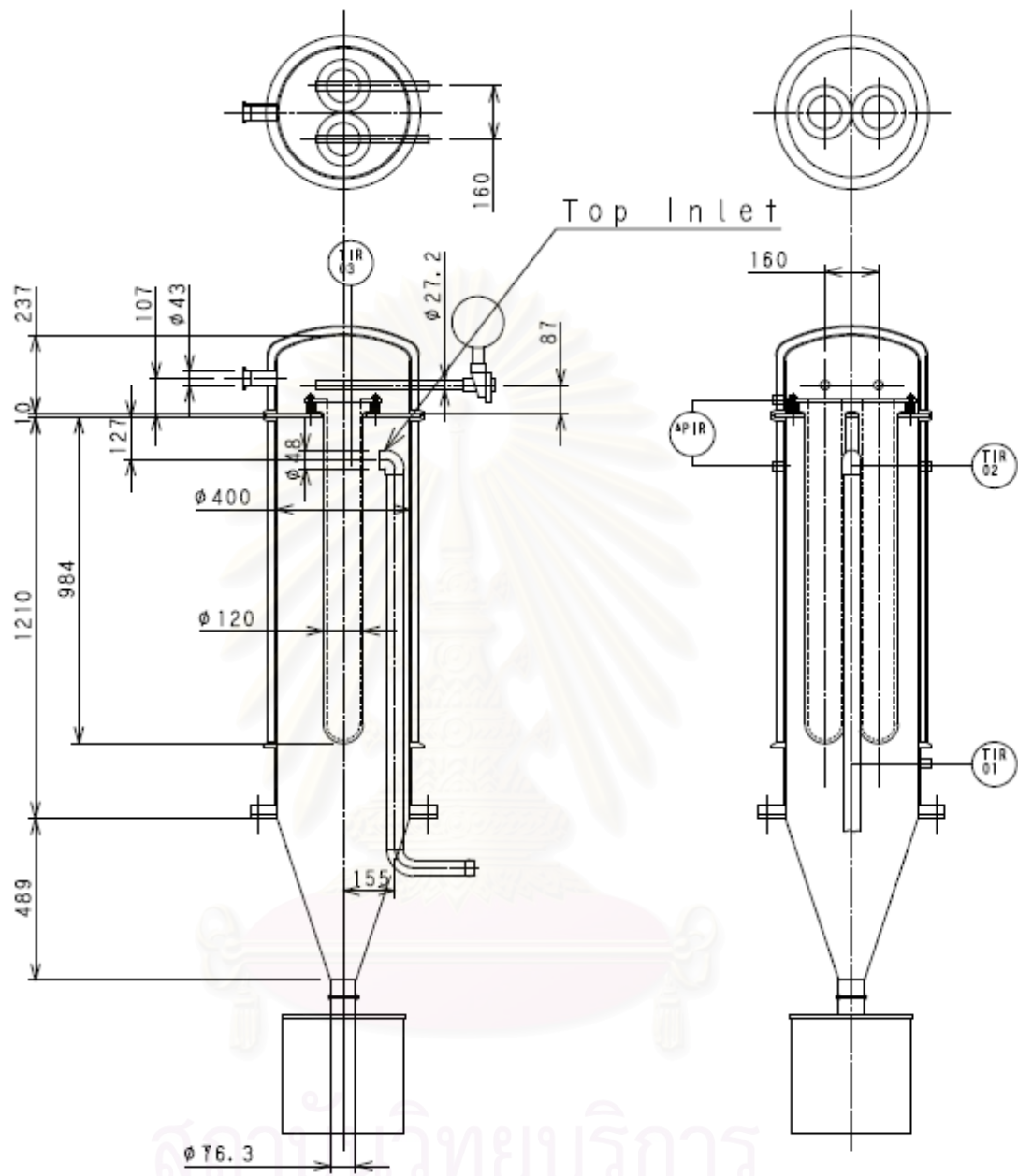


Figure A.2 The dimensions of the dust removal system fed from the top position

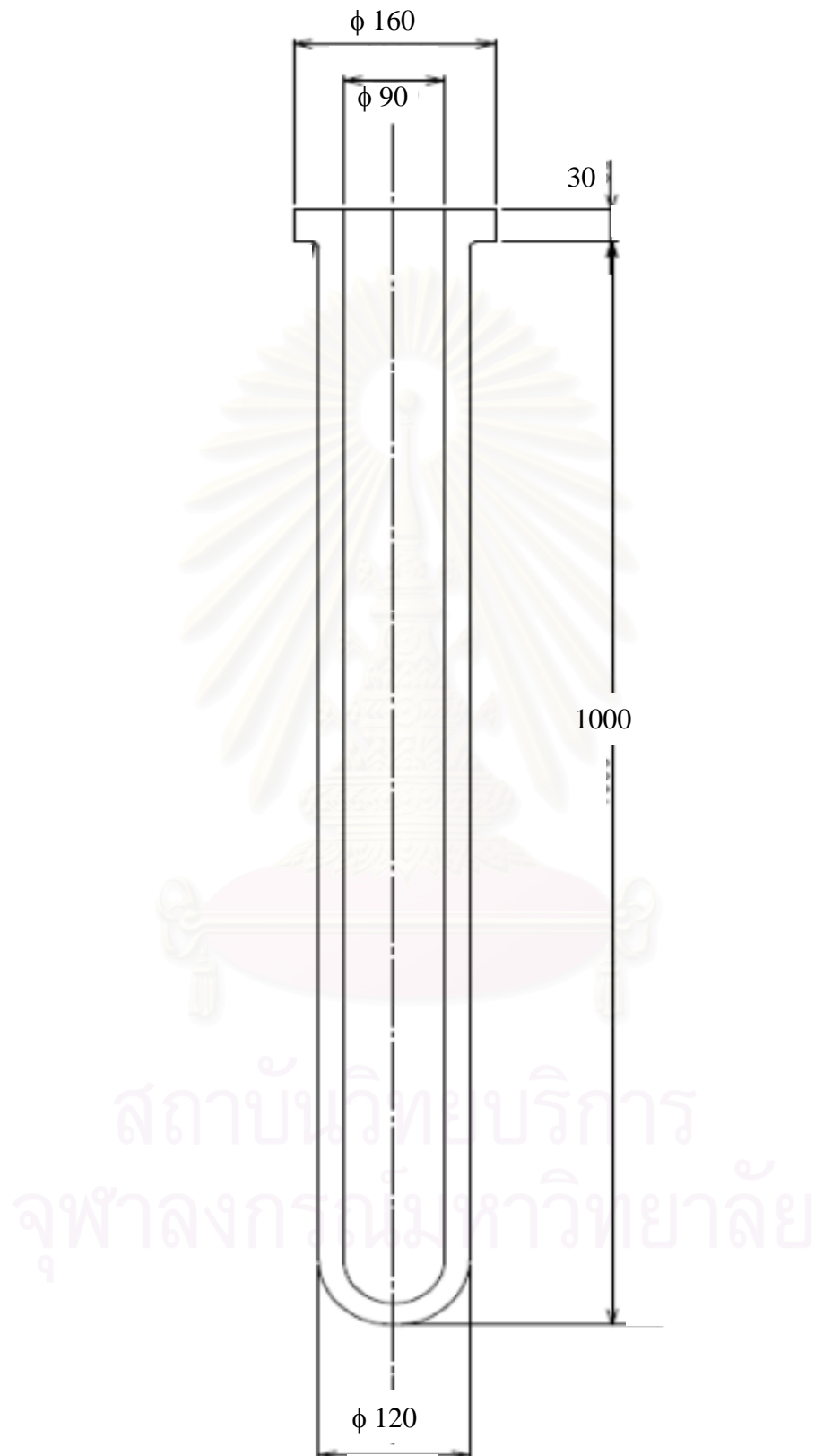


Figure A.3 The dimensions of the ceramic candle filter



APPENDIX B

Velocity vector profile

สถาบันวิทยบริการ
จุฬาลงกรณ์มหาวิทยาลัย

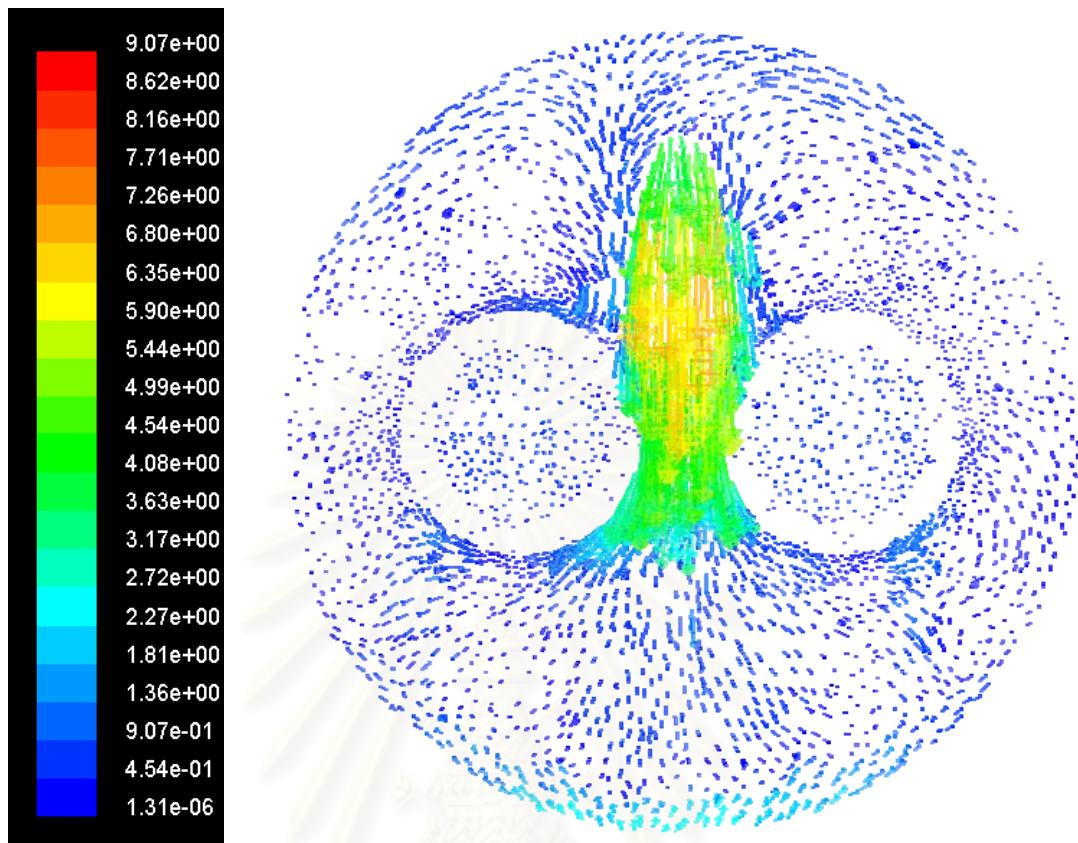


Figure B.1 Profile of velocity vector at $z = -100$ as a function of x and y for the top feeding port of the twin candle system (m/s)

สถาบันวิทยบริการ
จุฬาลงกรณ์มหาวิทยาลัย

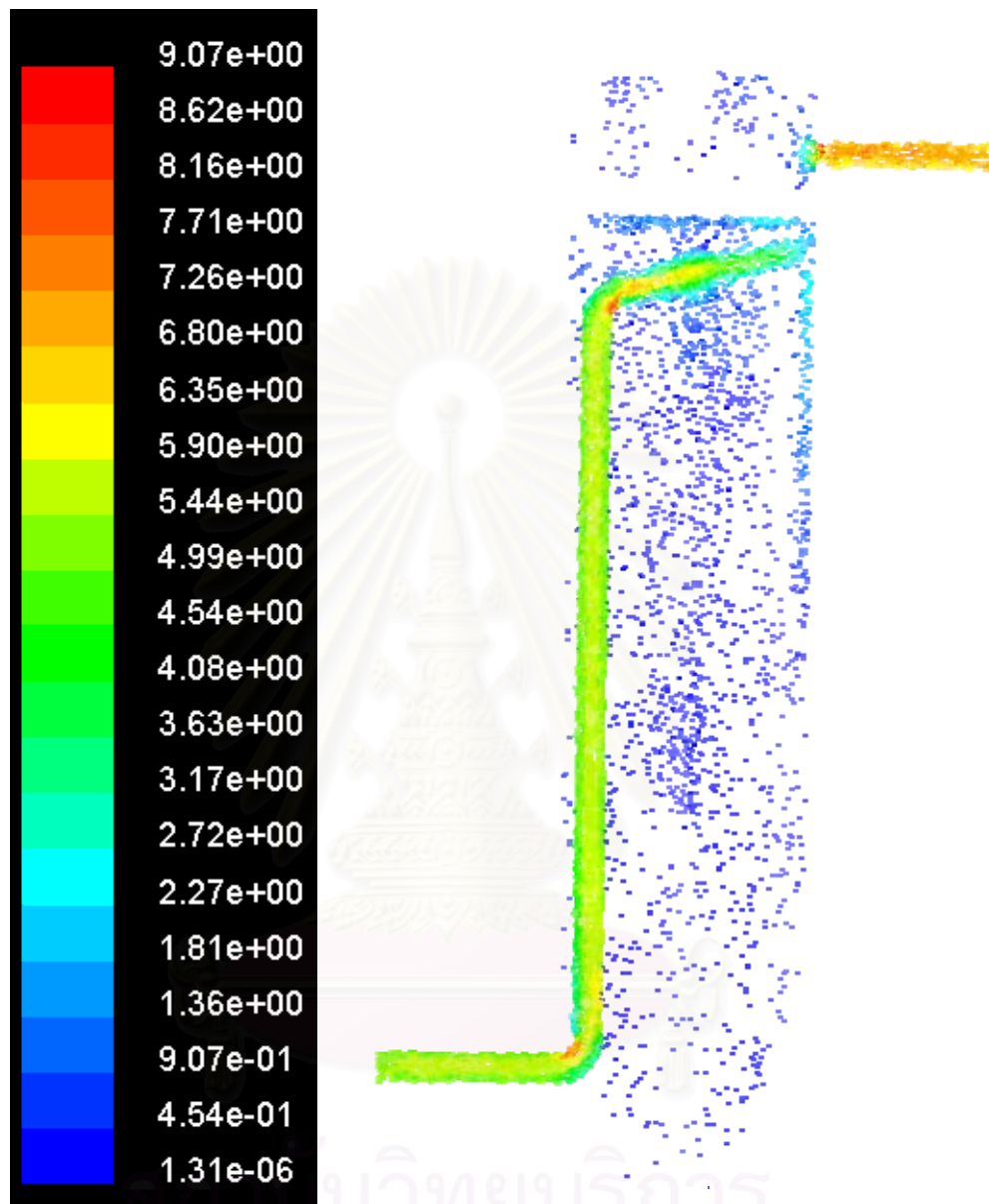


Figure B.2 Profile of velocity vector at $x = 0$ as a function of y and z for the top feeding port of the twin candle system (m/s)

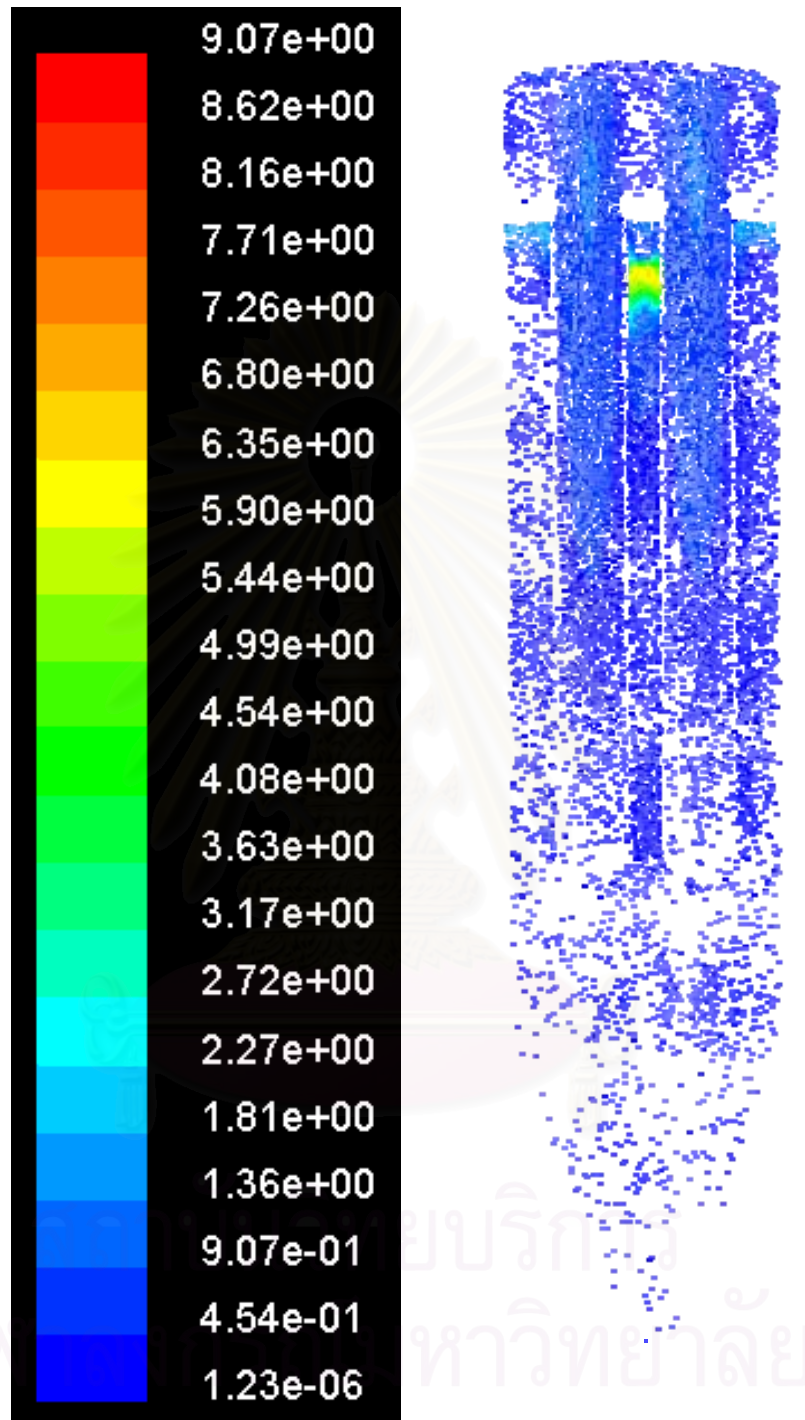


Figure B.3 Profile of velocity vector at $x = 0$ as a function of x and z for the top feeding port of the twin candle system (m/s)

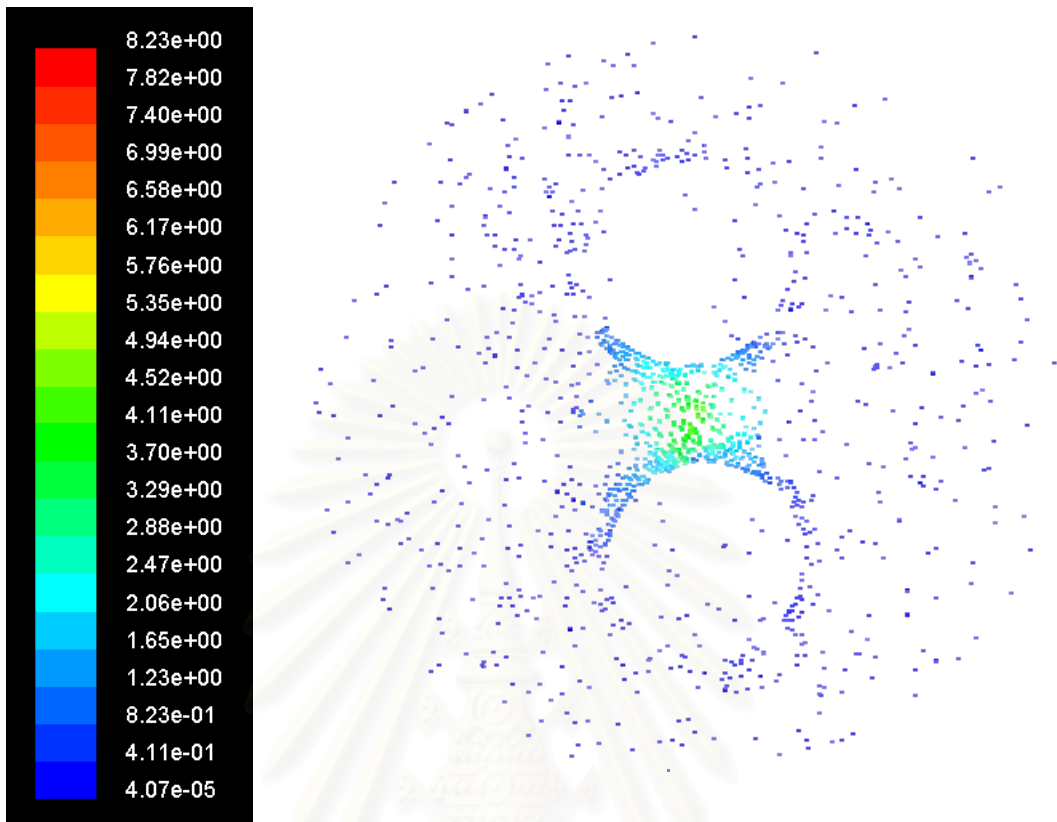


Figure B.4 Profile of velocity vector at inlet port as a function of x and y for the bottom feeding port of the twin candle system (m/s)

สถาบันวิทยบริการ
จุฬาลงกรณ์มหาวิทยาลัย

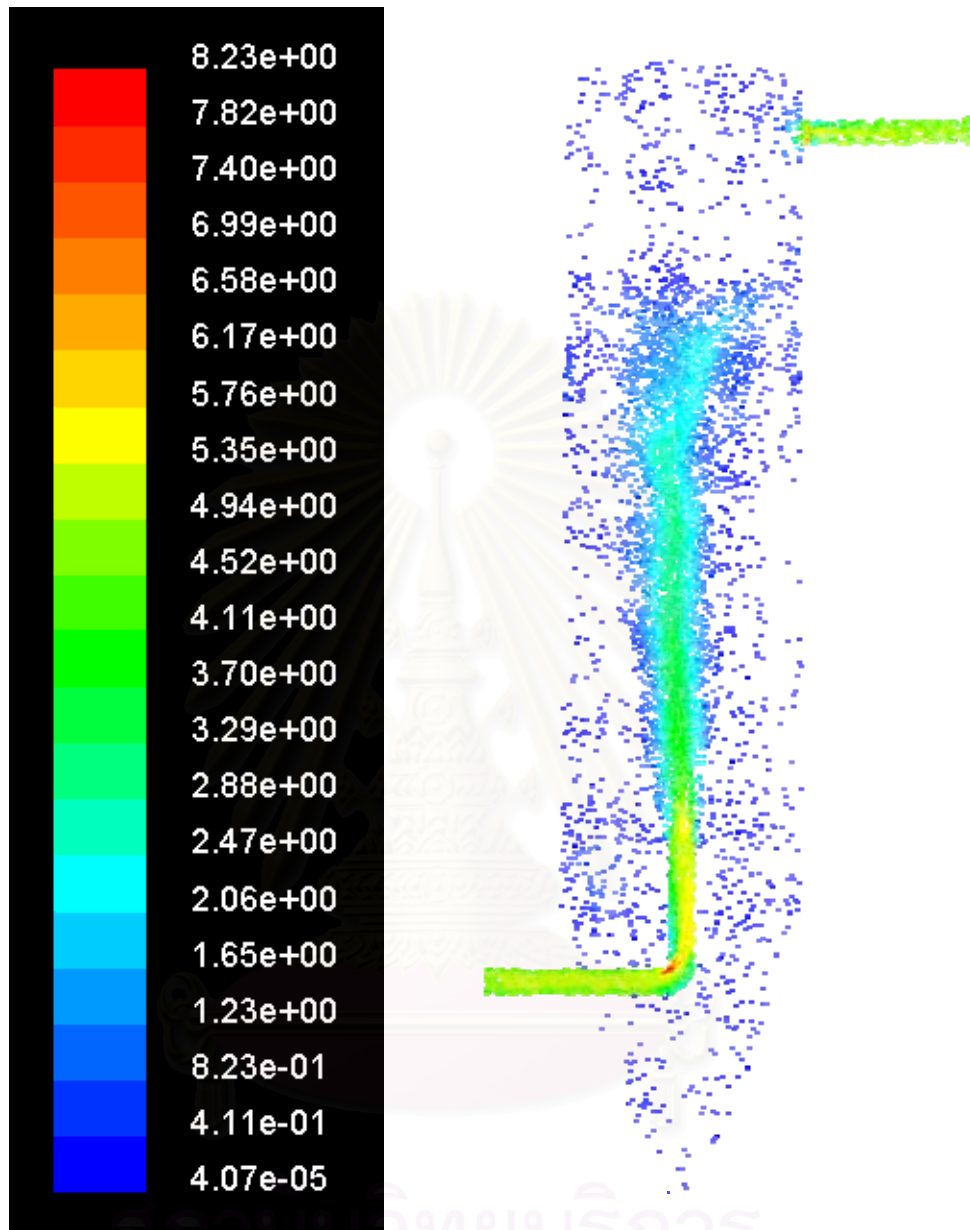


Figure B.5 Profile of velocity vector at inlet port as a function of y and z for the bottom feeding port of the twin candle system (m/s)

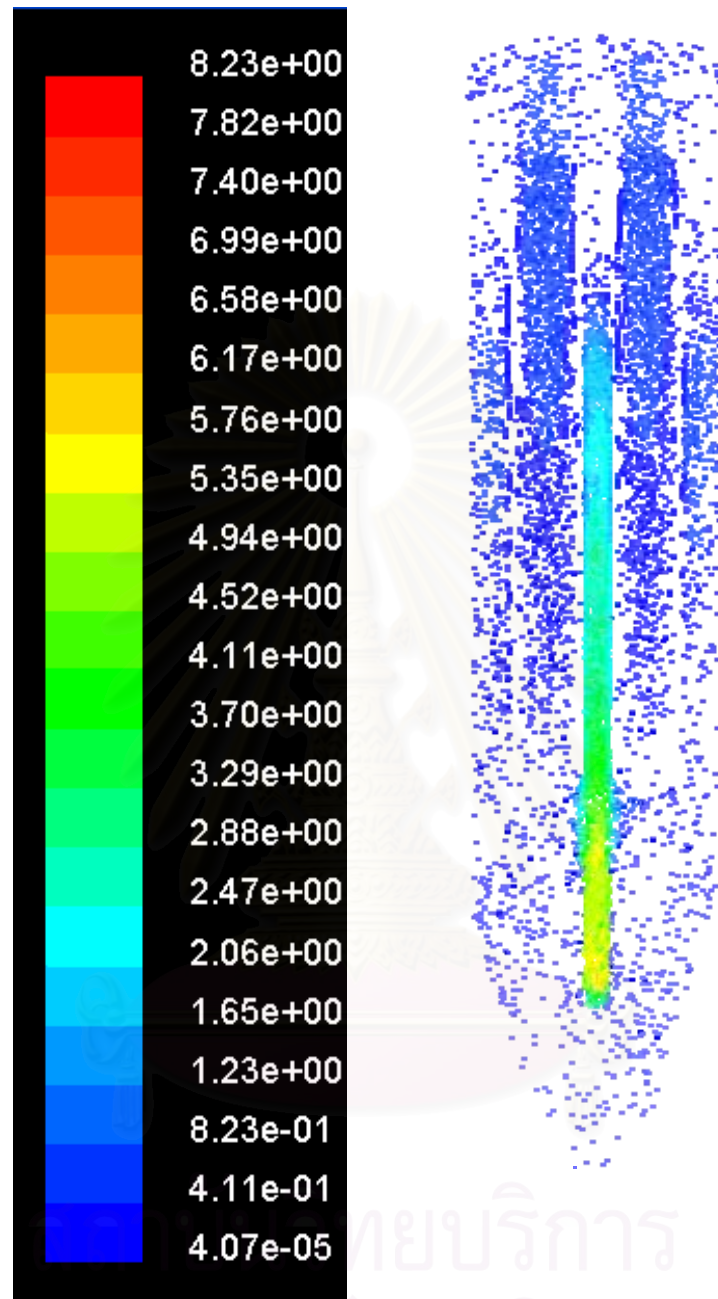


Figure B.6 Profile of velocity vector at inlet port as a function of x and z for the bottom feeding port of the twin candle system (m/s)



APPENDIX C

Pressure drop from simulation

สถาบันวิทยบริการ
จุฬาลงกรณ์มหาวิทยาลัย

Table C.1 Pressure drop at various temperatures

The filtration velocity and dust concentration were kept constant at 0.85 cm/s and 5 g/m³, respectively.

Cyclic time (s)	Pressure drop (Pa)						
	15 °C	100 °C	200 °C	300 °C	400 °C	500 °C	600 °C
0	999	1206	1443	1697	1824	1999	2157
20	1015	1225	1467	1725	1854	2031	2192
40	1026	1250	1488	1749	1887	2070	2233
60	1066	1286	1539	1810	1945	2131	2301
61	999	1206	1443	1697	1824	1999	2157
80	1015	1225	1467	1725	1854	2031	2192
100	1026	1250	1488	1749	1887	2070	2233
120	1026	1250	1488	1749	1887	2070	2233

Table C.2 Pressure drop at various filtration velocities

The influent gas temperature and dust concentration were kept constant at 270 °C and 5 g/m³, respectively.

Cyclic time (s)	Pressure drop (Pa)				
	1 cm/s	2 cm/s	3 cm/s	4 cm/s	5 cm/s
0	1872	3743	5600	7472	9342
20	1902	3804	5690	7593	9492
40	1927	3858	5780	7713	9643
60	1996	3992	5972	7969	9962
61	1872	3743	5600	7472	9342
80	1902	3804	5690	7593	9492
100	1927	3858	5780	7713	9643
120	1996	3992	5972	7969	9962

Table C.3 Pressure drop at various dust concentrations

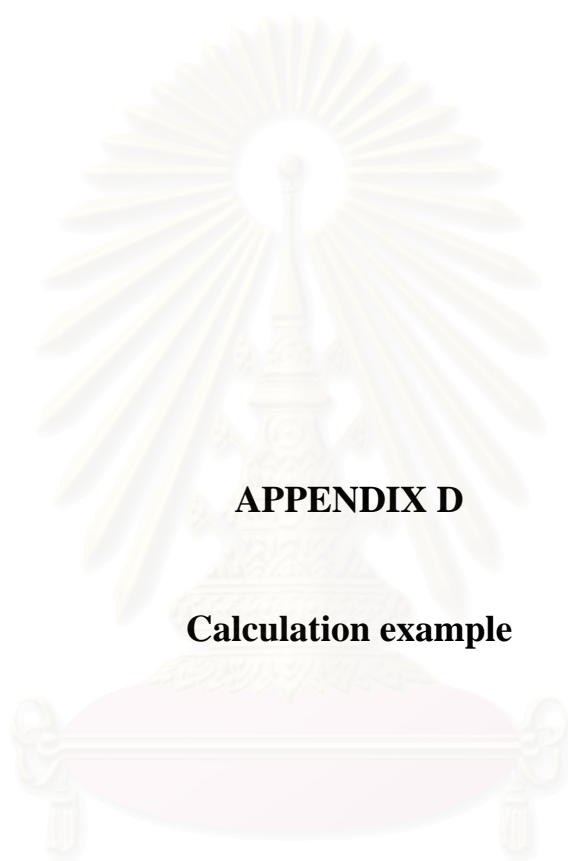
The filtration velocity and influent gas temperature were kept constant at 0.85 cm/s and 270 °C, respectively.

Cyclic time (s)	Pressure drop (Pa)					
	5 g/m ³	10 g/m ³	20 g/m ³	30 g/m ³	40 g/m ³	50 g/m ³
0	1586	1732	1878	2024	2170	2316
20	1612	1760	1908	2057	2205	2353
40	1637	1788	1939	2089	2240	2391
60	1692	1847	2003	2159	2314	2470
61	1586	1732	1878	2024	2170	2316
80	1612	1760	1908	2057	2205	2353
100	1637	1788	1939	2089	2240	2391
120	1692	1847	2003	2159	2314	2470

Table C.4 Pressure drop at various feed locations

The filtration velocity, influent gas temperature and dust concentration were kept constant at 0.85 cm/s, 270 °C and 5 g/m³ respectively.

Cyclic time (s)	Pressure drop (Pa)		
	Bottom	Top	Tangential
0	1586	1587	1568
20	1612	1612	1593
40	1637	1638	1619
60	1692	1692	1672
61	1586	1587	1568
80	1612	1612	1593
100	1637	1638	1619
120	1692	1692	1672



APPENDIX D

Calculation example

สถาบันวิทยบริการ
จุฬาลงกรณ์มหาวิทยาลัย

The conditions of the experimental data used in calculation are as follows

- Gas flow rate : 0.38 m³/min
- Gas temperature : 270 °C
- Dust concentration : 5 g/m³
- Dust type : Fly ash JIS10

Assumption: the dust particles are uniformly distributed in the influent gas stream.

a) Calculate the total dust load

The dust load of fly ash in 5 seconds is equal to gas flow rate multiply by dust concentration and time interval

$$\text{Total dust load} = 0.38 \times 5 \times (5/60) = 0.1583 \text{ g}$$

b) Analyze the flow field

From the simulation results, we know the volumetric rate of gas flow through each section of candle filter. So we can calculate the fraction of gas flow rate in each section.

$$\text{Flow fraction} = \frac{\text{Flow of interested section}}{\text{Total flow rate}}$$

Assume that the flow rate of the interested section is equal to 0.0096 m³/min.

$$\text{Flow fraction} = 0.0096/0.38 = 0.0253$$

c) Calculate the dust load in each section

$$\begin{aligned} \text{Dust load of interested section} &= 0.0253 \times 0.1583 \\ &= 0.004 \text{ g} \end{aligned}$$

d) Calculate the cake thickness

Since the bulk density of fly ash is about 0.7 g/cm³, we assume that the dust cake layer has a uniform density of 0.7 kg/m³ and the filtration area of the interested section is equal to 175 cm².

$$\begin{aligned}
 \text{Local cake thickness} &= \frac{\text{Dust load of interested section}}{\text{Cake density} \times \text{local filtration area}} \\
 &= \frac{0.004}{0.7 \times 175} \\
 &= 3.3 \times 10^{-5} \quad \text{cm}
 \end{aligned}$$

e) Calculate the specific cake resistance

Assume that the viscosity of air is equal to 3×10^{-5} Pa.s and the cake resistance is equal to 40000.

$$\begin{aligned}
 \text{Specific cake resistance} &= \frac{\text{cake resistance} \times \text{filtration area}}{\text{viscosity of air} \times \text{dust load per area}} \\
 &= \frac{40000 \times (175/1000000)}{(3 \times 10^{-5}) \times (0.004/(175/1000000))} \\
 &= 10208 \quad \text{m}^{-1}
 \end{aligned}$$

สถาบันวิทยบริการ
จุฬาลงกรณ์มหาวิทยาลัย

VITA

Mr. Witsarut Jintaworn was born on October 13, 1981 in Ratchaburi, Thailand. He studied in primary and secondary educations at Benjamarachutit School, Ratchaburi and The Demonstration School of Rajabhat Institute Nakorn Pathom, respectively. In 2002, he received the Bachelor Degree of Engineering with a major in Chemical Engineering from Chulalongkorn University. After that, he continued to study in Master Degree program at Chemical Engineering Department, Engineering Faculty, Chulalongkorn University. He was award a Master's Degree in Chemical Engineering in April 2006.



สถาบันวิทยบริการ
จุฬาลงกรณ์มหาวิทยาลัย